Dissertation
submitted to the
Combined Faculties for the Natural Sciences and for
Mathematics
of the Ruperto-Carola University of Heidelberg, Germany
for the degree of
Doctor of Natural Sciences

presented by
Dipl.-Phys. Martin Dürr
born in Nakuru / Kenya

Oral examination: 5th of July 2006

Electron Induced Break-up of Helium: Benchmark Experiments on a Dynamical Four-Body Coulomb System

Referees: Prof. Dr. Joachim Ullrich
Prof. Dr. Andreas Wolf

Zusammenfassung:

Diese Arbeit stellt eine experimentelle Studie zu Fragmentationsprozessen von Helium durch Elektronenstoß vor. Dabei wurden absolute, vollständig differentielle Wirkungsquerschnitte zur einfachen Ionisation, zur gleichzeitigen Ionisation und Anregung sowie zur Doppelionisation gemessen. Durch Anwendung eines Abbildungsverfahrens für die geladenen Fragmente, einem sogenannten 'Reaktionsmikroskop', wird ein großer Teil des Impuls-Endzustandsraumes abgedeckt und die grundlegenden Einschränkungen der konventionellen Methoden überwunden. Das bisherige Reaktionsmikroskop konnte entscheidend verbessert werden, indem nun der Projektilstrahl parallel zu den Spektrometerfeldern geführt wird. In der Einfachionisation von Helium tritt bei beiden untersuchten Projektilenergien (102 eV und 1 keV) eine erhöhte Emission außerhalb der Streuebene auf, die auch bei Stößen mit Ionen beobachtet wurde (M. Schulz et al., Nature (London) **422**, 48 (2003)). Die winkelaufgelösten Querschnitte für die Doppelionisation von Helium bei 105 eV Einschussenergie zeigen, dass der Prozess durch die gegenseitige Abstoßung der Elektronen dominiert wird, wobei jedoch Signaturen einer komplexeren Dynamik erkennbar werden. Die gewonnenen Daten dienen als Test für neu entwickelte theoretische Beschreibungen des dynamischen Drei- und Vier-Körper Coulomb Problems.

Abstract:

This work presents an experimental study of fragmentation of helium by electron impact, in which absolute fully differential cross sections for single ionization, ionization-excitation and double ionization were determined. By applying a charged-particle imaging technique, the so-called 'reaction microscope', a large fraction of the final-state momentum space is covered, and the major limitations of previous experimental methods applied in this field could be overcome. Decisive modifications of the previous reaction microscope were undertaken, the most important one being the arrangement of the projectile beam parallel to the imaging-fields. For single ionization on helium an enhanced electron emission outside the projectile scattering plane is observed at both considered impact energies (102 eV and 1 keV), which is similar to the result found for ion-impact (M. Schulz et al., Nature (London) **422**, 48 (2003)). The angle resolved cross sections obtained for double ionization at 105 eV impact energy reveal, that the process is dominated by the mutual repulsion of the three final-state continuum electrons. However, signatures of more complex dynamics are also observed. The data provide an ultimate benchmark for recently developed theories treating the dynamical three- and four-body Coulomb problem.

Dos son compañía, tres son multitud.

Two's company, three's a crowd.

Contents

Chapter 1

Introduction

The study of atomic collisions is a long-standing field in atomic physics. Already in the late 19th century, pioneering experiments were performed by Philip Lenard studying electrons, at that time known as cathode rays, penetrating through matter. In the Rutherford Scattering with α-particles [Rut11], the structure of the atom was discovered. Another famous experiment is the study of inelastic electron collisions with atoms performed by Franck and Hertz [uGH14], where it was demonstrated that bound electrons have discrete excitation energies. Presently, the static and time-independent properties (the 'structure') of atoms and molecules like the binding energy of electrons can be calculated and measured with highest precision, a prominent example being the 1s-2s transition energy in the hydrogen atom [FKZ$^+$04]. Considering the 'dynamics' in atomic systems, the situation is quite different: The prediction and experimental investigation of even the most simple time-dependent few-body quantum systems as collision induced single or double ionization has remained challenging. Even the fundamental collision process involving three continuum particles, the single ionization of hydrogen near threshold, could only be solved 'exactly' in 1999 claiming to reduce the problem to a question of mere computation [RBIM99]. For a second method, the so-called 'Convergent Close Coupling', it was formally shown in 2002 that it is mathematically consistent and is able to yield accurate cross sections for all three-body Coulomb problems [Bra02]. Still these methods have not been demonstrated to be practicable for single ionization by fast electron or ion impact. All approximative calculations, including very sophisticated non-perturbative methods have failed so far reproducing fully differential cross sections for the latter situation, where the electron is emitted out of the scattering plane, defined by the incoming and outgoing projectile momentum vectors. Single electron emission by ion impact at low energies, where rich structures have been observed in recent experiments, have remained unexplained until today (e.g. [FPR91, DKP$^+$96, MO04]). Similarly, even measured total cross sections for the single ionization in col-

lisions with slow antiprotons are in conflict with all available theoretical calculations despite of considerable effort [LTL00]. The next more complicated, nevertheless basic dynamical reaction, double ionization of the most simple correlated two electron system, helium, can be considered solved only for the absorption of a single photon [BS00]. Two or many photon-induced He^{2+} production has just become close to be treated in three dimensions within ab-initio approaches [RPRB06], whereas collision induced double ionization heavily relies on approximative methods that are only applicable at high projectile energies [BLBC03].

For electron impact single ionization, kinematically complete studies have been feasible since the pioneering experiment by Ehrhardt in 1969 [ESTW69], establishing the field of so-called (e,2e) experiments. These measure the fully differential cross section, serve as valuable benchmarks for theoretical treatments, and provide an important contribution to the detailed understanding of dynamic processes. Nevertheless, even after more than 30 years of experimental efforts by many groups world-wide not a single 'complete' data set at any collision energy exists, in the sense that the emission of the electron was detected over a substantial part of the final-state momentum space, that is for the most of the electron ejection energies and angles. No fully differential data at all could be recorded in ion impact induced single ionization until 1994 [MUU$^+$94], and only three measurements, under very restricted kinematical conditions do exist using conventional techniques for electron impact double ionization of He, so called (e,3e) data, obtained under great efforts over months of beamtime [TLBDA98, KBLB$^+$99, LBDC$^+$03].

With respect to the 'conventional' technique, the invention of the reaction microscopes marked a decisive improvement [UMD$^+$03]. By employing projection techniques it basically overcomes all the previous limitations, covering almost the entire final-state momentum space for the detection of even several target fragments. First fully differential cross section became accessible for single ionization of helium induced by fast ions yielding three-dimensional images in surprising disagreement with all well established theoretical treatments [SMF$^+$03]. Even more troubling, the differences were observed in scattering geometries, which were never studied in (e,2e) experiments, such that their appearance questions the present understanding of the very basic and the assumedly solved process. Moreover, fully differential double ionization experiments become feasible at high impact energies for ion as well as electron collisions, delivering unprecedently complete data sets for testing the validity of theoretical perturbative approximations.

In the light of these rapid recent achievements on the one side, but troubling discrepancies for ion impact and gaps in the available (e,2e) and (e,3e) data on the other side for the most fundamental few-body quantum-dynamical atomic properties, this work is aimed to overcome the experimental shortcomings of present techniques and to substantially improve the present quality of benchmarks for theory.

First, complete three-dimensional images were taken for single ionization of helium by high and low energy electron impact. At the high energy, the strength of the interaction between the projectile and the target is identical to that in the ion impact experiments where the discrepancies with all existing theories have been observed. Second, electron impact double ionization was explored for the first time at low impact energies of E_0=105 eV. Third, at the same impact energy, fully differential cross sections for ionization with simultaneous excitation of the remaining bound electron have been obtained, where the reduced complexity of the final-state with only two continuum electrons provides first guidelines for newly developed four-body descriptions.

These experiments only became feasible after several refinements of the reaction microscope dedicated to electron impact, which previously was afflicted with a lower limit of the projectile energy of 500 eV [DKS$^+$03]. The projectile beam was aligned parallel with the imaging fields, such that low impact energies can be realized, and at the same time making the detection of the scattered projectile possible. Hereby the resolution could be substantially improved with respect to previous setups. Secondly, a new position-encoding device, the so-called Hexanode [Jea02], with superior multi-hit capabilities for electron detection was installed. This significantly improves the performance of imaging processes, in which several electrons are emitted. Furthermore, the possibility of detecting all final state electrons and the ability to reach low projectile energies also opens the way to study a great wealth of phenomena in the interaction of electrons with more complex targets like molecules.

The quantum dynamics of few-particle systems and its phenomena play a major role in many fields and applications, in particular where electrons interact with atomic species, molecules, clusters and solids. Quite recently in the year 2000, it was discovered that negative ion resonances can be made significantly responsible for double-strand breaks in DNA upon electron impact of low-energy electrons (3 eV-20 eV), which are below the ionization threshold [BCH$^+$00]. In low- and high-density plasmas electrons provide a way to efficiently transfer energy to atoms and molecules and thus play an important role. Chemical processes driven by interactions with electrons can be found for instance in planetary atmospheres or in technical applications like chemical vapor deposition (CVD) used in material science. Especially the interaction of low energy electrons with molecules is of particular importance.

Another aspect of applications is the increasing miniaturization of electronic devices on the nanoscale (e.g. heterostructures, quantum dots). In these devices, mainly based on semi-conductor technology, electrons play the key role with respect to the electronic and magnetic material properties also for developing fields like spin-based electronics (spintronics). At the present speed of miniaturization, the number of participating electrons will

be reduced from 'many' (several thousands) to a 'few' (less than hundred). Therefore the statistical description which is applied to macroscopic objects may become inaccurate, and different frameworks bridging the area between microscopic one-particle descriptions and macroscopic many-particle descriptions are needed. Here, theoretical frameworks describing few-body systems of interacting particles may become important.

The present work is organized in following manner: first, a brief introduction into electron impact ionization and the theoretical treatment is given. A selection of theoretical methods is presented, including those claiming to provide exact numerical solutions of the three-body Coulomb problem. The next chapter is dedicated to the experimental setup, presenting the newest enhancements of the reaction microscope and the resulting properties. Experimental results are discussed in chapter 4. The troubling situation encountered in ion impact is addressed by comparing the fully differential cross section obtained for single ionization at 1 keV impact energy under very similar dynamical conditions. Further, (e,2e) cross sections at lower impact energies of 102 eV for single ionization of helium are presented and compared with state-of-the-art descriptions of the dynamical three-body Coulomb problem. This forms the starting point for a whole series of fragmentation experiments, which were all performed at similar impact energy, studying phenomena which unfold an increasing degree of complexity. Chapter 4.2 discusses results on ionization with simultaneous excitation leaving the He^+ in the first excited state, which provide benchmarks for developing four-body descriptions of the Coulomb problem. The last experiment presented in this work is the double ionization of helium near the ionization threshold in chapter 4.3, where the full correlation between all four final-state particles becomes visible and provides an ultimate challenge to current theory. Finally, the presented results are summarized in chapter 5.

Chapter 2

Introduction to Ionizing Collisions

When a charged particle collides with an atom or molecule, a wide range of phenomena appears, depending on the charge, mass and velocity of the incoming projectile. Among these collision induced 'reactions' are processes like ionization, excitation or charge exchange, where one or several bound electrons change their quantum-state, and hence the scattering of the projectile can be seen as a dynamical few-body problem. One of the most fundamental and basic processes is the single ionization of Hydrogen by electron impact, where only three particles (two electrons and the proton) are involved. Out of the broad range of charged particle impact phenomena, this work studies the electron impact ionization of helium, which is the simplest correlated bound two-electron system. In total three different reactions were studied:

$$e^- + \mathrm{He} \rightarrow \mathrm{He}^+ + e^- + e^- \tag{2.1}$$

$$e^- + \mathrm{He} \rightarrow \mathrm{He}^{*+} + e^- + e^- \tag{2.2}$$

$$e^- + \mathrm{He} \rightarrow \mathrm{He}^{++} + e^- + e^- + e^-, \tag{2.3}$$

i.e. single ionization, single ionization with simultaneous excitation and double ionization of helium, respectively.

Electron impact single ionization of atoms or molecules, the ejection of one electron from an atom or molecule, is one of the most basic processes of atomic physics and has been extensively studied, since it is of major importance in a wide field of applications. For example in plasmas, this process is to a large extent responsible for the production of charged particles and is of decisive importance in fusion physics, the chemistry of the upper atmosphere or in applications like gas discharges used for instance as light sources. While single ionization of He can be generally regarded as an effective three-body process, the simultaneous excitation of the second bound electron eq. (2.2) represents a full four-body problem in which both bound electrons take

actively part, and where their correlation through the electron-electron interaction plays a far greater role. The same is true for double ionization, where in the final state in total four continuum particles interacting by the long-range Coulomb force make the theoretical description an even more challenging task. These four-body systems are presently subject of active research, experimentally and theoretically (e.g. [BLBC03, HMR05b]). The way to access such a dynamical process is the ionization probability which is more precisely quantified by the cross section. This quantity gives the measured reaction rate per target atom, normalized to the incident flux of particles. The link between the experimentally determined cross section and the theoretical quantum mechanical description, which yields the transition amplitude T_{fi}, is given by the relation

$$\sigma \propto |T_{fi}|^2. \tag{2.4}$$

The present chapter provides a brief introduction into the field of charged particle impact ionization of atoms, however, mainly focusing on the topics which are within the scope of this work. The theoretical description of atomic scattering is presented, also outlining the newest developments, which may be considered as a breakthrough after many decades of effort.

2.1 General Classification

A characteristic of each process in eq. (2.1),(2.2) and (2.3) is its total cross section as a function of the impact energy of the incoming electron. The measured cross section for single and double ionization by electron impact is shown in Fig. 2.1, and the first thing to be noticed is that single ionization is by two to three orders of magnitude more probable than double ionization [1]. The question arises what really determines the cross section at a given impact energy. In order to track down the determinants of a particular process, for example the importance of different mechanisms, higher differential data deliver deeper insight and also allow to sensitively check different approaches which supply a theoretical model to the problem. Instead of merely measuring the total ionization probability, the dependence on other kinematical variables can be studied. Examples are the energy distribution of the ejected electron, the dependence of the cross section with respect to the scattering angle, etc. The most detailed information is given by kinematically complete experiments which measure the fully differential cross section (FDCS), where the momenta of all collision partners are determined. In these studies of the ejection process induced by electron impact one generally speaks of the (e,2e) and (e,3e) process for single and double ionization, respectively [LB91]. The recorded emission characteristics provides deep insight to the

[1] The total cross section for ionization-excitation is omitted, since an accurate determination of proves to be very difficult (see [VB05] and references therein).

process, such that the underlying mechanisms can be revealed at a chosen impact energy. Some of these insights will be presented in the following chapter, within a classification of the dynamics of collision processes.

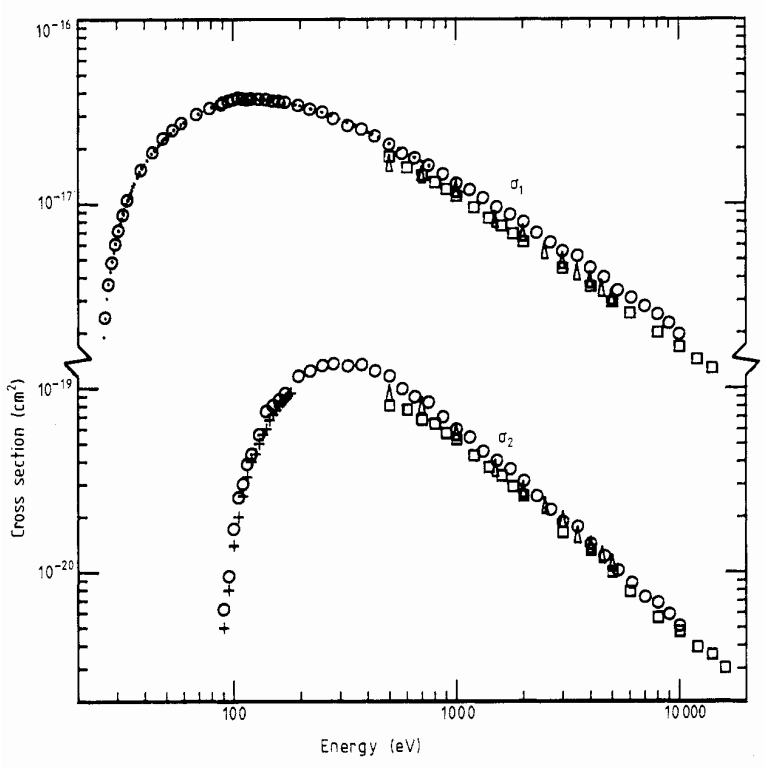

Figure 2.1: Experimental total cross section of single and double ionization of helium by electron impact labeled with σ_1 and σ_2, respectively. (From [SEMG88])

A classification in the spirit of a perturbative treatment shows to be particularly convenient. In the collision of a charged projectile with high velocity, the target atom sees a time-dependent electric field which acts as an external 'force' onto the target system. The interaction between the projectile and the atom is mediated through the exchange of a particular number of virtual photons, described by different 'orders' in perturbation theory. In the first order description, the momentum and energy is transfered to the target by one virtual photon, in the second order by two virtual photons, etc. This scheme can be applied for many reactions induced in a collision by any charged particle, in particular for the three studied in this work. A great advantage is, that this classification can be essentially used for the whole range of projectiles having different masses, charge states and velocities, and also a wide range of targets. The formal basis for this classification is found in the widely used Born Series, and was set beginning in the early days of

quantum mechanics in the treatment of inelastic charged particle collisions by Born [Bor26b, Bor26a] and later more extensively by Bethe [Bet30]. Formally the Born series is not tractable to computation beyond the second order, but provides a powerful description of quantum dynamical processes. The first order Born description significantly simplifies the description of the dynamics of collisions with charged particles and provides a good starting point (for a review see [Ino71]). The interaction is generally dominated by the exchange of one virtual photon, when the projectile is fast, which is equivalent to a short interaction time, and the induced electric field is not strong. 'Fast' means with respect to the velocity of the bound electron determining the time-scale of the atom, which is its classical orbiting time. The validity regime in which the first order treatment should provide an appropriate description will later be specified on a quantitative scale. When the projectile velocity is reduced, the number of exchanged photons is increased. Eventually, at very low velocities, an 'infinite' number of photons is exchanged, and the perturbative treatment breaks down since in principle all orders of interaction would have to be included.

2.1.1 'One-Photon'-Exchange

The simplest situation is the exchange of one virtual photon. Like for real photons, selection rules and particular symmetries appear, which are very distinct features of the first order process. The exchange of one photon is formally mirrored in the first Born approximation. As mentioned earlier, the classification scheme can be applied to many different dynamical processes and hence also to the three different channels studied in this work. In the following, some main features of the dynamics are discussed separately for single and double ionization. The discussion of the ionization-excitation process is omitted, since it does not exhibit further instructive features.

Single Ionization

For fast projectiles the ionization can be described by an exchange of one virtual photon. The analogy with the ionization by a real photon can be visualized by comparing the angular distributions of the ejected electron which show a dipolar character for both processes, photon and charged particle impact (Fig 2.2). The fully differential cross section is shown in a 3D polar plot and displays the angular emission for the ejected electron with fixed energy and in the case of charged particle impact at a fixed momentum transfer $\vec{q} = \vec{p_0} - \vec{p_1}$ which in analogy to the polarization vector manifests the quantization axis in charged particle impact. Here $\vec{p_0}$ ($\vec{p_1}$) is the momentum of the incoming (scattered) projectile. For both cases the ground state electron is in an s-state, and for photoionization within the dipole limit one quantum of angular momentum is transfered to the electron which was

initially carried by the absorbed photon. This is reflected in the dipolar emission pattern, which has the characteristic of a p-state.

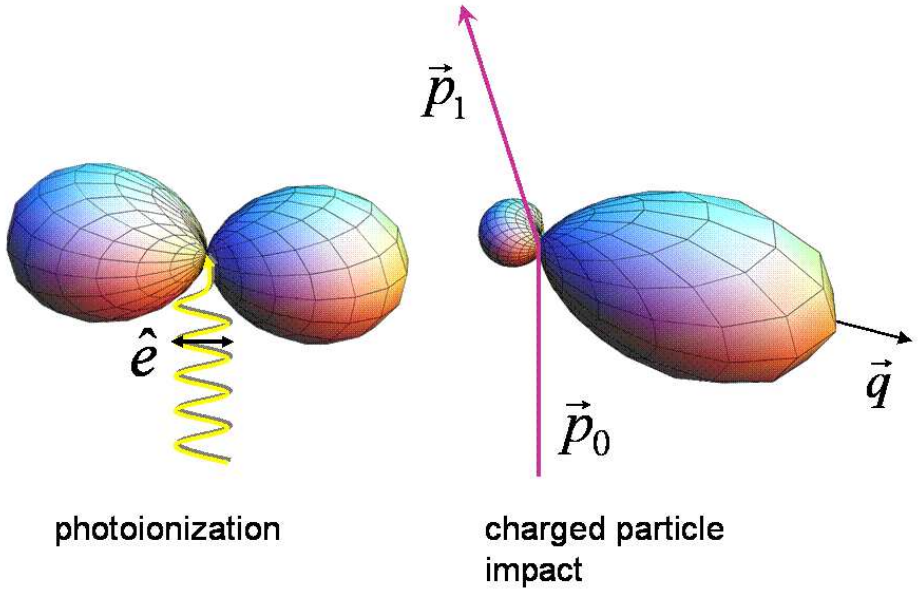

Figure 2.2: Comparison of the (calculated) angular emission pattern of the ejected electron for photoionization (left) and charged-particle impact ionization (right). The momentum transfer $\vec{q}$ manifests the quantization axis similar to the polarization axis $\hat{e}$ for photons.

A major difference between photon and collision induced processes is that in the latter case, the momentum transferred to the target is usually considerably larger. For photons, the dispersion relation uniquely couples its momentum to its energy. In charged particle impact, a wide range of momentum transfers is possible at a given energy transfer. Hence there is also a markedly difference between ionization processes induced by a real photon and the exchange of a virtual photon in charge particle collisions, as it is also visible in the angular emission pattern. Different from photons, several quanta of angular momentum can be exchanged between the projectile and the target and therefore electron collisions can induce transitions, that cannot be driven by photons, also manifesting the great importance of electron impact in applications. The difference vanishes, when the momentum transfer in particle collisions tends to zero.

The double lobe structure of the emission pattern in charged particle impact can be understood in an intuitive picture: the large lobe (the so-called binary lobe) in the direction of $\vec{q}$ corresponds to electrons emitted in a single binary collision with the projectile, i.e. the target nucleus remains essentially spectator. The smaller lobe pointing in the direction of $-\vec{q}$ re-

sults from collisions, where the projectile drives the target electron towards its own nucleus where it backscatters in the ionic potential. Therefore, the ion carries a large recoil momentum while the electron is emitted into the $-\vec{q}$ direction forming the so called recoil lobe. The particular shape and the magnitude of the binary and recoil lobes can strongly depend on the dynamics, which in the first order description is determined by the momentum transfer $\vec{q}$ and energy of the ejected electron.

Within this simplified description, the cross section for processes described by one photon exchange has a specific scaling behaviour

$$\sigma \propto (Z_P/v_P)^2, \tag{2.5}$$

Z_P being the charge of the projectile and v_P its velocity. The ratio is called perturbation $\eta = Z_P/v_P$. The cross section additionally depends on a matrix-element describing the 'strength' of the transition of the bound target-electron to the excited continuum state and which depends on the momentum and energy transfer and the specific target atom. As the total cross section in eq. (2.5) scales with η^2, it is independent of the charge-sign, which can be demonstrated by the experimental total cross section for single ionization that is identical for electrons, positrons, protons and anti-protons when they have equal velocity [AHK$^+$86, SEMG88]. This feature can be used to define the validity region of the first order description, which is reached at a projectile velocities of $v_P \approx 9$ a.u. for the total cross section of single ioniziation and singly charged projectiles with $Z_P = \pm 1$

However, higher differential cross sections turn out to be far more sensitive to higher order interactions which can be highlighted by considering the angle-resolved cross section. In so-called (e,2e) experiments first performed by Ehrhardt 1969 [ESTW69], the angular emission of the ejected electron with a fixed energy is determined at a fixed momentum transfer. Due to experimental constraints, the hereby resulting fully differential cross section has been obtained only in restricted geometries: like in almost all (e,2e) experiments, the angular emission is determined in the scattering plane, which is the plane containing the momentum transfer $\vec{q}$. It was shown that the first order limit for electron impact ionization of helium is reached only at an impact energy of 4 keV ($v_P = 17$ a.u.) in the experimental fully differential cross section [DCLB$^+$87] (see Fig.2.3).

Concluding, the general features of the cross section for one-photon exchange processes can be summarized in the following way:

- The cross section is essentially independent on the sign of the perturbation $\eta = Z_P/v_P$.
- The angular cross section is symmetric with respect to $\vec{q}$.
- For vanishing momentum transfer the cross section is equal to that obtained in photoionization.

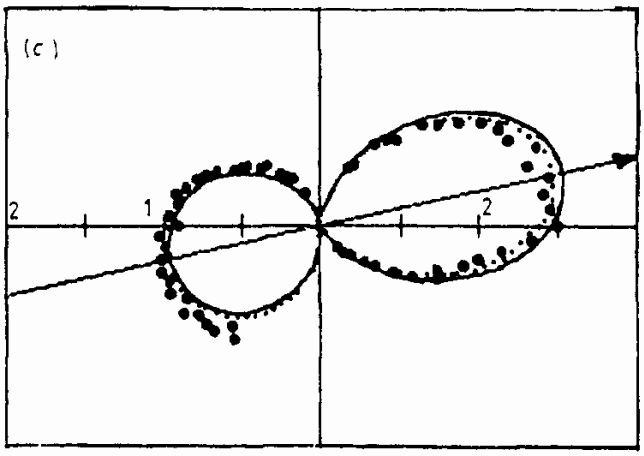

Figure 2.3: Experimental fully differential cross section for (e,2e) on He at an impact energy of $E_0 = 4\,\mathrm{keV}$. The points show the emission pattern in the scattering plane, where the emitted electron has 20 eV energy and at the projectile is scattered with an angle of $\theta_1 = 0.75°$ with respect to the incoming beam axis. The curve denotes a first Born calculation, the arrow the direction of the momentum transfer $\vec{q}$. Different scales are used in the left and right half of the polar plot. (From [DCLB$^+$87])

These features are not only valid for single ionization but apply to the cross section of all processes within the first order description.

Double Ionization

In double ionization the two bound electrons change their quantum state and the interaction with the projectile by one virtual photon, which is a one particle interaction, only leads to non-zero cross section when a correlated treatment of the bound electrons is used. Basically there are two physical processes which lead to a transition of both electrons after a single interaction via one virtual photon. First, so-called shake processes, where one electron is ejected by the interaction with the projectile, leaving the second electron in the continuum of the doubly-charged ion. Second, the projectile interacts with one of the bound electrons, which ionizes the other bound electron in an internal inelastic e^--He^+ scattering process.

Just like in the case of single ionization, the FDCS in double ionization of helium by fast electron impact is governed by the 'photon-like' interaction and the resulting selection rules. The strong similarity between double-ionization of helium by a photon and by fast particles was impressively shown in complete pictures of the break-up process obtained in an (e,3e) experiment using the reaction microscope [DKS$^+$01]. The angular distribution for electron emission of two electrons with the same energy (5 eV) is

shown in Fig. 2.4 for double ionization by photon (linearly polarized) and by 2 keV electron-impact at small momentum transfer. Both spectra show the fully differential cross section in the plane of the polarization axis, or in case of particle impact in the plane containing the momentum transfer ($|q| = 0.6$ a.u.). For a better comparison, the direction of the polarization axis $\theta_{\hat{e}}$ is chosen to be the same as the direction of the momentum transfer θ_q. When the emission of the ejected electrons is viewed in the scattering plane, the FDCS is now differential in the planar emission angle θ_1 and θ_2 of the two outgoing electrons. As both electrons have identical energy and are therefore indistinguishable, the cross section is symmetric with respect to the diagonal, where $\theta_1 = \theta_2$.

For double ionization by a single photon, the FDCS can be parametrized by following function [HSWM91]:

$$d\sigma(\theta_1, \theta_2) \propto (\cos(\theta_1 - \theta_{\hat{e}}) + \cos(\theta_2 - \theta_{\hat{e}}))^2 \cdot G(\Delta\theta). \tag{2.6}$$

The cosine squared distribution for the coplanar emission angles θ_1 and θ_2 of both ejected electrons which incorporates the dipole-selection rules and a 'correlation' factor $G(\Delta\theta)$, which accounts for the final state repulsion of the electrons. The correlation factor suppresses the emission in equal directions ($\theta_1 = \theta_2$). The lines displayed in both figures mark the angles, at which the dipole-selection rule forces the cross section to be zero. The direction of the polarization axis and momentum transfer is indicated by the dot at $\theta_1 = \theta_2 = 60°$.

For photoionization the resulting cross section exhibits four peaks of equal height, which are the analogy to the dipole emission pattern shown for single ionization. The cross section has to point-symmetric with respect to the angular position of the polarization axis or momentum transfer, which is intrinsically included in the parametrized cross section. For charged particle double ionization, the experimental cross section has very similar features with two pairs of peaks appearing, which have different height. These are the corresponding binary and recoil peaks for known from (e,2e) and the different peak heights can be explained by higher multipoles which appear at finite q. However, the pair of 'broad' peaks is slightly shifted, breaking the symmetry with respect to $\vec{q}$. This is already a signature of a higher order process, which cannot be described by one-photon exchange and is a consequence of the high sensitivity of the fully differential cross section to the underlying dynamics. However, the dipole-selection rule seems to be fulfilled quite well for charged particle impact. Usually, the two low-energetic electrons which have the same energy will leave the reaction in opposite direction, because of their repulsion (black solid lines in Fig. 2.4). It is therefore most noteworthy, that this back-to-back configuration of the electrons is strongly suppressed due to the dipole selection rule.

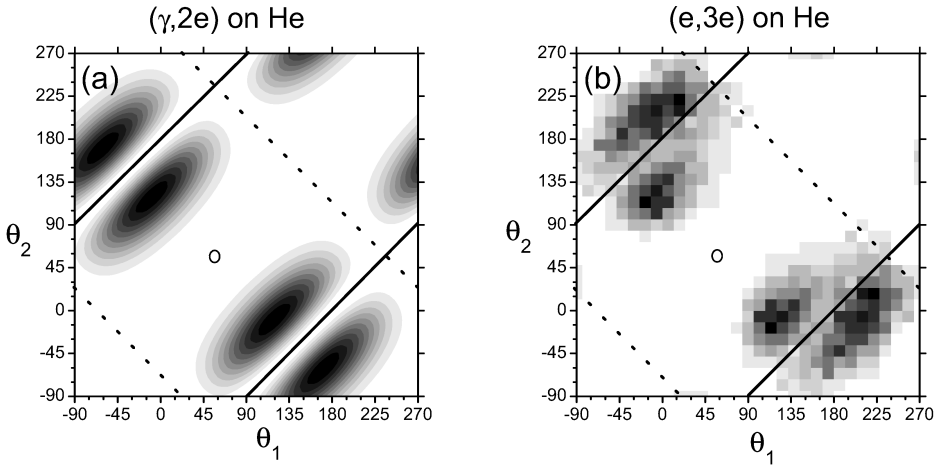

Figure 2.4: Fully differential cross section for double ionization of helium calculated for photo double-ionization (left) and measured with 2 keV electrons (right). The plotted cross sections show the angular emission of two electrons with 5 eV energy in the plane containing the momentum transfer $\vec{q}$ ($|q| = 0.6$ a.u.) in the case of charged particle impact, and in the plane of the polarization axis in the case of photon impact. The circle indicates the direction of the polarization axis and the momentum transfer, respectively. The angles, at which the dipole selection-rule predicts a node in the cross section, are marked by solid and dotted lines. (from [DKS+01])

2.1.2 Beyond 'One-Photon'-Exchange

So far, the discussion was restricted to processes which can be described by the exchange of one photon. However, at reduced projectile velocities, or when one looks very closely (for instance fully differential), effects from multi-photon exchange will appear. In the formal treatment within the Born series, higher order interactions lead to an interesting effect. When the next higher order of the Born expansion is included in the total transition amplitude, then the first and second order term of the scattering amplitude, T_{fi}^{B1} and T_{fi}^{B2}, have to be added coherently in the cross section:

$$\sigma_{fi} = |T_{fi}^{B1} + T_{fi}^{B2}|. \tag{2.7}$$

Apart from the incoherent squares of the amplitudes, a cross-term appears. In the cross section of eq. (2.7) the perturbation $\eta = Z_P/v_P$ can be extracted which leads to the expression

$$\sigma_{fi} \propto c_1 \left(\frac{Z_P}{v_P}\right)^2 + c_2 \left(\frac{Z_P}{v_P}\right)^3 + c_3 \left(\frac{Z_P}{v_P}\right)^4 + \cdots, \tag{2.8}$$

where the coefficients c_i do not explicitly depend on Z_P/v_P. The second term in eq. (2.8) is the cross-term, which is charge sign dependent due to the η^3 dependence, and is a result from the interference of second and first order amplitude. The interference is the leading contribution of higher orders when including the second Born amplitude. From this representation, it becomes clearly visible, that higher orders can be neglected, as long as $\eta \ll 1$ (in a.u.). At larger perturbations η the influence of higher orders gets stronger, and the perturbative Born description is inadequate.

Single Ionization

How higher order effects are observed in (e,2e) experiments is demonstrated in Fig. 2.5. If the impact energy of the projectile is reduced, the velocity of the incoming projectile is eventually so low, that its presence significantly 'distorts' the initial bound state of the atom such that it cannot be considered frozen in its asymptotic unperturbed state. The same is true for the final state, where the so-called post-collision interaction between the outgoing projectile and the target fragments has to be included. One way to achieve this is to include the next order of the Born series, which describes the ejection process by the exchange of two virtual photons between the projectile and target. Within this description, the projectile either scatters elastically of the neutral target and ejects an electron on a further step, or the projectile ionizes the target and interacts either with the singly charged He^+-ion, the bound electron, or the ejected electron. In the fully differential cross section, the deviation from the first Born description can be seen in the measurement at $E_0 = 500\,\mathrm{eV}$ impact energy (which corresponds to

a perturbation strength of $\eta = 0.15$ a.u.) reported by Ehrhardt [EFJ$^+$82], where the emission pattern exhibits an angular shift of the binary and recoil lobe with respect to the momentum transfer $\vec{q}$ (Fig. 2.5). The second Born calculation reproduces the shift and also provides a better prediction for the height of the binary and recoil peak. For negative projectiles the shift is directed backwards, in opposite direction of the outgoing projectile. For positively charged ions a similar shift has been observed, which tends to the opposite direction, namely in forward direction towards the outgoing projectile and is commonly attributed to the projectile-ejected electron interaction [HMF$^+$04].

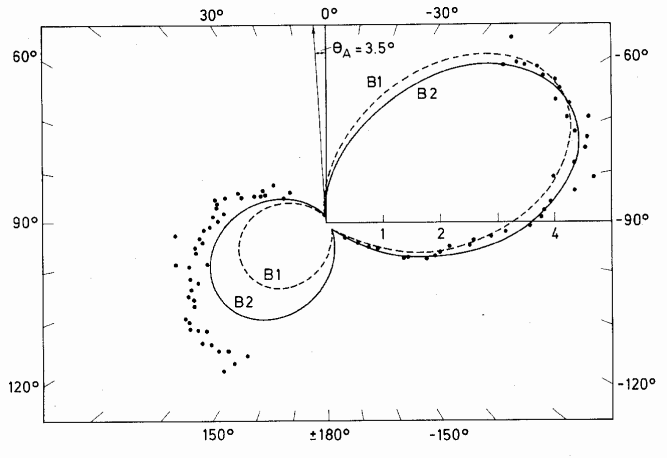

Figure 2.5: Fully differential cross section displaying the dipolar pattern for single ionization of helium by 500 eV electron impact, a scattering angle of 3.5° and an energy of the ejected electron of 5 eV. The curves represent a first (B1) and second Born (B2) calculation. (From [EFJ$^+$82])

The dynamics gets more complex at very low impact energies, where the incoming projectile is slow. Here the intuitive picture of describing the interaction as an exchange of several photons cannot be applied to explain the general features of the cross section. An example is shown in Fig. 2.6, where the FDCS is shown for (e,2e) on hydrogen at an impact energy of $E_0 = 17.6$ eV. The outgoing electrons are chosen to have equal energy of 2 eV each, and the scattered projectile cannot be identified in the final state. In this regime the coupling between all collision partners has to be treated on equal footing and the separation of the system into a 'projectile' interacting via photon exchange with the 'target' is not appropriate. Accordingly, the non perturbative calculation of the cross section represents a full and 'exact' numerical solution to the three-body Schrödinger equation. The observed agreement at this low impact energy, also between the two calculation methods (dubbed ECS and CCC, see sec. 2.2.3), has generally lead to the conclusion, that the so called three-body Coulomb problem is essentially

solved.

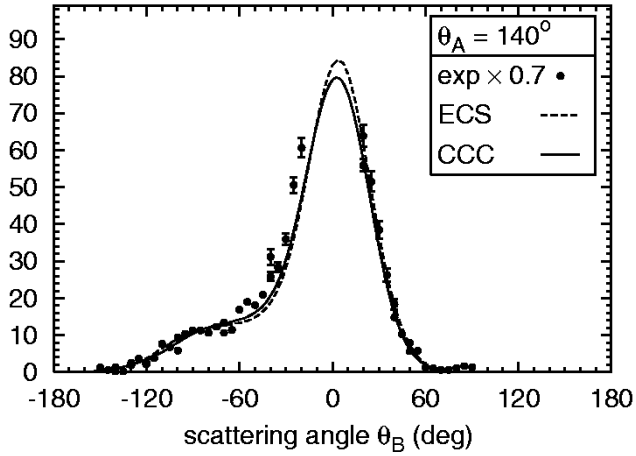

Figure 2.6: Absolute fully differential cross section (in $10^{-20} cm^2 sr^{-2} eV^{-1}$) for single ionization of hydrogen at 17.6 eV impact energy and for equal energy sharing of the outgoing electrons. (From [Bra02])

The revolutionary imaging technique used in reaction microscopes, represented a big step forward in the study of few-body dynamical problems and was first used in ion impact [MFK03, UMD$^+$03]. Here a large fraction of the final phase-space after fragmentation of atoms or molecules could be covered, which for the first time allowed to measure fully differential cross section using ions as projectiles, and at the same time provided insight into the collision process going well beyond what was possible in (e,2e) experiments. In the fully differential cross section taken as three-dimensional images in fast (100 MeV/u C^{6+}) ion-impact ionization of helium [SMF$^+$03], higher order effects are clearly revealed in the plane perpendicular to the momentum-transfer (Fig. 2.7). Here the surprisingly strong emission exhibits a strong anisotropy at a perturbation of $\eta = 0.1$ a.u., which is a clear indication of the presence of higher order interactions. The out-of-plane geometry provides a much greater sensitivity to higher order interactions and also to theoretical descriptions. The calculation shown in Fig. 2.7 represents one of the most sophisticated models for ion-impact ionization and has proven to be very successful describing doubly differential cross sections even at large perturbations η, where higher order effects are far stronger [MFS$^+$99]. Only the full image of the angle resolved cross section reveals the full underlying dynamics at a given momentum transfer and ejected electron energy. Although (e,2e) experiments have been performed since more than 35 years, three-dimensional images have not been available for electron impact and therefore the well advanced theoretical models which have been developed for electron impact ionization still lack an ultimate benchmark

for the description of singly ionizing collisions with helium. The aim of this work is to solve this deficiency: with the refinements of the reaction microscope three-dimensional cross section images can now be provided for electron impact, which are presented in 4.1.

Double Ionization

The importance of second order processes in double ionization lies in the nature of the double-ejection process: since both bound electrons participate, the ejection by two subsequent knock-outs by the projectile, described by the two virtual photon exchange, contributes significantly to the cross section.

On the fully differential scale, a clear indication of higher order process is the missing symmetry with respect to the momentum transfer axis, which can be already observed in Fig. 2.4 at an impact energy of 2 keV. The main features, however, are contained in the first order description [DKS$^+$01]. To provide some guidelines, further (e,3e) experiments at reduced projectile energy have been performed with conventional electron-spectrometers [TLBDA98, LBDG$^+$01, LBDC$^+$03] and with the reaction microscope [DMS$^+$99, DKS$^+$01, DKS$^+$03], where the detailed information on the dynamics in different kinematical situations was gained. The result of the latter experiment is displayed in Fig. 2.8 together with a First and Second Born CCC calculation. The elaborate consideration of effects like the post-collision interaction of the outgoing projectile with the ejected electrons, is not possible at the present status. Hence the achieved agreement of the second Born is quite satisfactory with respect to the angular emission pattern. The description by the exchange of two virtual photons seems to provide a consistent explanation of the major features of the cross sections obtained in the reaction microscope measurement. Calculations which attempt to include higher orders in the projectile target interaction still rely on approximations and are subject of intensive efforts [Khe04, ECLBC05].

There are still several remaining open questions, like the comparison with theory on absolute scale of the cross sections and the importance of higher orders going beyond the exchange of two virtual photons.

So far, (e,3e) experiments have not yet been performed at very low impact energies close to the ioniziation threshold. In this regime the coupling between all four particles should become equally strong, and the description within different orders of interaction should break down. Then, the interactions between all particles, three electrons and the ion, have to be described non-perturbatively. In the present work, experimental (e,3e) cross sections in this regime are presented in chapter 4.3, which provide a real benchmark for descriptions of the full four-body process.

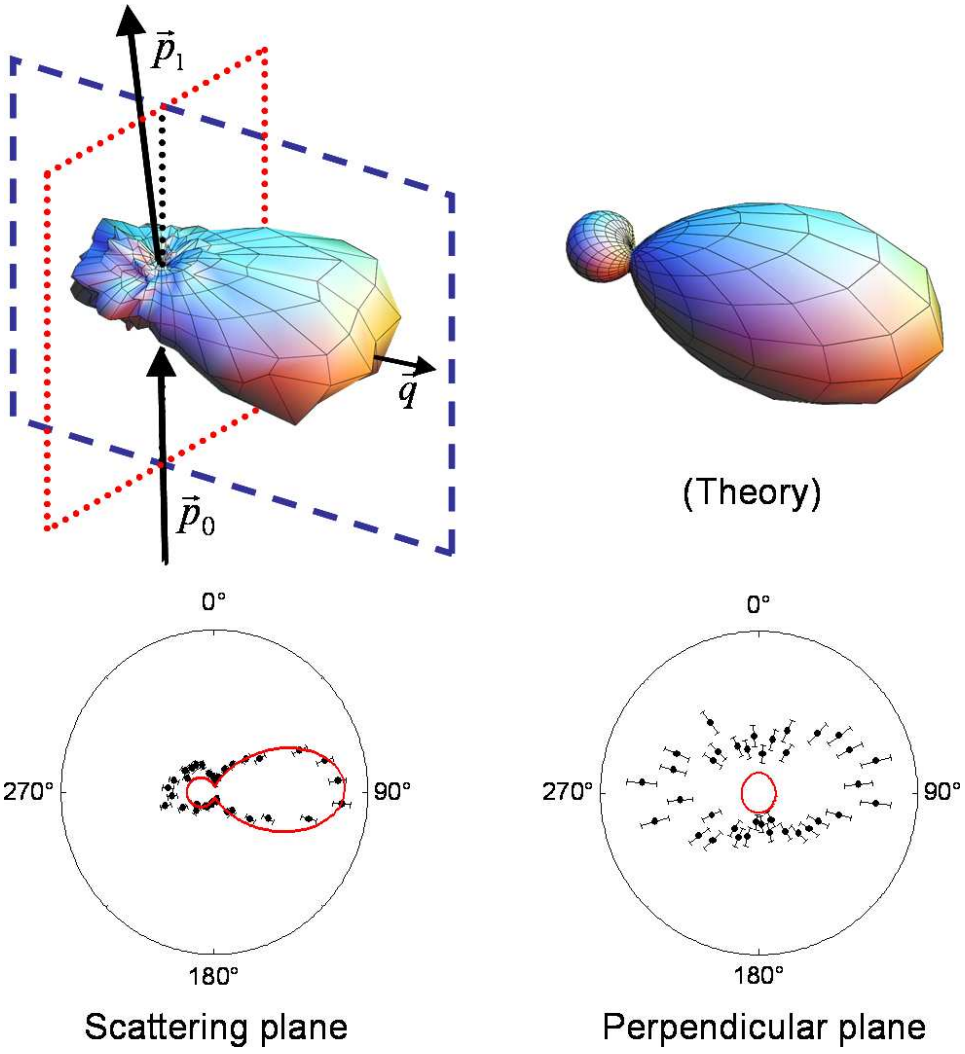

Figure 2.7: Three dimensional FDCS for single ionization by 100 MeV/u C^{6+} ions at $|q| = 0.75$ a.u. and $E_2 = 6.5$ eV [SMF+03]. For a quantitative comparison on an absolute scale, cuts in two selected planes were applied, where the scattering (perpendicular) plane is indicated by dashed (dotted) lines. The comparison shown in the bottom part of the figure shows a strong disagreement for the 'perpendicular' plane between the experimental data and a calculation using distorted waves.

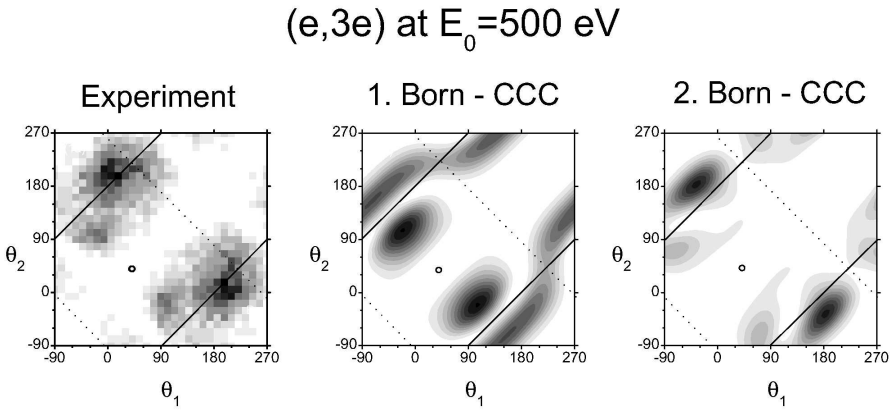

Figure 2.8: The fully differential cross section for the emission of two electrons with equal energy $E_1 = E_2 = 5\,\mathrm{eV}$ in the coplanar geometry and an impact energy of $E_0 = 500\,\mathrm{eV}$ and an amount of the momentum transfer of $|q| = 0.8$. The circle indicates the direction of the momentum transfer. Left: Experimental FDCS; Middle : 1. Born CCC calculation; Right : 2. Born CCC calculation. (From [DMS$^+$99])

2.2 Theory: A Brief Summary

The dynamics of several interacting particles can be described by the Schrödinger equation, which can be seen as the quantum mechanical equivalent to the equations of motion in classical mechanics. When it comes to practical calculation, one is confronted with serious difficulties especially for time-dependent problems. As for classical many-particle problems there is no analytical solution to the time-dependent few-body quantum problem for more than two interacting particles. Collision induced ionization of an atom represents an example, where the dynamics is predominantly ruled by the long-range Coulomb interaction. Even with the increasing computational resources available, using 'brute force' in order to directly solve the Schrödinger equation was not tractable until the formal foundations leading to a mathematically consistent prediction were laid. Already for the simplest dynamical few-body problem with three interacting particles, single ionization of hydrogen by low energy electron impact, the key to a proper solution was not found until 1999 [RBIM99]. Presently two frameworks, the 'Exterior Complex Scaling' and the 'Convergent Close Coupling', claim to be able to solve the three-body Coulomb problems realized in fragmentation reactions like single ionization of hydrogen by electron impact and double ionization by photon impact. In quantum mechanics textbooks, the scattering problem is often described in a simplified manner, however, many theoretical models in atomic scattering theory use a so-called 'time-dependent' formalism of scattering problems, which will be briefly sketched in the present chapter. One aim is to show some of the great difficulties in the description of dynamical few-body quantum systems is confronted with. Some approximative formulations, the most prominent being the Born-series, will be presented in section 2.2.2. The basic ideas behind the theoretical approaches claiming to provide an exact solution of the few-body Coulomb problem are handled in section 2.2.3. The choice of the presented methods is restricted to those, which are regarded to be relevant for the topics discussed in this work. Atomic units are used throughout the following discussion (see A.3).

2.2.1 General Considerations

Scattering processes in general are quite particular, when they are regarded as a time dependent problem. The projectile, initially considered as a free particle, impinges on the target and some interaction will take place which may induce a reaction or, in quantum-mechanical terms, a transition. Eventually, the final state particles (i.e. the emerging 'reaction' products) are considered to be free. More precisely, the situation can be described by the incoming projectile, which is free in the remote past ($t \to -\infty$) before it interacts with the target, which would be described by the asymptotic initial state Φ_i. The collision fragments leaving the reaction are free in the

far future ($t \rightarrow +\infty$) and are described as free-particle wavefunctions in the final state Φ_f. The coupling between the incoming projectile and the target at a finite time can then induce a transition into the final-state and hence atomic scattering represents a time-dependent problem. In order to specify an atomic collision process without entering into the details of the dynamics, the transition from the initial state Φ_i to the final state Φ_f can be written down in terms of a reaction. Taking the example of one of the simplest realization of a dynamical three-body Coulomb problem, electron scattering on atomic hydrogen, following reactions exist:

$$e + H \rightarrow e + H \tag{2.9}$$
$$e + H \rightarrow e + H^* \tag{2.10}$$
$$e + H \rightarrow e + e + p \tag{2.11}$$

In the first, the projectile scatters elastically and in the second excites the target to a higher-lying bound state. The third reaction is sometimes referred to as a 'rearrangement' collision, where the atom breaks into two fragments. The long-range between all outgoing particles has to be considered, which leads to increased difficulties in the theoretical description. Each reaction specifies the Hamiltonian, which is decomposed in two parts, describing the asymptotic collision system and the interaction during the collision:

$$\begin{aligned} H &= H_i + V_i \\ H &= H_f + V_f. \end{aligned}$$

The indices denote the initial (i) and final channel (f), respectively. The decomposition is chosen such, that the 'perturbation' $V_{i,f}$ vanishes asymptotically. For atomic scattering one can write $H_i = H_{Target} + H_{Projectile}$ and V_i is the Coulomb interaction between the projectile and the constituents of the target-atom. As different channels exist, the total Hamiltonian may separate differently in the final state than in the initial state, depending on the channel under consideration. For the first two reactions in eq. (2.9) $H_i = H_f$ and $V_i = V_f$, which simplifies the description considerably opposed to the fragmentation, where these identities are not fulfilled. The decompositions of the Hamiltonians define the asymptotic eigenstates by

$$\begin{aligned} H_i|\Phi_i\rangle &= E_i|\Phi_i\rangle \\ H_f|\Phi_f\rangle &= E_f|\Phi_f\rangle. \end{aligned}$$

These asymptotic states represent the 'unperturbed' system, where all collision partners are free. These will be perturbed due to the interaction $V_{i,f}$ between the particles, and it is in the nature of the scattering process that this interaction is time-dependent since it is switched on and off before

and after the collision process, respectively. The dynamics of the quantum mechanical system represented by the state $|\Psi(t)\rangle$ is given by the well known time-dependent Schrödinger equation:

$$i\hbar\frac{\partial}{\partial t}|\Psi(t)\rangle = H|\Psi(t)\rangle, \tag{2.12}$$

where the Hamiltonian contains the information on the collision dynamics. It is generally said, that the state-vector and the operator both are represented in the 'Schrödinger-picture'. Facing the nature of the scattering problems, the formulation in eq. (2.12) is not particularly convenient: in the Schrödinger picture the operators are time-independent (apart from the explicit time-dependence) and the time dependency is included in the description of the state. A more appropriate description would use a time-dependent description for the state and similarly for the perturbation V, such that the interaction vanishes when all collision partners are infinitely apart.

Different representations of the Schrödinger equation can be found, since the vector $|\Psi(t)\rangle$ and any operator A in Hilbert-space can be rotated by a unitary transformation

$$|\Psi(t)'\rangle = U|\Psi(t)\rangle \tag{2.13}$$
$$A' = UAU^{\dagger}. \tag{2.14}$$

In principle an infinite number of representations is possible. In the first step the Hamiltonian (in the Schrödinger picture) is split into two parts

$$H = H_0 + V. \tag{2.15}$$

The term H_0 represents the unperturbed system and V the perturbation, in the sense that $V \to 0$ for $t \to \pm\infty$. The operator for the transformation into the 'interaction picture' as in eq. (2.13) is chosen to be $U_I(t, t_0) = \exp\{iH_0(t - t_0)\}$, such that

$$|\Psi_I(t)\rangle = \exp\{iH_0(t - t_0)\}|\Psi(t)\rangle. \tag{2.16}$$

Similarly, one can transform the operator V like in eq. (2.14) resulting in a time-dependent perturbation V_I(t). The time evolution of the state is now given by an equation which is obtained by inserting $|\Psi(t)\rangle$ into the Schrödinger equation (2.12)

$$i\frac{\partial}{\partial t}|\Psi_I(t)\rangle = V(t)|\Psi_I(t)\rangle, \tag{2.17}$$

called 'Tomonaga-Schwinger Equation'. In the description one imposes that the interaction will be 'switched on' during the collision, but is 'switched off' asymptotically. The interaction representation is then ideally suited for

scattering experiments: Starting with the initial state of free particles $\Psi(t \rightarrow -\infty) = \Phi_i$, the state will 'evolve' only when the interaction is active by virtue of eq. (2.17) and thus the state $|\Psi(t)_I\rangle$ is time-dependent. The operators in the 'interaction-picture' are time-dependent given by the transformation in eq. (2.14)

Scattering Matrix

The asymptotic state Φ_i in the remote past ($t \rightarrow -\infty$) evolves into the eigenstate $|\Psi_i^+\rangle$ of the total Hamiltonian by means of the time-evolution operator, which in the interaction picture is defined by

$$U(t, t_0) = \exp(iH_0 t) \exp(-iH(t - t_0)) \exp(-iH_0 t_0). \tag{2.18}$$

Similarly the asymptotic final state in the far future ($t \rightarrow \infty$) can be developed backwards into $|\Psi_f^-\rangle$. The scattering wavefunctions, which are solutions of the time-dependent Schrödinger equation fulfilling the correct asymptotic boundary conditions, can be written as

$$|\Psi_i^{(+)}\rangle = \lim_{t \rightarrow -\infty} U(t_0, t)|\Phi_i\rangle \tag{2.19}$$

$$|\Psi_f^{(-)}\rangle = \lim_{t \rightarrow +\infty} U(t_0, t)|\Phi_f\rangle, \tag{2.20}$$

with $U(t, t_0)$ defined above. It is said that $|\Psi_i^{(+)}\rangle$ fulfills 'outgoing wave' boundary conditions. In the same way the asymptotic final state can be developed from $+\infty$ to t_0 which results in $|\Psi_f^-\rangle$ fulfilling 'incoming wave' boundary conditions. Suppose now that the exact form of the scattering waves are known, how does Φ_i in the remote past ($t \rightarrow -\infty$) relate to the state Φ_f in the far future ($t \rightarrow +\infty$)? This relation is expressed by the scattering matrix

$$S_{fi} = \langle \Phi_f | S | \Phi_i \rangle = \langle \Psi_f^{(-)} | \Psi_i^{(+)} \rangle \tag{2.21}$$

with the collision operator defined as

$$S := \lim_{\substack{t' \rightarrow -\infty \\ t \rightarrow \infty}} U(t, t_0) U(t_0, t') \tag{2.22}$$

The S-matrix in is time independent. The formal expression in eq. (2.21) expresses the amplitude for a system initially in the state Φ_i to get into the final state Φ_f. Finally, eq. (2.21) leads to following expression [Joa] :

$$\langle \Phi_f | S | \Phi_i \rangle = \delta_{if} - i \frac{(2\pi)^4}{\mathcal{V}} \delta(E_i - E_f) \delta(\vec{P_i} - \vec{P_f}) \langle \Phi_f | V_f | \Psi_i^+ \rangle, \tag{2.23}$$

where $\mathcal{V}$ is the total volume and $\vec{P_{i,f}}$ is the center-of-mass momentum in the initial and final state, respectively. The delta functions ensure energy and

momentum conservation. The delta-function δ_{if} in the collision matrix leads to an infinite amplitude, since the time considered is infinite. The second term of the scattering-matrix is the non-trivial part describing transitions from the initial to the final state and the matrix element $\langle\Phi_f|V_f|\Psi_i^+\rangle$ is called the T-Matrix T_{fi}. It describes the amplitude for the transition of the scattering state vector Ψ_i^+ to the final state Φ_f under the acting interaction V_f in the outgoing channel. The interaction V_i is already included in the scattering state, so that the information of all interactions of the entire scattering process in the initial and final state are included. The S-matrix presented in eq. (2.23) is the so-called prior-form, however there is a second representation, the so called post-form of the collision matrix, which provides an equivalent description:

$$\langle\Phi_f|S|\Phi_i\rangle = \delta_{if} - i\frac{(2\pi)^4}{\mathcal{V}}\delta(E_i - E_f)\delta(\vec{P}_i - \vec{P}_f)\langle\Psi_f^-|V_i|\Phi_i\rangle. \tag{2.24}$$

The transition probability $P_{fi} = |\langle\Psi_f^-|\Psi_i^+\rangle|^2$ per unit time is given by

$$w_{fi} = i\frac{(2\pi)^4}{\mathcal{V}}\delta(E_i - E_f)\delta(\vec{P}_i - \vec{P}_f)|T_{fi}|^2, \tag{2.25}$$

which gives the vital quantity accessible in the experiment. The measured cross section is the transition rate normalized to the incident flux of projectiles, which is given by $v_p/\mathcal{V}$, where v_p is the velocity of the incoming particle beam and under the assumption, that only one projectile is in the volume.

$$\sigma_{fi} = i\frac{(2\pi)^4}{v_p}\delta(E_i - E_f)\delta(\vec{P}_i - \vec{P}_f)|T_{fi}|^2, \tag{2.26}$$

In order to calculate the cross section the T-matrix has to be evaluated. To achieve this a solution for the scattering state Ψ_i^+ or Ψ_f^- has to be found.

The Lippmann-Schwinger Equation

The (stationary) Schrödinger equation can be written as an inhomogeneous equation :

$$(H_i - E)|\Psi_i\rangle = V_i|\Psi_i\rangle. \tag{2.27}$$

The formal solution $|\Psi_i\rangle = GV_i|\Psi_i\rangle$ is obtained by means of the Greens-operator

$$G = \lim_{\epsilon\to 0}\frac{1}{E_i - H_i \pm i\epsilon}, \tag{2.28}$$

and thus

$$|\Psi_i^{(\pm)}\rangle = \Phi_i + \lim_{\epsilon\to 0}\frac{1}{E_i - H_i \pm i\epsilon}V_i|\Psi_i^{(\pm)}\rangle. \tag{2.29}$$

The scattering state $\Psi_i^{(\pm)}$ fulfilling the correct boundary conditions can also be obtained from eq. (2.19), which will not be presented here (see [Joa]). The eq. (2.29)is known as 'Lippman-Schwinger' equation, which is an integral equation for $|\Psi_i\rangle$ and solves Schrödinger equation under correct boundary conditions[2].

The formal expressions presented here form the basics for theoretical models developed to describe atomic fragmentation processes. Now that all ingredients for the transition amplitude T_{fi} seem to be formally present, the problem of its actual calculation has to be addressed. One way is to introduce approximations, which may even allow to gain analytical expressions for the cross section. The most famous approximation leading to the Born series should lead to an appropriate description, where the dynamics due to the incoming projectile can be treated perturbatively. A full solution of the Schrödinger equation in order to treat ionizing collisions already seemed to be an insuperable task already for the simplest problem, namely single ionization of hydrogen by electron. Although the mathematical theory had been worked out in the 1960's by Peterkop [Pet77] and simultaneously by Rudge and Seaton [RS65, Rud68], the form of asymptotic boundary conditions to the scattering wave of three continuum particles was so intractable, that a numerical solution could not be found until an adapted formulation was found by Rescigno et al. in 1999 [RBIM99]. Another type of calculation method uses pseudostate representations of the continuum - like the Convergent Close Coupling (CCC) [Bra02] or R-matrix calculations [BHS$^+$96] - where the former claims to be able to calculate exact transition amplitudes for three-body Coulomb systems. However, the formal basis was not completed until 2003, when a practical formulation for the extraction of the transition amplitude for electron atom ionization was presented, that is free of ambiguity and divergence problems [KMSB03, KMSB04]. For electron-impact single ionization of hydrogen and for single-photon double ionization on helium the two calculation methods ECS and CCC achieve very good agreement with experimental data even at very low projectile energies. These experiments and the performed calculations can bee seen as 'proof of principle' which form the starting point for more complex problems starting with charged particle impact ionization of few-electron targets like helium. Another field with potential of further progress is the ionization with positively charged particles (e^+ and ions), where the binding potential of the projectile leads to additional effects.

[2]The equivalent equations also exist for the final state representations

2.2.2 Approximative Methods

The Born Series

The Born series is obtained by iteratively solving the Lippman-Schwinger equation (eq. (2.29)), which is achieved by setting $|\Psi_i^{(+)}\rangle = |\Phi_i\rangle$ on the right-hand side in the first iteration. Continuous iteration leads to the series

$$|\Psi_i\rangle = |\Phi_i\rangle + G_i V_i |\Phi_i\rangle + G_i V_i G_i V |\Phi_i\rangle + \dots \tag{2.30}$$

which is called the Born series. It should be noted that the same series can be written in the 'post-form'. In the further discussion only the prior-form will be considered and therefore the subscript in G and V will be omitted. The transition matrix-element simplifies to

$$T_{fi} = \langle \Phi_f | V | \Phi_i \rangle + \langle \Phi_f | V G V | \Phi_i \rangle + \dots \tag{2.31}$$

as only the asymptotic wavefunctions appear. The Born series corresponds to an expansion in powers of the 'perturbation' V and therefore convergence is expected in the regime, where the interaction V is weak. For fragmentation reactions the perturbation is the Coulomb interaction between the projectile and the target constituents. For sufficiently 'fast' projectiles, this interaction becomes 'weak' due to the short interaction time and the first term in eq. (2.30) dominates the cross section. The Born approximation cannot be applied for low-energy electron impact, since all terms of the series contribute and a perturbative treatment is not justified. So far the evaluation of the second Born amplitude remains challenging, such that the third Born term is considered to be beyond reach of practical calculation.

The First Born Approximation

The initial state is expressed by a product of a plane wave describing the incoming projectile having momentum $\vec{k_i}$ and the eigenstate of the target (i.e. $|\Phi_i\rangle = |\vec{k_i}\rangle |\phi_i\rangle$). In the final-state the scattered projectile is described as plane wave, which means that the interaction of the scattered projectile with the fragments is neglected, and is just the result from taking only the first term of the Born expansion in eq. (2.31). This is the so-called first Born approximation (FBA). For the collision with an atom with N electrons, the perturbation is entirely due to the Coulomb interaction between the incoming projectile and the target constituents

$$V = -\frac{Z_P Z_T}{r_P} + \sum_{i=1}^{N} \frac{Z_P}{|r_P - r_i|}, \tag{2.32}$$

where Z_P is the projectile charge, r_P the projectile coordinate, r_i the electron coordinates. In the transition amplitude the first term, which describes

the interaction of the projectile with the nucleus vanishes due to the orthogonality of the initial and final target states.

The first Born transition amplitude is given by

$$T_{fi}^{B1} = \frac{Z_P}{2\pi^2 q^2}\langle\phi_f|\exp i(\vec{q}\cdot\vec{r})|\phi_i\rangle, \tag{2.33}$$

with the momentum transfer $\vec{q} = \vec{k_i} - \vec{k_f}$. In the FBA the dynamics is determined by the momentum transfer and the matrix element in eq. (2.33). For single ionization, the final-state $|\phi_f\rangle$ is the product of a continuum electron and the residual target. The ejected electron can be expressed by a Coulomb wave describing its motion in the field of the residual ion. The only properties of the scattered projectile appearing in eq. (2.33) are its charge Z_P and the momentum transfer $\vec{q}$. This way the three-body system is reduced to a two an effective two-body problem consisting of the ejected electron and the residual ion. Similarly for double ionization, the four-body system is reduced to an effective three-body problem. The ionization process depends only on the 'strength' of the electric field which enters through the projectile charge Z_P and how strongly the 'momentum-kick' $\vec{q}$ from the collision was. Alternatively, this can be seen as the exchange of a virtual photon, through which the momentum and energy is transfered to the target.

Even in the regime, in which the first Born approximation can be expected to be valid, the calculation of the amplitude in eq. (2.33) is far from trivial. When the asymptotic states Φ_i and/or Φ_f are not known exactly, the equivalence of post- and prior-form is no longer valid, and spurious contributions in the evaluation of the transition amplitude may appear. Keeping in mind, that there is no analytical representation of the ground state of the simplest two-electron system like He, already correlated processes like excitation-ionization or double-ionization can be challenging in the first Born approximation (e.g. [KBB99]).

The Fully Differential Cross Section Very detailed information is given by the fully differential cross section, when all momentum vectors of in the initial and final state are determined and all kinematical variables (or if one likes 'quantum numbers') are known. In the FDCS for single-ionization and ionization-excitation all three momentum vectors of the three final state particles have to be fixed. A very common representation of the 'triply differential cross section' (TDCS) is $d^3\sigma/d\Omega_1 d\Omega_2 dE_2$, where $d\Omega_{1,2}$ denote the emission angles of the two outgoing electrons and dE_2 is usually the energy of the ejected electron. These three parameters fix the momentum vectors of all final state particles via momentum and energy conservation. In double-ionization with four final-state continuum particles, the fully differential cross section is fivefold differential and, in analogy to the TDCS,can be expressed as $d^5\sigma/d\Omega_1 d\Omega_2 d\Omega_2 dE_2 dE_3$, where the emission-angle and energy of the third final-state electron enters.

The FDCS in the first order has following behaviour:

$$\text{FDCS} \propto \left(\frac{Z_P}{v_P}\right)^2 \frac{1}{q^4}\langle\phi_f|\exp(i\vec{q}\cdot\vec{r})|\phi_i\rangle, \tag{2.34}$$

which shows the dependence on the momentum transfer $\vec{q}$, which strongly determines the dynamics of the collision at a given impact energy. The energy of the ejected electron enters into the first Born amplitude through the matrix element, which only contains properties of the target-atom and the operator $\exp(i\vec{q}\vec{r})$, describing the first order interaction. The momentum-transfer is the only remaining vector and therefore represents a quantization axis in the collision. An important point in eq. (2.34) is the q^4 dependence, which resembles the cross section in Rutherford scattering and reveals that most ionizing collisions in the first order regime occur at low momentum transfer.

A further approximation is achieved by expanding the exponential

$$\exp(i\vec{q}\vec{r}) = 1 + i\vec{q}\vec{r} + \cdots, \tag{2.35}$$

where the higher powers of $\vec{q}$ can be neglected for small momentum transfer, which is the so-called dipole approximation or the photoionization limit. The constant term vanishes, when the matrix element is evaluated due to the imposed orthogonality of the initial and final target states. In the dipole approximation the operator of the interaction $i\vec{q}\vec{r}$ shows a strong analogy with the dipole operator describing the interaction with a photon $i\hat{e}\vec{r}$, $\hat{e}$ being the polarization axis.

Second Born Approximation

The second Born amplitude is given by the second term of the Born series

$$T_{fi}^{2B} = \langle\phi_f|VGV|\phi_i\rangle \tag{2.36}$$

$$= \lim_{\epsilon\to 0}\langle\phi_f|V\frac{1}{E - H_0 + i\epsilon}V|\phi_i\rangle, \tag{2.37}$$

where H_0 stands for the unperturbed Hamilton operator. The second order amplitude can be seen as a single interaction of the projectile with the target expressed by the first V, then the projectile propagates freely,which is expressed by the Greens operator G, before it interacts a second time again expressed by the interaction V. The product of the target eigenstate $|\phi_n\rangle$ and the plane wave representing the projectile $|\vec{k_P}\rangle$ be the complete set of eigenvectors of the unperturbed system. Then the expression of eq. (2.36) can be written as:

$$T_{fi}^{2B} = \lim_{\epsilon\to 0}\sum_n \int d^3\vec{k'_P}\frac{\langle\phi_f|V|\vec{k'_P}\rangle|\phi'_n\rangle\langle\phi'_n|\langle\vec{k'_P}|V|\phi_i\rangle}{E - E_n - E_{P'} + i\epsilon}, \tag{2.38}$$

where $|\phi_n\rangle$ includes bound and continuum states of the target atom. Here the integration runs over the intermediate momenta of the projectile $|\vec{k_{P'}}\rangle$ and continuum states of $|\phi_n\rangle$ and the sum runs over the intermediate target-states $|\phi_n\rangle$. The second Born amplitude is commonly calculated using several approximations. The sum has to include an infinite number of states, which can be overcome by applying the so-called 'closure approximation'. Here the energy of the intermediate state E_n is replaced by an average energy $\overline{E}$ and the sum can be evaluated due to the completeness of the target eigenstates. The value of $\overline{E}$ can be chosen arbitrarily, and a particular choice is often motivated from plausibility reasons which also depends on the process which is to be described (e.g. [MRR$^+$00]).

The second Born term breaks the symmetry of the cross section with respect to the momentum transfer, since the projectile now scatters twice. Of importance for atomic scattering experiments is the inclusion of elastic scattering of the projectile from the target nucleus. In the first order amplitude this contribution is zero. In processes involving two active electrons from the target, like double ionization or ionization-excitation of helium, the second order term can become very important in the cross section and leads to strong contributions, even at small perturbations. The calculation of the second Born amplitude is already a challenging task and so far, higher orders of the Born expansion have not been calculated.

Distorted-wave Methods

The idea behind the method of using distorted waves is to split the interaction term $V_{i,f}$ in both the initial and final state.

$$V_{i,f} = U_{i,f} + W_{i,f} \tag{2.39}$$

The interaction of the first term $U_{i,f}$ on the right-hand side of is treated exactly and the second term $W_{i,f}$ perturbatively, similar to the Born expansion. The Lippman-Schwinger equation is solved including only the so-called distortion term $U_{i,f}$, by determining the distorted scattering wavefunctions for either the initial or the final state from

$$|\chi_{i,f}^{(\pm)}\rangle = |\phi_{i,f}\rangle + \frac{1}{E - H_{i,f} \pm i\epsilon} U_{i,f} |\chi_{i,f}^{\pm}\rangle. \tag{2.40}$$

Whatever choice is made for the splitting of the initial and final state perturbation $V_{i,f}$ is left to tractability of the calculation. The transition matrix, again in the equivalent post- and prior-form, is then written as

$$T_{fi} = \langle \chi_f^{(-)} | W_f | \Psi_i^{(+)} \rangle \tag{2.41}$$

$$= \langle \Psi_f^{(-)} | W_i | \chi_i^{(+)} \rangle, \tag{2.42}$$

and so far no approximations have been made: The scattering amplitude provides the freedom to shift part of the interaction appearing in the operator V into the wavefunction. In the distorted wave Born approximation, the scattering wave is approximated for instance by

$$|\Psi_i^+\rangle \approx |\chi_i^+\rangle, \tag{2.43}$$

which would be the first order approximation. Similar to the Born series, the next higher order reads

$$|\Psi_i^+\rangle \approx |\chi_i^+\rangle + GU_i|\chi_i^+\rangle. \tag{2.44}$$

The distorted-wave approach allows to treat some part of the interaction exactly, and others perturbatively. As an example, the distorted wave methods allow to treat the interaction of the projectile with the nucleus in the initial and final channel. However, when making an approximative choice, special care has to be taken with respect to the orthogonality of the initial and final states. For instance the equivalence of the transition amplitude shown in eq. (2.41) gets lost, when approximations for the scattering wave are used.

The 3C Wavefunction

The approach using the 3C wavefunction is somehow similar to the distorted wave approach. It was first applied to electron impact ionization of Hydrogen by Brauner, Briggs and Klar [BBK89], and in an approximative way includes the interaction between three Coulomb interacting particles. The usual starting point is the transition amplitude in the prior form

$$T_{fi} = \langle \Psi_f^{(-)} | V_i | \phi_i \rangle, \tag{2.45}$$

where V_i is the interaction between the projectile and the target atom in the initial state. Instead of attempting to calculate the scattering wavefunction, the 3C approach uses an ansatz for $|\Psi_f^{(-)}\rangle$

$$|\Psi_f^{(-)}\rangle \approx |\Psi_{3C}\rangle = CW(1)CW(2)DF(1 \leftrightarrow 2). \tag{2.46}$$

The so-called 3C wavefunction serves as a description of the two electrons labeled with (1) and (2) in the field of the ion. The interaction of the electrons with the nucleus is described by the two Coulomb waves CW(1) and CW(2). The interaction between the outgoing projectile and the ejected electron is described by an additional Coulomb distortion factor DF(1↔2), which depends on the relative coordinates between the electrons. The ansatz $|\Psi_{3C}\rangle$ satisfies the correct boundary condition of the three-body Schrödinger equation and approximately describes the motion of three Coulomb interacting particles, however in an approximative manner. The 3C wavefunction only

provides an exact description for the separate two-body sub-systems, when the third particle is at infinite distance. This deficiency is partly mended by including the so-called dynamical screening (DS3C), which accounts for the presence of the third particle in the two-particle subsystems. A great advantage of the 3C approach is, that it supplies an analytical expression for the scattering wave. In some cases the model using the 3C wavefunction leads to excellent agreement with data for three-body beak-up processes, which was for instance found in single ionization at very low impact energy (1 eV above breakup threshold) [BB94]. On the other hand it was shown, that for specific scattering geometries at low energy the 3C description fails completely, which was explained by the disability to describe the three-body system at low relative particle separations [LRW99]. Any attempt to reduce the disagreement by including dynamical screening does not provide a rigid framework, since the particular choice of how the screening is included is arbitrary.

The idea of using three Coulomb waves as an approximative scattering wave for two electrons and the residual ion has been extended a description of three active electrons. Now in total six Coulomb distortions are included in the scattering wave, again treating the pairwise interaction of the four-body system. It has been used for single ionization of helium by ion impact, in order to include the electron remaining in the residual ion into the treatment [FPS$^+$05] and has been applied to double ionization, where it serves as a description going beyond the commonly used first and second Born models [GWB03, ECLBC05].

2.2.3 'Exact' Approaches to Coulomb Three-Body Problems

So far, the presented selection of theoretical models are based on approximative simplifications of the few-body Coulomb problem. With increasing computing power available in the last decades, two models have emerged, which attempt to solve the Schrödinger equation for three Coulomb interacting continuum particles in an exact manner. Naturally, the predictions are limited by the computing power, however these first numerical simulations provide a basis for further developments. In the first published calculation [RBIM99], the so-called Exterior Complex Scaling (ECS), very good agreement between the fully differential cross section for low energy electron impact ionization of hydrogen could be achieved (for a review see [MBR04]). Due to computational limitations, the framework is presently restricted to continuum problems including only three interacting particles, also realized in double-photoionization of helium. Moreover, the ECS only produces results for electron energies lower than 100 eV. A further method to describe the three-body Coulomb problem is the Convergent Close Coupling (CCC), which after a critical debate proved to provide a sound and formally correct basis for three-body descriptions [BC99, Bra99, SBP02, BS02].

Exterior Complex Scaling

The Exterior Complex Scaling treats the single ionization of Hydrogen representing the most basic and simple three-body continuum problem. The method determines the scattering wavefunction under the correct asymptotic boundary conditions, solving the time-independent Schrödinger equation.

Within this stationary treatment, the total scattering wavefunction in coordinate representation reads

$$\Psi^{+} = \phi_i + \Psi^{sc}, \tag{2.47}$$

Here ϕ_i again describes the unperturbed initial state and Ψ^{sc} is the scattered part of the total scattering wave function. For several decades, no practical solution of the three-body problem was tractable due to the asymptotic boundary conditions, and it therefore had to be treated in a approximative way. The ECS tackles the problem by transforming the spatial coordinate into the complex plane:

$$r = \begin{cases} r & \text{for} \quad r \leq R_0 \\ R_0 + (r - R_0)e^{i\eta} & \text{for} \quad r > R_0, \end{cases} \tag{2.48}$$

hence the Schrödinger equation is solved in a finite space represented by a grid. In the new coordinates the solution of the scattering wave $\Psi^{sc}(r = R_0)$ fulfills the correct boundary conditions for $r \to \infty$, which now takes the very simple form $\Psi^{sc} \to 0$. Then the limit $R_0 \to \infty$ can be taken, which leads to the exact result of the scattering wave in eq. (2.47). Practically, the extension of the grid is increased until the desired convergence is reached. The crucial point is the order, of how the limits $r \to \infty$ and $R_0 \to \infty$ are taken [MBR04].

The computed result of the scattering-wave can be visualized like in Fig. 2.9a showing one component of the expansion of Ψ^{sc} as a function of the radial coordinate of both electrons. The amplitude drops exponentially at the outer edges, which is due to the transformation of the coordinates in eq. (2.48).

Once the scattering function has been calculated, the transition amplitude has to be extracted in order to provide information on the cross section. It turns out, that considerable effort is necessary, in order to achieve an accurate evaluation of transition amplitudes [MBR04]. For example, the cross section can be calculated from the flux of the scattering wave when $r_{1,2} \to \infty$, but also other methods are possible. To do this accurately is not straightforward, since spurious effects may appear which have to be kept under control. For instance convergence of the transition amplitude with respect to the grid size has to be established. Nevertheless, the ECS provides a framework, in which the three-body continuum problem has been

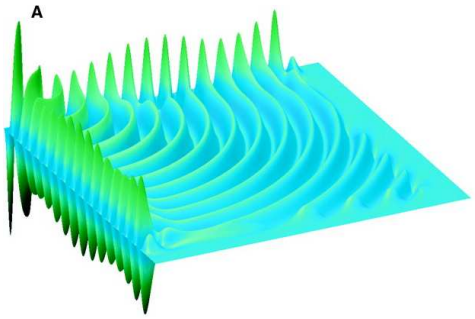

(a) Part of the expansion of the full scattering wave calculated for single ionization of hydrogen at 17.6 eV impact energy and equal energy sharing between the outgoing electrons. The wavefunction is shown in dependence of the radial coordinates r_1 and r_2 of the continuum electrons. (From [RBIM99])

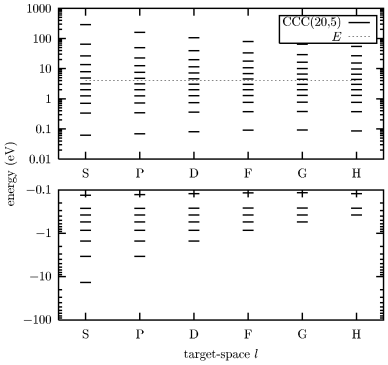

(b) The energy-spectrum of the target states displaying the bound and continuum states which form the basis of the CCC coupled channel expansions.

Figure 2.9

reduced to a matter of 'practical computation'. A drawback is, that until now it is limited to low impact energies and to three-body descriptions, because the method numerically scales infavourably with respect to needed computational resources.

First treatments of the four-body problem within the ECS realized in electron impact single ionization have been published using a simplified model, where only states with zero angular momentum are treated [HMR05a, HMR05b]. This four-body treatment studies autoionization phenomena at low impact energy which show three electron correlation effects, but is however still in its infancy.

Convergent Close Coupling

Initially, the 'Convergent Close Coupling' method was applied to study inelastic excitation processes without ejection of a target electron. The treatment of such processes using coupled channel approaches was very successful at low impact energies since only one electron is asymptotically in the continuum (i.e. the incoming and scattered projectile-electron) [BS92]. In the close-coupling treatment, which can be classified as a coupled channel calculation, the target-atom is expanded in basis-set of eigenfunctions of the unperturbed target-Hamiltonian, which is constructed from so-called Laguerre functions. The eigenstates $|\phi_n\rangle$ to the target Hamiltonian H_T are constructed such, that

$$H_T|\phi_n\rangle = E_n|\phi_n\rangle, \tag{2.49}$$

where states with negative energies represent bound and those with positive energy continuum states (see Fig. 2.9b). The only approximation done so far is that the number of target states is restricted to N, hence the name close-coupling. The bound target states represent the 'true' states, whereas the continuum states form a discretization of the continuum and are also called 'pseudo'-states. By increasing the number of states N the representation of the continuum becomes increasingly 'dense' and converges to the true continuum.

The CCC methods seeks a solution to the T-matrix, which is equivalent to solving the full Schrödinger equation.

$$T_{fi} = \langle \Phi_f | H - E | \Psi_i^{(+)} \rangle \tag{2.50}$$

Here Φ_f are the asymptotic eigenstates and $|\Psi_i^{(+)}\rangle$ is the scattering wave, which is a solution of the Schrödinger equation under correct boundary conditions. The solution is achieved by using the multichannel expansion of the scattering wave

$$|\Psi_i^{(+)}(N)\rangle = \sum_{n=1}^{N} f_n |\phi_n\rangle, \tag{2.51}$$

where the coefficients $f_n = \langle \phi_n | \Psi_i^+(N) \rangle$ are found by solving the coupled Lippmann-Schwinger equations. The asymptotic final state within the CCC-expansion is given by a $|\Phi_f\rangle = |\vec{k_f}\rangle |\phi_n\rangle$, where the scattered projectile is represented as a plane wave or alternatively by a distorted wave. The CCC framework is an 'exact' treatment of the three-body Coulomb problem in the sense, that the expression for $|\Psi_i^{(+)}(N)\rangle$ converges to the 'true' scattering wave for increasing N. Within this framework, the scattered projectile and the ejected electrons are treated in a different manner. While the former is treated as an asymptotically free particle, the latter is confined to the target-space, since it is represented by a 'pseudo'continuum state. This has caused several discussion, especially in the case, where both electrons have the same energy [BC99, Bra99]. It could be shown, that this asymmetric treatment of the two final state electrons still provides a sound basis for the calculation of scattering cross sections, even when both electrons have equal energy [Bra02], and thus the CCC framework can be seen as an exact solution to the three-body Coulomb problem. The advantage of the CCC method over ECS, is that it can easily adapted to more complex targets, where the additionally bound electrons play merely the role of spectators. Until now, the CCC method shows excellent agreement with essentially all experimental data on electron-impact single ionization of Hydrogen [Bra02, REP$^+$97] and Helium [BF96b, BF96a, SBFB05] as well as photo double-ionization of Helium [KB98] from near threshold up to high impact energies.

So far, four-body processes like electron impact ionization-excitation and double ionzation have been addressed by treating the interaction with

the projectile perturbatively by a first and second Born amplitude and describing the three-body target sub-system exactly within the close-coupling scheme. This method has shown to provide superior results in predicting fully differential cross sections at projectile energies down to $E_0 = 500\,\mathrm{eV}$ [DKS$^+$03] and also first differential data obtained for ion-impact double ionization of helium [Khe04].

2.2.4 Threshold Laws

Instead of describing the ionization process quantum mechanically, one can approach this problem classically for small impact energies, where the excess energy is small $E_{exc} = (E_0 - IP) \to 0$. After ionization near the threshold, the final-state particles have small velocities and a classical treatment can be justified. The characteristic for the so-called threshold regime is the Coulomb interaction in the final state, which dominates the behaviour of the total cross section explained by 'threshold-laws'.

The first description of the atomic threshold process in single ionization of atoms by and electron was discussed by Wannier [Wan53]. There a classical phase-space argument was used to derive the behaviour of the total cross section with increasing excess energy E_{exc}. A typical feature of the treatment is, that the knowledge of the detailed ejection mechanism is not necessary for its predictions. The result shows that the cross section for the fragmentation of atoms rises with a power law $\sigma \propto (E_0 - IP)^\alpha$, where $\alpha \approx 1$ for electron-impact single ionization of atoms. Generally, the number of free electrons in the final state and the charge of the residual ion enter into the calculation, which considers the ion screening the repulsion of outgoing electrons. For single ionization of neutral atoms, the so-called Wannier theory predicts an exponent of $\alpha = 1.13$. Since the exponent only depends on the number of final state electrons and the charge of the ion, the same behaviour is predicted for photo double-ionization of negative ions [DGH$^+$82]. The framework can be extended to multiple fragmentation and in a crude description, neglecting the electron-electron correlation, the exponent with n escaping electrons scales with $\alpha \approx (n-1)$ [Wan55]. In a more sophisticates treatment additionally considering the effects of electron correlation, a general expression for α including the charge of the residual ion Z can be derived. Apart from the behaviour of the total cross section near threshold, the framework also predicts, at which preferred angles the electron escape. For single ionization, the electrons preferably escape 'back-to-back', i.e. at angles of 180°, or in other words, the probability distribution $P_\theta(\theta_{12})$ of the two electrons has a maximum at 180°. The reason for this preferred configuration can be seen by regarding the process exactly at threshold. The two electrons can only move away from the ion in opposite directions, or otherwise one electron will be 'pushed' back into the binding potential well of the ion by the repulsive force experienced by

the other electron. A careful inspection of the behaviour of the classical phase space then additionally allows to predict the scaling behaviour of the width of the distribution $P_\theta(\theta_{12})$ which scales with $(E_0 - IP)^{1/4}$ [Rau71]. One problem of the derivation of threshold laws is, that the limits of its validity concerning the excess energy cannot be predicted from the theory. This has to be established experimentally, and the predictions of Wannier theory for two-electron escape have been to a great extent been verified for the total cross section and the angular distribution [CR74] for energies lower than 2 eV. Three-body break-up process near threshold have been studied by measuring the fully differential cross section in single ionizaton of hydrogen and helium [PS91, REP$^+$97], where the cross section varies for the two different target atoms, and photo double-ionization of helium [BS00]. On this detailed scale the classical Wannier picture quickly reaches its limits, since here the detailed dynamics of the ejection process is ignored. With the advent of 'exact' formalisms of three-body break-up processes (ECS,CCC), a full quantum mechanical treatment is provided which so far support the classically derived predictions from Wannier theory [BS04, WBS06].

Theoretically, threshold laws have been extended from the two-electron escape to three electrons, starting with the first treatment by Klar and Schlecht in 1976 [KS76, Gru83, FF90, KO98]. For double ionization of Helium by electron impact a power-law with an exponential $\alpha = 2.27$ is derived from the classical treatment. For three-electron escape the preferred configuration is with 120° between the three electrons which form a equilateral triangle with the massive ionic core at its center.

Chapter 3

Experimental Setup

In this chapter the experimental apparatus (reaction microscope) used to measure fully differential cross sections for ionization of helium by electron impact is described in detail after some general introduction into previous experimental techniques. In principle, the imaging technique exploited here, has been used since about seven years for such experiments but still suffered from technical drawbacks. In this work these have been essentially eliminated by aligning the electron beam along the spectrometer axis, providing a multi-particle imaging spectrometer that is ideally suited now for the investigation of electron collisions with atoms and molecules. Several technical problems had to be solved, as for example the realization of a position sensitive detector with a hole for the beam. The new developments, which go along with new aspects regarding resolution and calibration, open the pathway to study electron impact with slow electrons. The modifications implemented, the working principle of the spectrometer as well as the improved resolution achieved with the new setup are presented in detail.

3.1 Introduction into the Experimental Techniques

Experimentally, the most sensitive test for theoretical approaches is provided by determining the fully differential cross section of the collision process. For this purpose, with N final state particles exiting the reaction, all their momenta have to be determined. It is sufficient to detect N-1 fragments in coincidence, exploiting momentum conservation to obtain the momentum of the undetected particle. In the pioneering experiment of Ehrhardt [ESTW69], the fully differential cross section for single ionization of helium was measured by placing two electron detectors around the interaction region, where single ionization occurred after crossing a projectile beam of electrons (well collimated and with well defined energy) with an atomic beam of helium (Fig. 3.1). The scattering geometry is defined by the selective energy filtering using electrostatic analyzers, which determine the energy of the outgoing

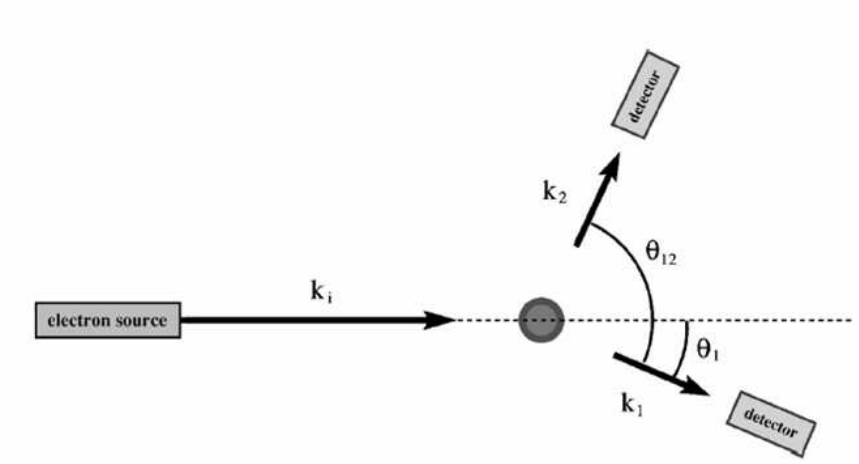

Figure 3.1: Experimental scheme for measuring the fully-differential cross section for single-ionization of atoms by electrons.

electrons, together with a well defined entrance region of the spectrometers defining the detection solid angles. The two electrons have to be detected in coincidence in order to ensure that both emerged from the same collision event. The coincidence rate R can be linked to the fully differential cross section (FDCS) by the relation

$$R = \frac{d^3\sigma}{d\Omega_1 d\Omega_2 dE_2} \cdot \Delta\Omega_1 \Delta\Omega_2 \Delta E_2 \cdot \epsilon_1 \epsilon_2 \cdot N \cdot j, \tag{3.1}$$

where $\Delta\Omega_{1,2}$ are the detection solid angles for the two electrons, ΔE_2 the energy acceptance for electron (2), $\epsilon_{1,2}$ the respective detection efficiencies and $N \cdot j$ the product of target density and beam current (see for example [LB91]). Normally, the scattered projectile is labeled with (1) and the ejected electron (2). From eq. (3.1) it becomes clear, that the small detection solid angles, which are typically in the order of 10^{-3} sr for electrostatic analyzers, lead to low coincidence rates and thus long accumulation times, when a greater part of the solid angle is to be covered.

For double ionization, where three electrons have to be detected, this leads to even lower rates, since the solid angle of the third electron additionally enters into the expression in eq. (3.1). Furthermore, the cross section for double ionization is more than two orders of magnitudes smaller than for single ionization. To overcome these limitations, 'multi-detection' spectrometers have been applied which are able to resolve angle and/or energy over a larger fraction of the solid angle and/or energy range, where to the present a solid angle acceptance of few percent of 4π is reached. This leads to typical coincidence rates of one true (e,3e) event every 20 min [DLBLM98, FDMC95].

The dependence of the FDCS on the kinematical parameter of one of the outgoing electrons is determined by measuring the coincidence rate as a function of emission angle or energy. All other factors like detection efficiencies, beam current and target density have to be controlled and stabilized while scanning. Basically, the technique was applied for many kinematical regions and in the passed 35 years a wealth of data has become available for single and more recently for double ejection of an electron from atomic and molecular targets which marks the field of (e,2e) and (e,3e) studies (reviews of these fields can be found in [EJKS86, CMD94, LB91, LB02, BLBC03]).

During the last decade a novel technique to study atomic and molecular fragmentation studies emerged: instead of detecting all final state electrons, all target fragments are detected, including the residual ion, however leaving the scattered projectile undetected. The so-called 'reaction microscope', is a combination of recoil ion momentum spectroscopy with an electron spectrometer [MUS$^+$96] and marked a big step forward in atomic fragmentation studies. The combination of electron and recoil ion momentum spectroscopy allows to gain the full kinematical information of the reaction, without detection of the scattered projectile. For the first time kinematical complete experiments on ionization by fast ions became feasible, where the projectile is scattered under indetectably small angles of 1 nrad [UMD$^+$03]. After the ionization of an atom the emitted fragments (ions and electrons) are mapped onto two position sensitive detectors using a homogeneous electric field, with an additional magnetic field to radially confine the electrons. The momentum vector (p_x, p_y, p_z) of each particle is inferred from the arrival positions and the time-of-flight (x,y,t). After coincident detection of N-1 fragments of in total N final-state particles, including the recoil ion, all kinematical parameters can be reconstructed which allows to determine the fully differential cross section. The major advantage of imaging techniques with respect to the conventional methods using electrostatic analyzers is the large phase-space acceptance, which is given by the large covered solid angle of essentially 4π for low energy electrons (up to 100 eV) and for the residual ion and also the large acceptance in the energy of the ion and the electrons. For electron impact experiments there are several advantages over conventional methods. Probably the most noticeable feature is the large range of collision geometries which can be accessed and recorded simultaneously. For instance for double ionization, this leads to an enhancement of the coincidence rate by a factor 10^9 already through the solid angle acceptance which for each detected particle is by a factor 10^3 larger as compared to conventional setups. Another advantage is the insensitivity of the measured cross section with respect to temporal variation of target density, electron beam current and detector efficiencies. The reason is that all angles and energies are covered simultaneously and the cross section at each angle is proportional to the rate integrated over the accumulation time. This is contrary to conventional methods where scanning of angles or energies has to be

undertaken, which leads to a coincidence rate, that is sensitive to temporal variation of target density and current. With a reaction microscope merely the spectrometer fields have to be kept stable, which is easily possible over several weeks of data taking.

3.2 Reaction Microscope for Electron Impact Ionization

The application of multi-coincidence imaging to study processes induced by electron impact involves a particular difficulty: the magnetic field which is used for imaging the fragments strongly deflects the projectile beam. Therefore, the situation is substantially different from studying processes induced by ions with comparably high mass or photons. One solution is reached by aligning the beam with an angle of a few degrees with respect to the magnetic field. As a result the projectile beam has a non-vanishing velocity component transverse to the magnetic field and therefore undergoes a cycling motion while traversing the spectrometer (see Fig. 3.2). Since the time of revolution of the resulting spiral trajectory depends on the strength of the magnetic field it has to be chosen such, that the projectile beam crosses the spectrometer axis in the interaction point. After a further half cylcotron revolution the projectiles pass by the electron detector in order to avoid degradation of the sensitive microchannel plate (MCP). However, for a specific projectile energy the strength of the magnetic field has to be matched. This interconnection of projectile energy and magnetic field results in a major drawback, as will be demonstrated in the following example: when using a projectile-beam with an energy of $E_0 = 2000\,\mathrm{eV}$ and in order to reach the desired projectile trajectory, a magnetic field of $B = 12$ Gauss is needed. At this magnetic field only electrons below 25 eV can be detected over the full solid angle, given by the imaging properties of the spectrometer. For lower projectile energies the magnetic field has to be decreased which in turn lowers the angular collection efficiency for the electrons. The lowest projectile energy reached with this configuration is 500 eV [DKS$^+$03].

Therefore, a different solution has been sought: aligning the projectile beam parallel to the electric and magnetic fields along the spectrometer axis, minimizes the effect of the fields on the trajectory of the incoming electrons. However, unscattered electrons from the projectile beam would impinge onto the electron detector, leading to high background and degradation of the sensitive microchannel plate. This can be avoided by implementing a hole in the detector, through which unscattered electrons pass and are subsequently dumped. In this arrangement the projectile energy and the magnetic field can be chosen independently, making very low projectile energies of a few eV accessible without suffering losses in imaging quality. However, for the implementation of the hole special care has to be taken, such that the imaging

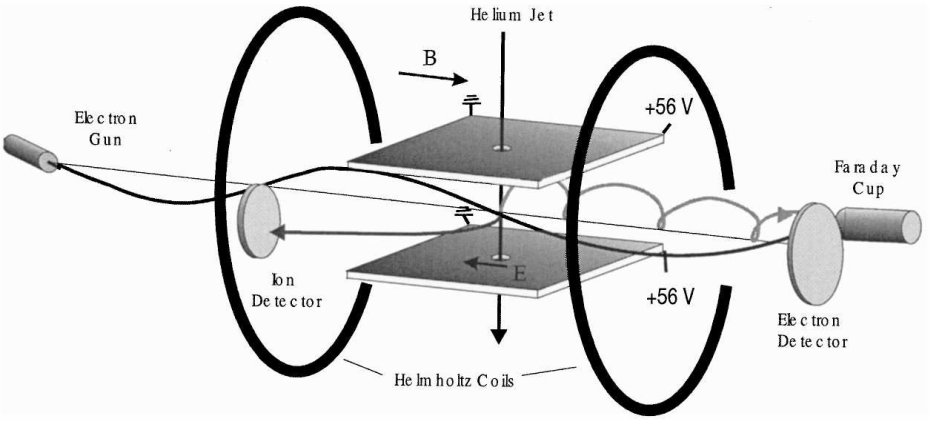

Figure 3.2: Schematical view of the reaction microscope used for previous electron impact experiments. The projectile beam has a non-vanishing velocity component transverse to the magnetic field B, which results in a spiral trajectory. (From [DKS+03])

properties of the spectrometer remain uninfluenced.

Apart from making low projectile energies feasible, the new flexibility in the choice of the magnetic field allows to chose the optimal value with respect to the imaging properties, which are discussed in more detail in sec. 3.4. Another import advantage over the previous setup, is the possibility to detect the scattered projectile deflected from the projectile axis, which is no longer guided away from the detector. Previously, the scattering angle of the scattered projectile was reconstructed from the recoil ion and the ejected electron momenta [UMD+03]. With the refinements enabling the detection of the scattered projectile the full kinematics can be directly obtained with a resolution that is a factor of two or three better. Altogether the major advantages of new arrangement can be summarized as follows:

- Increased flexibility in projectile energies and imaging properties.
- Feasibility of low projectile energies ($\ll$ 100 eV).
- Detection of the scattered projectile with full kinematical information.

These enhancements open a wide range of new perspectives which will be partly outlined in the current chapter. The reaction microscope dedicated for detailed studies of fragmentation processes induced by electron impact is displayed in Fig. 3.3. The projectile beam is crossed with an internally cold atomic beam formed out of a supersonic gas expansion. The interaction volume, defined by the overlap region of both crossed beams, is located at the center of the spectrometer where a homogeneous electric field extracts

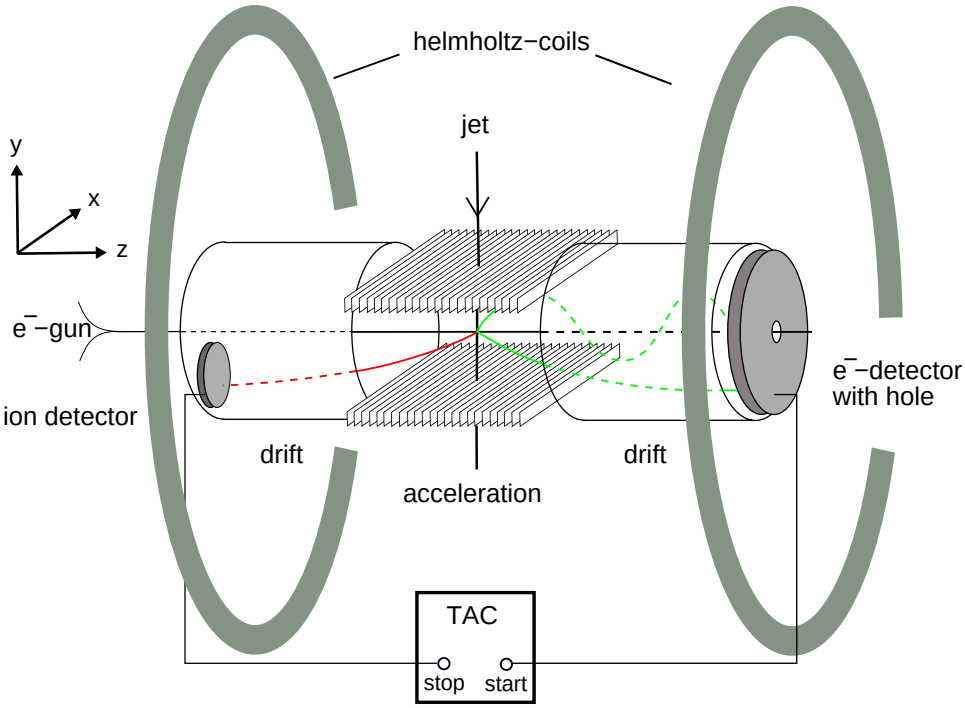

Figure 3.3: Schematical view of the reaction microscope dedicated for electron impact experiments at low projectile beam energies ($E_0 \ll 100$ eV).

ions and electrons into opposite directions. After acceleration they traverse a field-free drift region and are finally detected with position sensitive detectors located opposite of each other at the ends of the spectrometer. The interaction volume in the centre of the acceleration region together with the extraction field define the spectrometer axis which will be further referred to as the z-axis. The y-axis points in opposite direction of the jet flow, the x-axis is transverse to the jet (see Fig. 3.3). The readout circuit allows to record the coincident detection of an ion and several electrons by checking the time correlation between hits on the electron detector and the ion detector with a Time-to-Amplitude Converter (TAC)[1]. In the following all components of the setup will be described in detail.

3.2.1 Spectrometer

The spectrometer as a whole is designed to resolve all three momentum components (p_x, p_y, p_z) of electrons and ions produced after the fragmentation induced by particle impact with a solid angle of 4π. In a first step, this is achieved by guiding the charged particles onto position sensitive detectors by means of a homogeneous electric field. Ions and electrons are dragged into opposite directions due to their different charge sign. After the charged particles have been accelerated over 11 cm they pass through a field free drift region of 22 cm length, which is exactly twice the extension of the acceleration region. This leads to the so-called time-focussing configuration (Wiley-McLaren type time-focussing) in which the arrival time depends only on the initial momentum in the longitudinal direction and is in first order independent on the z-position where the fragmentation occurs. The time-focussing brings a particular advantage in the crossed beam arrangement, since the extension of the interaction volume along the spectrometer axis doesn't affect the momentum resolution in the z-direction. In consequence, there is no need of reducing the diameter of the target beam along the z-direction, for the benefit of a larger interaction volume and thus a larger number of target atoms without loss of resolution. This is always desired since ionization cross sections are typically low.

For the combined imaging of recoil ion and electron an additional homogeneous magnetic field is used, which is needed for the typical energy range of the electrons and ions emerging from the collision. Assuming that the target atom in the jet is initially at rest, the typical momentum transfered by an incoming electron is below few atomic units for most collisions of interest. The corresponding energy for a helium ion is in the range of a few meV, making an energy resolution for the residual ion in the μeV-range necessary for sufficient momentum resolution. This is achieved by using small extraction fields of a few eV/cm, reaching however at the same time a total

[1] A detailed diagram of the electronic circuit is shown in the appendix (sec. A.4)

detection solid angle of 4π for all ions. Because of the low mass of the electrons compared to the ions, the energy and thus the velocity of the electrons with a momentum of few a.u. is much higher ($p_e = 1\,\text{a.u.} \rightarrow E = 13.6\,\text{eV}$). The trajectory of the particles being limited by the spatial dimensions of the spectrometer, electrons with a transverse momentum component corresponding to a few eV in energy would remain undetected as they cannot reach the detector. Increasing the extraction voltage would diminish the momentum resolution for the ions and is thus not acceptable. Therefore, an additional homogeneous magnetic field is applied parallel to the electric field, forcing the electrons on a cyclotron motion thus leading to radial confinement of the electron trajectories and increasing the acceptance for electrons with large momenta transverse to the extraction direction. The transverse acceptance of the electrons can be calculated from the magnetic field and the geometrical dimensions of the spectrometer and is described in detail in sec. 3.4.1.

The homogeneous electric field is produced by two parallel arrays each consisting of 80 electrodes, which are located above and below the collision volume. Each electrode is electrically connected to its neighbors with a 1kΩ resistor. The voltage difference applied at the ends of each array is divided among the single electrodes, hence the array acts as a voltage divider. Simulations show that in this way two such arrays arranged parallel to each other form a homogeneous electric field [MUS$^+$96]. The region within the electrode arrays manifests the acceleration region with a total length of 22 cm. The gap between the two parallel arrays amounts 7 cm from each other, and the electrodes have a length of 20 cm. Since the ions initially have a significant momentum in the negative y-direction due to the jet-velocity ($p^y_{jet} \approx 6$ a.u. for He), the field can be slightly tilted by varying the voltage on either side of the upper or lower array. Hereby ions can be accelerated in the transverse y-direction. The whole electrode construction can be rotated around the beam axis, which allows to steer the ions in x-direction, ensuring that the ions are well guided to the detector, which is positioned 'below' the spectrometer axis. The steering of the ions doesn't affect the electrons, since the additional kinetic energy gained through acceleration in the transverse directions is typically less than a few meV.

The momentum vector of the secondary particles is determined by measuring the time the charged particles need to reach the detector and their hitting position. In the offline analysis the momentum is reconstructed by tracing back the trajectory to the interaction point. This requires a well defined electric and magnetic field throughout the entire flight path and a well defined interaction point. Any inhomogenity of the fields as well as the finite size in x and y of the interaction volume will affect the resolution. The unavoidable gap in boundary between the acceleration and the drift region leads a distortion of the field lines due to field penetration from the vacuum chamber which is at ground potential. This leads to a lensing effect which

can be cured by inserting a fine wire mesh (transmission ≈ 85 %), forming a straight equipotential surface. Unfortunately, a mesh can't be used for the ion spectrometer arm, because of the effect of 'microlensing' in the pores which affects the resolution for the low energy ions far stronger than for the electrons. The high voltages applied to the electron multiplication detection devices have to be carefully shielded as well. Especially for the electron detector, which has a hole implemented special care has to be taken, not to disturb the electric field in the drift region (see sec. 3.3).

The entire setup is located in a volume surrounded by three pairs of square-shaped Helmholtz coils (2 m wide) which shield the earth magnetic field in all three dimensions (not shown in Fig. 3.3). Hereby the distortion of the electron trajectories can be reduced. With a magnetic field probe the performance of the shielding was measured, the magnetic field not exceeding 30 mG whithout operating the Helmholtz pair used for magnetic guiding of the electrons. The latter is set to typically 6-12 Gauss, thus the resulting inhomogeneities from the imperfectly shielded earth magnetic field of $\leq$0.5% can be neglected, because they are exceeded by those of the guiding field which are estimated to be around 1%.

Reconstruction of ion momenta

The time-of-flight from the interaction zone to the detectors can be easily calculated by solving the Newtonian equation of motion. The charged particle is first accelerated by a constant electric field U/a (a: acceleration path length) and then drifts with a constant velocity (d: drift length) until it reaches the detector. The time-of-flight of a charged particle (with charge q and mass M) can be expressed as:

$$t_{\pm}(E^{\parallel}) = f \cdot \sqrt{M} \cdot \left(\frac{2a}{\sqrt{E^{\parallel} + qU} \pm \sqrt{E^{\parallel}}} + \frac{d}{\sqrt{E^{\parallel} + qU}} \right), \tag{3.2}$$

where the '+'-sign has to be used for ions/electrons emitted in direction of acceleration and the '-'-sign is used for those emitted in opposite direction. Equation (3.2) gives the time-of-flight in ns, for $f = 719.7\sqrt{\text{eV/amu}} \cdot \text{ns/cm}$ and the length of the acceleration a as well as the drift region d in cm, the Mass M in amu and qU in eV. The initial kinetic energy along the spectrometer axis gained during the collision $E^{\parallel}$ is given in eV. In order to extract the longitudinal momentum $p^{\parallel} = \sqrt{2ME^{\parallel}}$ from the measured time-of-flight, eq. (3.2) has to be solved for $p^{\parallel}$, which can only be done numerically or with an approximate function. It is convenient to express the momentum components of the electrons and ions in cylindrical coordinates ($p^{\parallel} = p_z$, $p^{\perp} = \sqrt{(p_x)^2 + (p_y)^2}$, $\phi = \arctan(p_x/p_y)$), which accounts for the cylindrical symmetry with respect to the spectrometer axis.

For ions the energy gained qU during acceleration is much larger than the initial longitudinal energy $E^{\parallel}$ and, therefore, a linear approximation of

eq. (3.2) around the point $t_0 = t_\pm(E^\parallel = 0)$ can be justified, which leads to the relation

$$p^\parallel = 8.042 * 10^{-3} \frac{\text{cm a.u.}}{\text{eVns}} \cdot \frac{q \cdot U \cdot \Delta t}{a}, \tag{3.3}$$

where $\Delta t = t_\pm(E^\parallel) - t(E^\parallel = 0)$. The actual value of $t(E^\parallel = 0)$ has to be found in a calibration procedure and is described in sec. 3.4.3 .

The transverse momentum of the recoil ion after the collision is deduced from the arrival position (x_{ion}, y_{ion}) on the detector (see Fig. 3.4). The position at which an ion with zero momentum arrives on the detector is taken as a reference point (x_0, y_0), which is determined by initial 'offset'-momentum in jet-direction and the total time-of-flight $t(E^\parallel)$. For typical acceleration voltages $t(E^\parallel)$ is in the order of a few μs, whereas Δt is in the range on a few ns and thus the arrival position can be regarded to be independent of the longitudinal momentum. With this simplification any transverse momentum of the ion leads to the displacement

$$r := \sqrt{(x_{ion} - x_0)^2 + (y_{ion} - y_0)^2} = (2a + d) \cdot \sqrt{\frac{E^\perp}{qU}} \tag{3.4}$$

The transverse momentum in a.u. is then given by:

$$p^\perp = 11.6 \frac{\text{a.u.}}{\sqrt{\text{amu eV}}} \frac{r}{2a + d} \sqrt{qU \cdot M}. \tag{3.5}$$

The reference point is uniquely defined by the centre of the spatial distribution of the events on the detector, because of the cylindrical symmetry with respect to the projectile axis. Besides the transverse momentum, also the emission angle in the xy-plane can be calculated by $\phi = \arctan(y_{ion}/x_{ion})$ (see also Fig. 3.4).

Reconstruction of electron momenta

For the electron momentum the situation is more difficult, because the magnetic field leads to a more complicated trajectory. In addition, the energy with which an electron is emitted from the collision is in the range of the energy gained during the collision and eq. (3.2) can no longer be approximated by a linear function. Instead of inverting the expression in eq. (3.2), the longitudinal momentum can be extracted using an approximative formula. First of all eq. (3.2) is transformed by setting $T = (t/a)\sqrt{qU/2m_e}$ and $x = \sqrt{E^\parallel/(q \cdot U)}$, m_e being the mass of the electron, and now reads:

$$T = \frac{1}{\sqrt{1 + x^2} + x} + \frac{1}{\sqrt{1 + x^2}}. \tag{3.6}$$

The inverse function can be approximated by the expression

$$x = A + \frac{B}{T} + C \cdot T + D \cdot \sin(T), \tag{3.7}$$

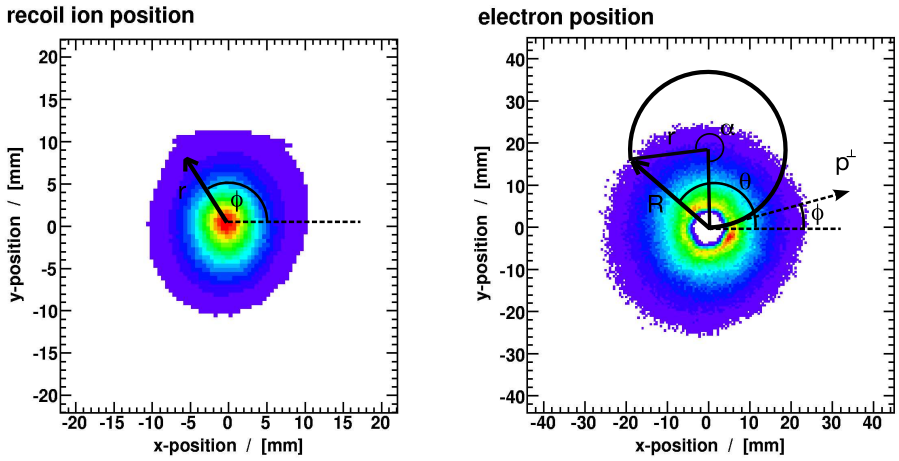

Figure 3.4: Illustration of the reconstruction of the transverse components of the ion and electron momenta from their arrival positions on the detector (see text). On the right the hole of the electron detector can be seen in the center of the distribution.

with the constant factors $A = -0.051, B = 1.508, C = -0.466, D = 0.2558$. The longitudinal momentum then is calculated simply by

$$p^{\parallel} = x \cdot \sqrt{2m_e eU} \tag{3.8}$$

Another difficulty arises from spiral trajectory of the electrons in the magnetic guiding field with the cyclotron frequency

$$\omega = \frac{qB}{m_e} \tag{3.9}$$

which only depends on the magnetic field B. As will be shown later this relation can be used for its precise determination in the offline analysis. First it should be noted, that the radius r of the cyclotron motion depends on the transverse momentum by

$$r = p^{\perp}/eB. \tag{3.10}$$

From the interaction point to the final arrival position (x_e,y_e) the electron has passed through $\omega \cdot t/(2\pi)$ turns in the magnetic field (t=time-of-flight). The trajectory of the electron additionally depends on the initial azimuthal angle ϕ. The resulting path from the interaction point to the detector as seen in the projection on the xy-plane (the 'detector'-plane) is shown in Fig. 3.4 and illustrates the reconstruction of the transverse momentum $p_{\perp}$ from the hitting position on the detector. The centre of the xy-coordinate system is defined by the origin of the electron trajectories which lies on the

spectrometer axis. The distance of the hitting position from the detector-center R can be related to the radius r of the cyclotron motion by

$$r = \frac{R}{2|\sin(\omega t/2)|}, \tag{3.11}$$

and allows to calculate the magnitude of the transverse momentum with eq.(3.10).

$$p^{\perp} = 1/2 \cdot \frac{ReB}{|\sin(\omega t/2)|} \tag{3.12}$$

The azimuthal angle during the emission ϕ is related to angle ϑ in the detector plane by

$$\phi = \vartheta - \omega t/2 \tag{3.13}$$

derived from simple geometrical considerations [2]. The presented relations eq. (3.13), (3.12) and (3.8) can be used to estimate the effects of the time- and spatial-resolution on the reconstruction of the electron momentum which will be discussed in sec. (3.4.2).

3.2.2 Projectile Beam

The projectile electron beam is produced from a standard thermocathode electron gun (see Fig. 3.5). It consists of a tipped cathode from which electrons are emitted by thermionic emission. The cathode is enclosed by the Wehnelt cylinder, which is negatively biased with respect to the cathode. Focussing is achieved by three einzel-lenses succeeded by two pairs of parallel plates which can be used to steer the beam in x- and y-direction. The main purpose of the Wehnehlt cylinder - besides focussing - is to pulse the electron beam. The negative potential from the Wehnelt cylinder forms a potential barrier for the electrons emitted by the cathode, which is turned off by applying a short positive voltage pulse ($U_{max} = 20\,V$, length ≈5 ns (FWHM)) on the Wehnelt cylinder, accelerating the electrons from the cathode and a short bunch of electrons is emitted. A typical value for the length of an electron bunch is approximately between 1 ns and 1.5 ns with a beam focus $< 1\,mm$ measured at the interaction zone. The number of electrons in each bunch is approximately 10^4 which correspond to a beam current of 300 pA at a repetition rate of 200 kHz. Electron energies ranging from 30 eV to 2 keV could be realized.

During the whole passage of the projectile electrons, the beam should stay focused temporarily and spatially which is a particular challenge in view of the rather large distance (66 cm) the beam has to pass through the spectrometer without focussing elements. The transverse velocity distribution leads to defocussing whereas the longitudinal energy spread to dispersion

[2] This depends on, whether the magnetic field is parallel or anti-parallel to the electric field. Otherwise the expression is $\phi = \vartheta + \omega t/2$

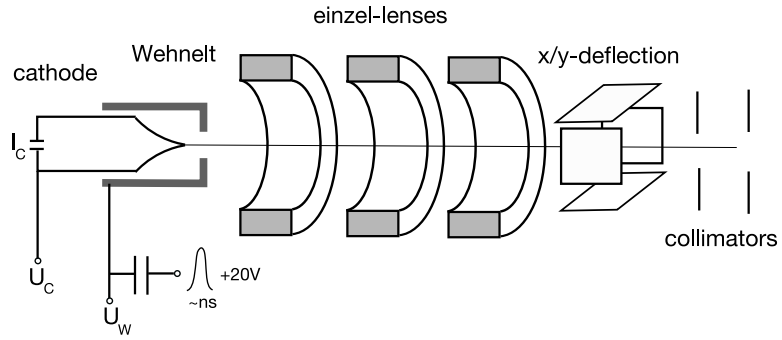

Figure 3.5: Schematical view of the electron gun and its components.

of the pulse. Additionally, space charge effects lead to spatial and temporal broadening which becomes increasingly important for low energy beams where the projectiles are slow. At the end the electrons have to traverse through the hole in the detector without creating too many secondary electrons, which may lead to high background. The magnetic imaging field can assist in guiding the primary beam on its way through the spectrometer, since it radially confines the motion of projectile electrons. At specific values, when the time for a full cyclotron revolution equals an integer multiple of the time-of-flight from the source to the interaction region, all electrons independently of their transverse velocity return to their source point. This can be used to improve the focussing in the target region, however only at cost of flexibility in the choice of the magnetic field.

The pulse length determines the achievable resolution for the reconstruction of the electron momenta. In future shorter pulse widths can only be reached with more sophisticated electron sources such as photo-cathodes, of which GaAs semi-conductor cathodes have been pursued because of the potential of creating (ultra-)cold and even spin-polarized beams [SRD+05].

3.2.3 Target

For ion momentum spectroscopy in ionizing collisions the residual ion receives a momentum of less than a few atomic units, which is much lower than the initial momentum spread of a gas at 300 K. Hence, the target atoms have to be cooled far below room temperature, in order to resolve the momentum transfered during the collision. An atomic beam formed out of a supersonic jet expansion, fulfills the requirement of internal cooling and at the same time comparably high densities can be reached (Fig. 3.6).

In the present setup the beam nozzle has $30\,\mu m$ diameter and can be operated at stagnation pressures up to 17 bar. The internal cooling of the beam depends on the ratio p/p_0 of stagnation pressure in the nozzle p_0 and the final pressure after the expansion p, which is estimated to be the vacuum

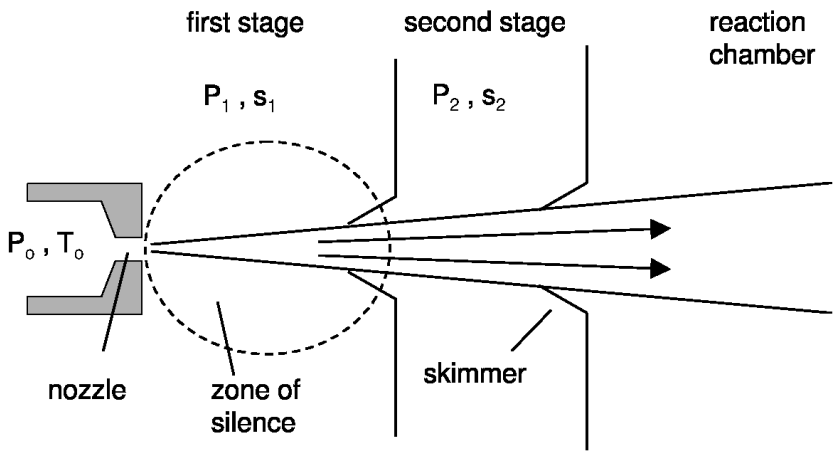

Figure 3.6: Schematical view of the two stage supersonic jet (from [US03]).

pressure in the last expansion stage. The reachable pressure p is limited by the pumping speed of the pumps in the expansion stages. The final internal beam temperature T can be expressed by ([Mil88])

$$T = T_0 \cdot (\frac{p}{p_0})^{(\gamma-1)/\gamma}, \tag{3.14}$$

where T_0 is the initial gas temperature, and γ the adiabatic coeffecient. For helium the lowest temperature reached is 1 K in beam direction (without pre-cooling of the gas) for a stagnation pressure of $p_0 = 17$ bar before the nozzle and a base pressure of $p = 10^{-6}$ mbar in the second stage. A second advantage of supersonic expansions is the high particle density in the beam ($\approx 10^13$ atoms/cm^3), which is important for the overall interaction rate (eq. (3.1)). Transverse to the beam direction the internal temperature can be further lowered by collimating the beam with a slit, filtering out hot atoms which have a large transverse velocity component. After the skimmer the beam traverses a slit for collimation of 1 mm diameter before entering the acceleration region through the electrode plates in the centre of the array. The beam exits through the lower array and enters a differentially pumped jet dump. At a base pressure of a few 10^{-9} mbar in the spectrometer region no pressure rise could be observed during operation of the supersonic jet. The beam diameter of the jet at the interaction point is estimated to be about 1 mm (FWHM). The extension of the target along the spectrometer axis doesn't play a major role. Because of the time-focussing geometry the resulting size of the interaction volume in z-direction doesn't affect the resolution. That is one advantage of aligning the projectile beam along the

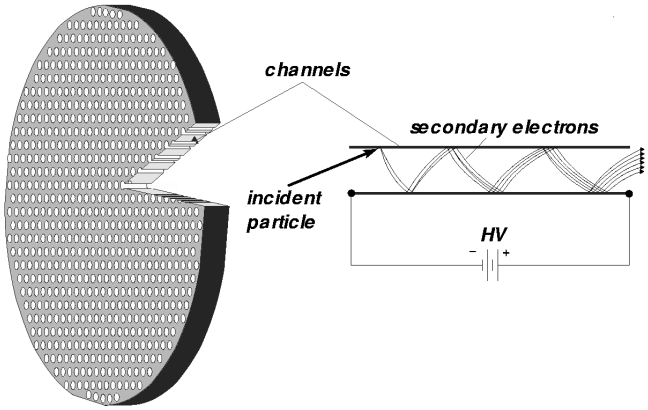

Figure 3.7: Details of a microchannel plate used as an electron multiplication device. (From [MFK03])

spectrometer axis, since in the direction of the projectiles no focussing is possible.

A further benefit of supersonic expansions is the possibility to produce clusters during the expansion. Here noble-gas clusters open interesting perspectives as the bonding between the individual atoms due to the van-der-Waals Force differs from molecular bonds. Furthermore, molecules are cooled into their vibrational ground state during the jet expansion thus providing well defined initial conditions.

3.2.4 Position Sensitive Detectors

The detection of charged particles is accomplished by a microchannel plate (MCP), used for electron multiplication, and a position encoding structure which delivers the arrival position. A microchannel plate is a microfabricated array of channels (each with a diameter of a few tens of microns) with a total diameter several cm. The initial incoming particle enters a channel and produces a charge cloud at the exit of the channel by secondary electron multiplication. By stacking several channelplates, typical amplification factors range between 10^4 and 10^6 and the charge amount leads to a sufficiently high voltage signal which can be processed electronically. In order to resolve the position, the produced charge cloud is accelerated on a position encoding device (anode), which allows to determine the position where the charge arrived on the MCP.

For position encoding the ion detector is equipped with a standard wedge & strip anode, which allows good position resolution without need of sophisticated electronics [MJL$^+$81]. For the electron detection a three-layer delay-line anode (Hexanode) [Jea02] with increased multi-hit capabilities is used to resolve the position. Deadtime-free detection of two electrons arriving

within a short time is of major importance for studying double ionization processes, where two electrons have to be detected. Additionally, the information on the momentum of the recoiling ion is no longer necessary when all final-state electrons in (e,2e) processes are detected. This significantly increases the resolution and allows to extend the range of heavier target species, where the internal cooling does not lead to sufficient momentum resolution. Alternatively, the ion detection can be used to get information on molecular break up processes, which is not available when only electrons are detected. Because of the great importance of deadtime-free detection and the connected experimental perspectives of studying electron-molecule interactions and because it states one of the major improvements with respect to the previous microscope, the electron detection scheme is presented in more detail.

3.3 The Electron detector

3.3.1 The Hole of the Electron Detector

The electron detector has to be equipped with a hole (10 mm diameter) in order to allow unscattered projectiles to pass (Fig. 3.8). The main challenge is to avoid the penetration of fields which are produced by the high voltages of several kV needed for the efficient electron multiplication in the MCP. For electrons moving in the drift tube towards the detector, the front-side of the MCP and its high voltage of ≈ 200 V is shielded by a grid, which is set to the drift tube potential. A ceramic tube through which the projectile beam is guided, is coated with a resistive layer of germanium on its outer side and is placed between the grid and the front-side of the MCP. The outer side of the tube is electrically connected on both ends, one end with the front-side of the MCP, the other with the grid. The germanium layer acts as a continuous voltage divider which leads to straight potential lines between the grid and the front side of the MCP. Between the back side of the MCP and the delay-line the field has to be homogeneous as well, such that the charge cloud exiting a MCP channel is properly imaged onto the delay-line. For this purpose a metal ring is inserted into the hole of the channelplate and has electric contact to its back-side in order to reduce the stray fields from the hole. The projectiles are guided to pass through the ceramic tube where they are attracted by the positive potential of the delay-line anode, which acts as the 'beam dump'. The projectiles do not represent any hazard, since the number of electrons in each bunch is less than the number of electrons in a charge cloud produced by the MCP. No influence of stray fields penetrating into the spectrometer region or in any crucial point could be observed within the limitations of the resolution.

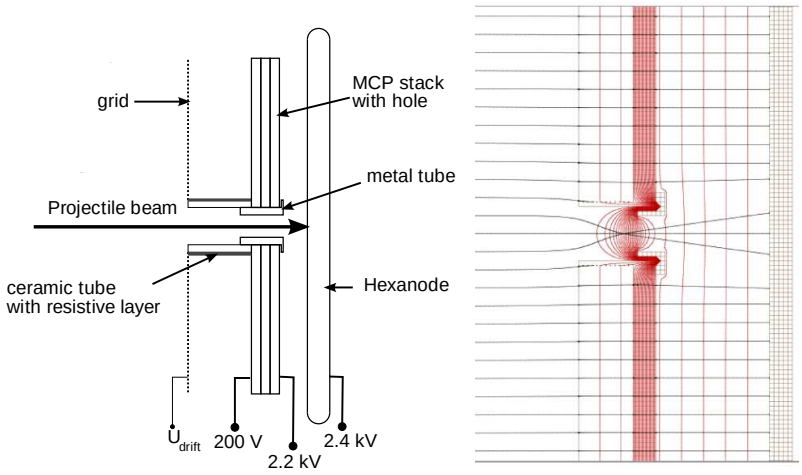

Figure 3.8: Left: Details of the electron detector with implemented hole. The delay-line is used as 'beam dump' for the primary beam. Right: The same view in a SimIon simulation of the static electric fields and trajectories of electrons from the spectrometer impinging on the detector system from the drift region. The red lines are equipotential-lines resulting from applying typical voltages

3.3.2 The Delay-Line

As mentioned earlier, the position on the detector is determined in different ways for the ion and for the electrons, since for the electrons the detector needs multi-hit capability which is unnecessary for the ion detection[3]. The so-called delay-line Hexanode allows to detect several hits arriving in short time with practically no deadtime. In the following this system used for electron detection will be described in more detail.

Before going into the details of deadtime-free detection with the Hexanode, the general working principle of the delay-line is presented. The signal processing and the electronic deadtime strongly determine the multi-hit abilities of the setup, which will be introduced afterwards and is accompanied by some words about the effects of signal losses on the position encoding and the necessary reconstruction strategies.

The electron impinges on the MCP leading to an electron avalanche which is imaged on a positively biased delay-line anode. The delay-line anode consists of two wire layers, on which the charge cloud is deposited. The signal propagates to both ends of each wire and the time difference is proportional to the position coordinate at which the charge cloud started to travel to the wire ends. The scheme for one layer is visualized in Fig. 3.9a. The signal of the MCP gives the arrival time t_0 of the electrons on the

[3] at least for atomic targets

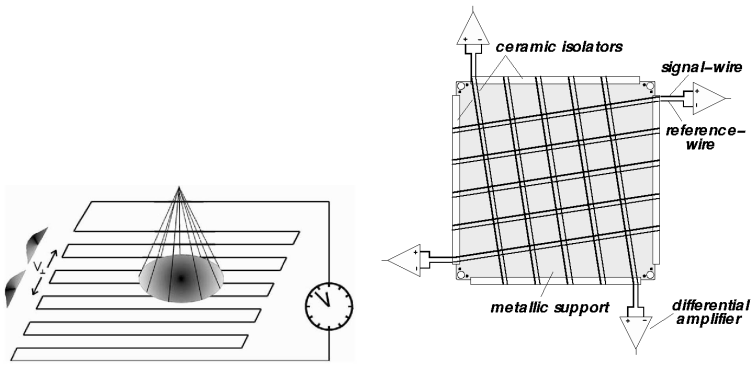

(a) (b)

Figure 3.9: Left: Scheme of principle of a delay-line used for position sensitive detection. Right : Details of a square delay line with the two layers of wire pairs wound around the support structure.

detector and starts the clock which measures the arrival time of the signals on each layer. Assuming that the signals propagate along each coordinate with an effective velocity $v_\perp$ and the propagation time of the signal-pulse to each end of the delay-line is t_{left} and t_{right}, respectively, the position coordinate in one layer can be calculated as:

$$x = v_\perp \cdot ((t_{left} - t_0) - (t_{right} - t_0)) = v_\perp \cdot (t_{left} - t_{right}) \tag{3.15}$$

The second layer, wound perpendicular to the first one, provides the second coordinate y. The largest time for the signal propagation is typically 70 ns for a square anode with 80 mm width. The achievable resolution depends on the timing resolution, which is about 1 ns with the present setup which would correspond to a resolution of about 0.5 mm.

As can be seen from eq. (3.15), the arrival time on the detector t_0 cancels out and is not needed for the position information. The time-sum of each individual layer

$$t_{sum} = (t_{left} - t_0) + (t_{right} - t_0) = const. \tag{3.16}$$

is constant and depends on the cable length and the size of the anode. In the usual analysis only events fulfilling the condition (eq. (3.16)) are processed, which allows to filter 'good' events from noise.

Electronic Processing of the Signals

The electron multiplication avalanche in the MCP leads to a detectable drop in the applied voltage, which has a duration of 10 ns (width of the baseline) and delivers the arrival time t_0 on the detector. The resulting signal pulse is

amplified and further processed with so-called Constant Fraction Discriminators (CFD) before it is transmitted to the Time-to-Digital Converter (TDC), which digitizes the time information.

The processing of the delay-line signals requires a little more effort: each layer actually consists of two wires, where one is positively biased with respect to the other (Fig. 3.9b). Thus the electron cloud will mainly impinge on this wire, which is the 'signal-wire'. The second wire, the 'reference-wire', runs parallel to the signal wire at a spacing of 0.5 mm forming a transmission-line. In addition, any noise picked up by both wires can be eliminated by amplifying the voltage difference between the signal and reference wire with a high-bandwidth differential amplifier (DA). The amplified difference signal is fed into to the CFD and then to the TDC.

The CFD is an electronic device which produces a standarized output signal (NIM) if the input voltage exceeds an adjustable threshold. The output occurs, when the input has risen to 20% of its maximal value and is fed to a TDC where the information is digitized and recorded. With a CFD the timing of the output pulse is independent of pulse height and thus reduces the jitter of the pulse which is essential for good timing resolution. The CFD plays the decisive role in determining the timing of the arriving pulse and it severely affects the capability of processing two pulses arriving within a short time. When two pulses overlap, either only the first pulse is processed properly or the interference may inhibit any output at all. The NIM-signals are then transmitted to a multi-hit TDC, where the arrival time is digitized. The signals taken directly from the MCP have a different shape and are shorter than the pulses from the delay-line. This can be probably attributed to the limited bandwidth of the difference amplifier and the dispersion of the pulses during their propagation along the delay-line wires, which leads to broadening of the input pulse. Typically the width of the baseline of the voltage pulses is 10 ns for MCP-signals and 15-20 ns for delay-line signals. Therefore, the interference of two delay-line pulse arriving within short time during the processing in the CFD becomes stronger resulting in a longer deadtime than for signals from the MCP, which are directly amplified with a high bandwidth amplifier (FA).

The timing resolution is estimated ≤ 1 ns given by the electronic signal procession devices.

The Electronic Deadtime

With the electronic processing presented in the previous section, the question is now, how the limitations of the CFD in processing multi-hits and the inherent deadtime of 10 ns of the TDC finally affects the multi-hit capabilities. In order to get this information, the problem of interfering signals can be studied in the following way: the capability of the readout-circuit to process two signals on each separate channel depends on the time-difference

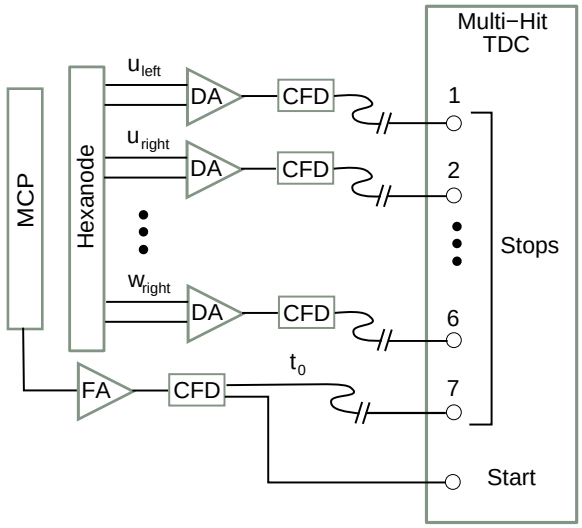

Figure 3.10: Selected electronic components for the signal-processing of the Hexanode (see text).

between two pulses, or 'pulse-pairs', which shall be now defined as t_{pp}. For the channel processing the MCP signal (No. 7 in Fig. 3.10), t_{pp} is just equal to the time-of-flight difference Δt of the incoming hits. This is different for the channels processing delay-line signals (No. 1,... 6, in Fig. 3.10), where the pulses first propagate with times t_{left} and t_{right} before they reach the processing units. The deadtime for both kinds of signals, either from the MCP or from the delay-line, can be studied by looking the number of signals recorded by the TDC as a function of t_{pp}. Such a 'pulse-pair'-spectrum is shown for both 'types' of signals in Fig. 3.11: for a signal arriving from the MCP and for a signal from one end of a delay-line layer.

The limited deadtime leads to loss of at least one signal at a specific range of t_{pp}:

- The pulse-pair spectrum of the MCP signal has a steep cutoff at $t_{pp} =$ 10 ns, which is due to the deadtime of the TDC. Between 10 ns and 20 ns some oscillations appear, which may be due to interference of two signals, while they are processed in the CFD. In particular the dip at $t_{pp} \approx$24 ns may be attributed to an inhibited output of the CFD.

- For the case of delay-line signals such a sharp cutoff is absent, and thus is not attributed to the deadtime of the TDC. The reason may be the variety in the length of the arriving delay-line pulses, some being shorter or longer. Pulses with a larger width lead to a greater deadtime than shorter ones, such that the pulse-pair distribution is smeared out. A dip is also apparent at around 30 ns, which may be for the same reason as for the MCP signals, namely the interference of

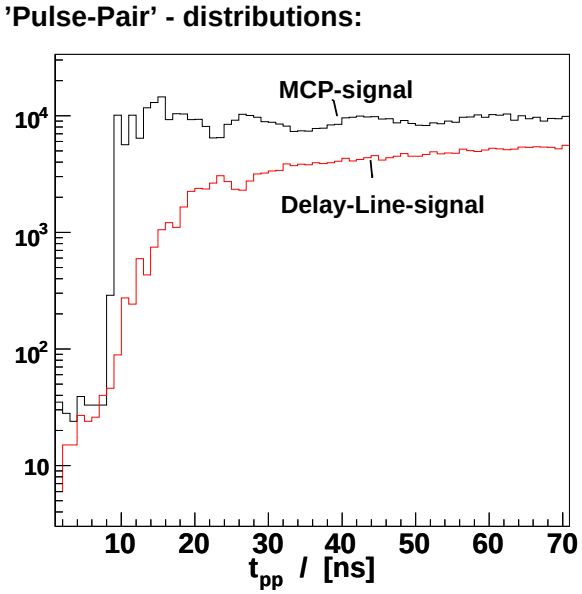

Figure 3.11: Number of recorded double-hits as a function of the time difference t_{pp} between two signal pulses, displayed for the MCP-signals and signals from one delay-line layer end. The so-called 'pulse-pair'-spectrum shows the deadtime of the electronic circuit.

input signals in the CFD. It appears at larger t_{pp}, which is probably due to the larger width of the signals.

3.3.3 Hexanode Delay-Line Detector

Now that the deadtime for the different types of signals has been demonstrated, the question is how the interplay of lost time and delay-line signals affects the position encoding of multiple hits. Fig. 3.12 shows the number of recorded events depending on their difference of their time-of-flight Δt and their difference in coordinate of one layer, denoted Δu in Fig. 3.12 and expressed in ns. Only position signals are plotted, where the time-sum condition for each of the two hits was fulfilled. Two deadtime regions become visible, in which the information has to be reconstructed. The narrow blank area in Fig. 3.12 (left), marked as region I, can be easily explained by lost time-signal of the MCP: when the second hit arrives the detector within 10 ns after the first hit, the information cannot be processed by the TDC, as it falls within its deadtime.

The question arises, how the shape of region II can be explained and why it is that large, the width of the corridor without events being ≈60 ns. First, there is a relation between the coordinate difference Δu and Δt, for which the deadtime for delay-line signals becomes relevant. Delay-line signals from

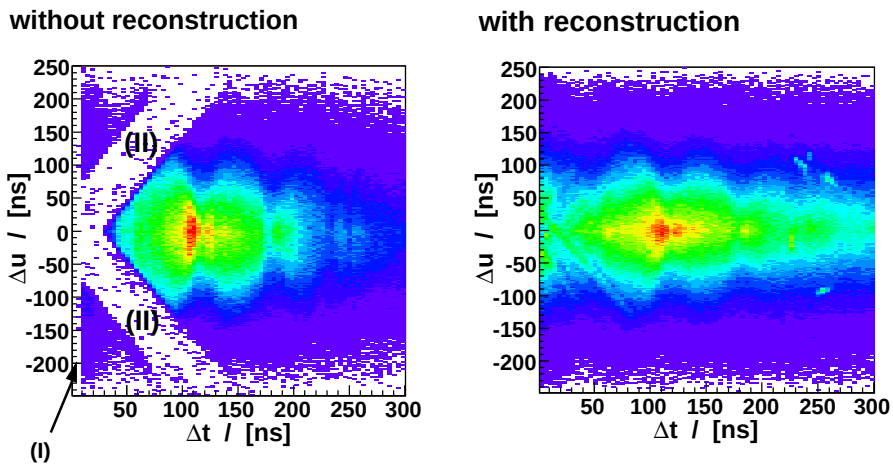

Figure 3.12: Demonstration of the impact of the deadtime from the electronics (left) and the perfomance of the RESORT 6.0 signal reconstruction routine by A. Czasch (right).

electrons only interfere when they overlap while they are processed by the electronics (i.e. at small t_{pp}). When the first hit occurs on the detector, the pulse deposited on a specific delay-line layer (e.g. u-layer) propagates to each end. During the propagation a second hit occurs, leading to another pulse pair traveling to each end. At a particular end of the wire, the deadtime only becomes important if the pulses generated by the two hits reach the end of the layer at the same time. If Δt is larger, the delay-line signals only interfere at larger separations in the coordinate Δu due to the propagation time on the delay-line, which explains the shape of region II.

The large width of approximately 60 ns finds following explanation: In the empty area (II) on the left of Fig. 3.12, the delay-line signal on one end of the u-Layer became lost due to the deadtime of the electronics. Because the information of either hit may have been lost, the width of region II is about twice the dead time for delay-line signals of about 30 ns.

Signal Reconstruction

In principle the problem of lost time signals can be overcome by reconstructing the arrival time from the position signals and the constant time-sum from the delay-line using eq. (3.16)

$$t_0 = 1/2(t_{left} + t_{right} - t_{sum}). \tag{3.17}$$

The equation holds for both layers, which allows a cross check when all position signals are present. However there still remains the problem of lost delay-line signals, when two particles arrive on the detector with a

certain time and position difference. When the arrival time is known, and the delay-line signal is lost on one end, the information provided by the delay-line is still sufficient, because the time sum of the respective layer is constant. Hence the missing position signal on the left (right) end can be reconstructed from the position signal on the right (left) end by

$$t_{left(right)} = t_{sum} - t_{right(left)} + 2t_0. \tag{3.18}$$

The problem arises, when the arrival time *and* a position signal is lost, because neither position nor arrival time can be inferred. This situation occurs in the intersection of region (I) and region (II). This decisively influences the ability to detect multiple hits, which depends on the difference in arrival position $(\Delta x, \Delta y)$ and arrival time Δt. For a square anode with two layers, one for the x- and the second for the y-position, blanks are apparent for both the x- and y- coordinate (similar to the blank areas in the spectrum Δu vs. Δt). For a double-hit of particles, the information of the second hit is irrecoverable at time differences $\Delta t \leq 10\,\text{ns}$ and for a position relative to the first hit $(\Delta x, \Delta y)$ which lies on a cross, as visible in Fig. 3.14.

In order to overcome this limitation, a third layer can be added, which supplies a third redundant coordinate. In this type of delay-line anode, the so-called Hexanode (Fig. 3.13), the three layers have a relative angle of 60° with respect to each other forming a hexagonal structure. From the three coordinates of the layers u,v and w the position in the rectangular coordinates x,y can be calculated with following relations:

$$\begin{aligned} x_{uv} &= u \\ y_{uv} &= \frac{1}{\sqrt{3}} \cdot (u - 2v) \end{aligned}$$

$$\begin{aligned} x_{uw} &= u \\ y_{uw} &= -\frac{1}{\sqrt{3}} \cdot (u + 2w) \end{aligned}$$

$$\begin{aligned} x_{uv} &= (v - w) \\ y_{uv} &= -\frac{1}{\sqrt{3}} \cdot (v + w). \end{aligned}$$

The x- and u-axis are chosen to be the same for reasons of convenience.

The redundant information allows to unambiguously assign the detected signals to two individual hits arriving within a short time Δt on the MCP. For $\Delta t < 10$ ns the deadtime cross of a two layer anode is reduced to a hole for the Hexanode (Fig. 3.14).

In practice, the reconstruction of the position and time informations is complicated by timing problems of the CFD for specific pulse-pair separations t_{pp} and noise. Special care has to be taken, that the recorded digitized

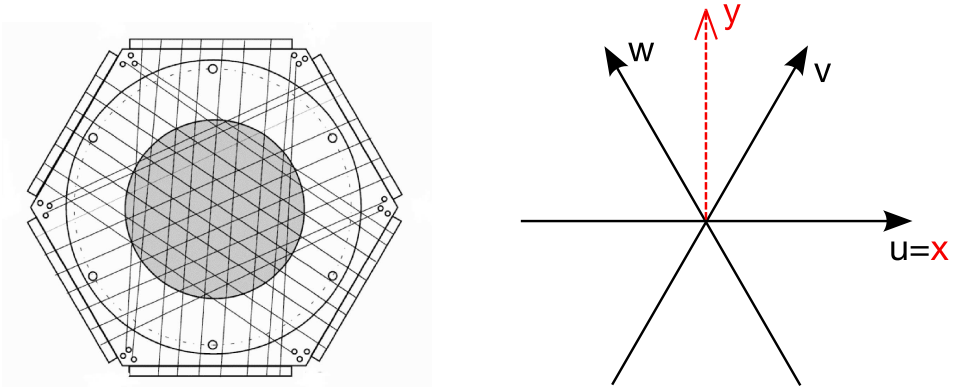

(a) The Hexanode, a delay-line anode with three coordinate-layers for increased multi-hit capabilities.

(b) Details on the coordinates u,v,w of the Hexanode and the spatial cartesian coordinates x,y.

Figure 3.13: Some details on the delay-line anode used for position encoding of the electrons

information from the delay-line is properly assigned to the individual detector hits. In particular, spurious contributions have to be avoided from signals, which are mistakenly reconstructed from noise. This makes an elaborate reconstruction routine necessary. According to the spectrum in the left of Fig. 3.12 position signals in one coordinate are lost even for large differences in the time-of-flight of the electrons $\Delta t \leq 150\,\text{ns}$. In these cases, position signals have to be reconstructed, otherwise acceptance holes will appear for very specific cases of double hits. This effect can be shown for electrons arriving with a difference of $\Delta t = 80\,\text{ns}$, and therefore the reliability of the sorting algorithm is of great importance even for two-electron hits which arrive within larger times Δt. The performance of signal reconstruction is shown on the right hand side of Fig. 3.12, where the blank areas could be filled by an elaborate reconstruction routine (RESORT 6.0) developed by the A. Czasch from the group of R. Dörner in Frankfurt.

In conclusion, the reconstruction of the pulses is of decisive importance for the detection of several electrons and therefore for the realization of the advanced capabilities of detecting the scattered projectile in electron impact ionization experiments. A successful data-reconstruction critically depends on the quality of the signals received from the detector-system. Otherwise the data will be 'contaminated' by falsely reconstructed events. In future, modern electronic data processing devices (Flash-ADC) will make it possible to digitize the amplified analog pulse coming from the detector and to store the entire information of the pulse shape. The further processing, previously done electronically by the CFD is done 'offline' by software with far more sophisticated methods available, hereby reaching higher timing resolutions of 0.5 ns and essentially zero deadtime (see e.g. [CVB$^+$05]).

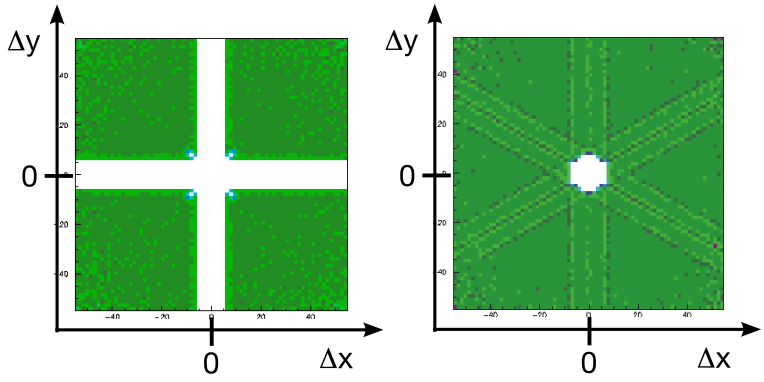

Figure 3.14: deadtime region resulting for the second hit arriving within 10 ns after the first hit for a 'conventional' delay-line anode using two layers (left) and for two hits arriving simultaneously for a Hexanode using three layers (right) (from [Gmb].)

3.4 Performance: Acceptance and Resolution

With respect to the previous reaction microscope for electron impact ionization studies, new features have to be considered and will be discussed in the following section. First, the hole in the detector has an impact on the acceptance: not all electrons can be mapped on the detector surface, which has implications to the solid angle acceptance. Second, all particles in the final state including the scattered projectile can be detected and momentum and energy conservation can be checked. This has the big advantage that the spectrometer can be precisely calibrated. Moreover the resolution for electrons and ions can be determined and reliable limits on the measured cross section can be given.

3.4.1 Acceptance

The major constriction for the acceptance in momentum space is given by the size of the position sensitive detectors. For the ion momenta the acceptance in the longitudinal direction is limited to $p^{\parallel} \leq \sqrt{2MeU}$ by the acceleration voltage U used to guide the ions onto the ion detector. With the high mass of the ion compared to an electron this usually doesn't lead to any restrictions for the collisions of interest. This is no longer true for the transverse acceptance of the ions, which can be calculated straightforwardly from eq. (3.5) assuming a maximal displacement of an ion of 20 mm which just half the diameter of the detector. For example, at a spectrometer voltage of 18.5 V and the spectrometer extensions given in sec. 3.2.1 the maximal accepted transverse momentum of a He^+-ion is 4.5 a.u.

The acceptance of electrons in terms of momentum components $p^{\parallel}$ and $p^{\perp}$ is given by the spectrometer voltage U, the magnetic field strength B and

the geometrical extensions of the spectrometer. For the longitudinal component of the electrons the same argument as for the ions is valid. Electrons which are emitted opposite to the extraction field can escape the acceleration region, if they have a kinetic energy larger than electric potential U. Thus only electrons with a momentum larger than $p^{\parallel} > -\sqrt{eU/2m}$ can be guided to the electron detector by the accelerating electric field. In the positive z-direction there is no limitation in momentum acceptance, meaning that very fast electrons can be detected. Even though the resolution of the longitudinal momentum is poor for fast electrons, the transverse momentum of the fast detected projectile may still be resolved.

For the transverse component $p^{\perp}$ the acceptance is determined by the limits imposed on the trajectories of the electrons reaching the detector. The radial motion of the electrons is limited by the separation of the two electrode arrays in the acceleration region to a radius of $d/2 = 35\,\mathrm{mm}$. Due to the hole in the electron detector only electrons cycling with a radius larger than 5 mm can be detected. In consequence there is a minimal (maximal) cutoff in transverse momentum $p^{\perp}$ at the value

$$p^{\perp} = 4 \cdot 10^{-3} \frac{\text{a.u.}}{\text{mm Gauss}} \cdot Brq \tag{3.19}$$

which can only be reduced (increased) by lowering (raising) the magnetic field. The cyclotron motion has additional consequences for the acceptance: at flight-times t which are integer multiples of the cyclotron-revolution time $t = t_{wig} = n \cdot 2\pi/\omega (n = 0, 1, 2, \dots)$ all electrons originating from the interaction point return to the spectrometer axis (magnetic focussing). These characteristic times t_{wig} only depend on the magnetic field and are called a 'wiggle'. They can be seen in Fig. 3.15 (left) showing the radii of the recorded electrons as a function of the flight time. At times near t_{wig} the radii shrink to small values for all electrons which become undetected because they enter the detector hole. With eq. (3.8) and (3.12) the radius of an electron and its time-of-flight can be translated to transverse and longitudinal momentum leading to the corresponding shape of accepted momenta as displayed in Fig. 3.15 (right).

The visible blanks in momentum space can be filled by repeating the measurement with different electric or magnetic field, or by changing both. By varying only the acceleration voltage , where t_{wig} remains fixed, electrons that previously entered the hole, now arrive earlier or later and therefore can be detected. An important issue is the acceptance of the two detected electrons that will be discussed in the following section.

Combination of Several Measurement Runs

The hole of the detector brings in a further difficulty. Due to the specific trajectory of the electrons in the magnetic field, blank areas appear in

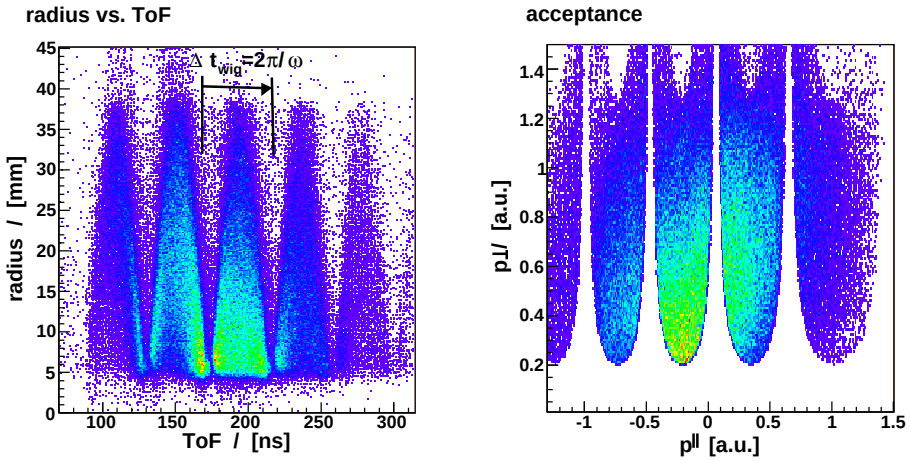

Figure 3.15: Left: The detected radial range of electron trajectories as a function of the time-of-flight. Right : The resulting acceptance in momentum space.

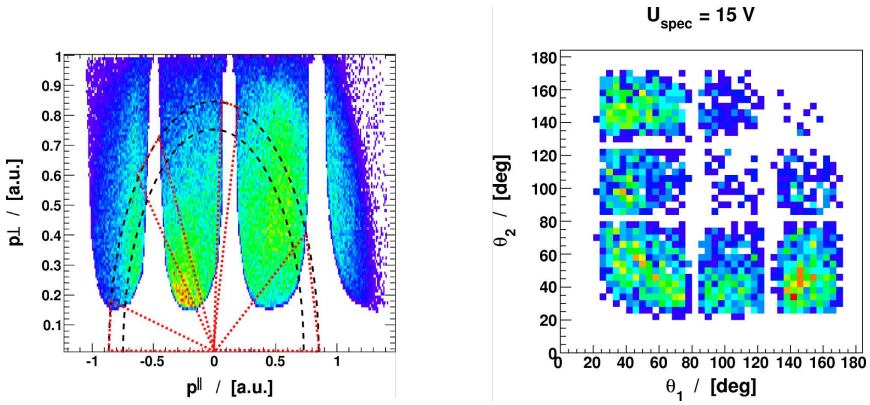

Figure 3.16: The blank areas in the momentum space of the electrons (left) result from the central bore in the electron detector. At a particular energy (8-10 eV) shown as circular slice in momentum space, the detector hole leads to a limited angular acceptance for the polar angle $\theta_{1,2}$ for both detected electrons (right).

the momentum phase-space of the two detected electrons (like in Fig. 3.15 (right)). This section demonstrates the feasibility of filling these blank areas by several runs of measurement with different spectrometer voltages. The data shown here are taken from the experiment studying double ionization at an impact energy of $E_0 = 105\,\mathrm{eV}$. Here, two of the three slow electrons emerging from the collision have to be detected in order to gain the full kinematics. Different to the case of single ionization, where the scattered projectile is very fast and the ejected electron is slow, both electrons have comparably low energy in double ionization. This means, that the holes in momentum space appear for both detected electrons labeled (1) and (2). The magnetic field was set to $B = 6\,\mathrm{Gauss}$, which leads to an upper limit of $p^{\perp}_{1,2} = 1\,\mathrm{a.u.}$ and a lower limit of $p^{\perp}_{1,2} = 0.2\,\mathrm{a.u.}$ of the transverse component. The accelerating voltage was set to $U = 15\,\mathrm{V}$ in the first run of the measurement. To visualize the problem of detecting two electrons, it is easier to consider the angular acceptance only for a selected range of electron energy. In the representation of the momentum space already chosen in sec. 3.4.1, this corresponds to a cut of a circular band which is also shown in Fig. 3.16 (left). The polar angle of the electron θ is defined as the angle between projectile axis and its momentum vector by $\theta = \arctan(p^{\perp}/p^{\parallel})$. Then, the holes in momentum space correspond to specific polar angles $\theta_{1,2}$, for which the electrons at the chosen energy E_2 cannot be detected. By limiting the consideration to a specific cut in E_2, the blanks in momentum space can be represented as stripes in the distribution of polar angles of *both* electrons simultaneously, as shown on the right side in Fig. 3.16. The angles $\theta_{1,2}$ at which there is no acceptance are different for each electron energy. For the example shown in Fig. 3.16 the electron energy has been chosen to be $E_{1,2} = 8\,eV - 10\,eV$.

In order to 'fill' the holes for the two detected electrons, three measurement runs were undertaken, each with a different spectrometer voltage (first run: 15 eV, second run: 12.25 eV, third run: 18,5 eV). For each spectrometer voltage, the holes in momentum space are shifted in horizontal direction. As a result, the missing events from the first run of the measurement can be filled by the events recorded in the second run. In the representation showing the blank bars in the polar angles of both electrons, the second run will now fill the blanks of the first run. However, the second run itself has blanks again. As a result, the intersection of the blank bars from both measurements will remain empty. Therefore another third run was undertaken, where the last blank patches in the polar angles were filled. The individual contributions of each measurement run are shown in Fig. 3.17 again for a selected electron range of $E_{1,2} = 8\,eV - 10\,eV$. Electrons which are emitted approximately in direction of the projectile axis, which is equivalent to a small transverse momentum component $p^{\perp}$, cannot be detected at all due to the hole in the detector. This cannot be cured by taking different measurement runs at different spectrometer voltages, and therefore there are

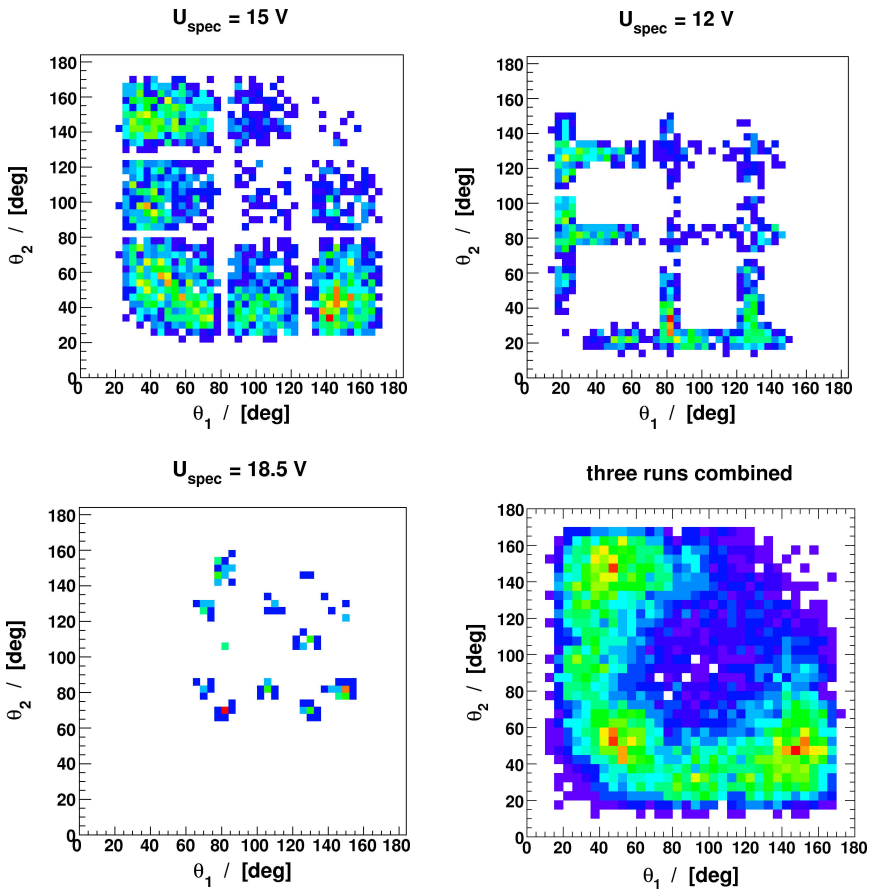

Figure 3.17: The blank areas in the angular acceptance for the electrons can be filled by combining three measurement runs at different spectrometer voltages U_{spec}. The spectrum in the lower-right corner shows all three runs combined for a selected electron energy $E_{1,2} = 8 - 10\,\mathrm{eV}$.

remaining blank areas in a range of $\theta \leq 20°$ and $\theta \geq 160°$.

Another issue, which can be seen in the spectrum showing the number events as function of the polar angles of the two electrons θ_1 and θ_2, is a possible influence of the electronic deadtime. Picking the example where both electrons have equal energy $E_{1,2} = 8\,eV - 10\,eV$, two hits arriving at the same time also have the same longitudinal momentum. Since both considered electrons have the same energy, they also have the same transverse momentum[4] and therefore electrons arriving simultaneously have equal polar angles $\theta_1 = \theta_2$. Any deadtime limitations for electrons arriving simultaneously on the detector should lead to blank area in Fig. 3.17 in the diagonal, where $\theta_1 = \theta_2$. As it can be seen, the area is filled, which is an indication, that the deadtime limitations are not present. This has been tested by omitting the reconstruction which was discussed in sec. (3.3). Without the reconstruction routine the area around $\theta_1 = \theta_2$ remained empty.

3.4.2 Calibration and Resolution for Electrons

The accuracy of the momentum spectroscopy depends on how well the accelerating voltage U, the acceleration distance a, the drift length d and the magnetic field are known. Instead of individually measuring these parameters, they can be determined in a calibration procedure which is outlined in this section. The method to a great part relies on the fact, that all final-state particles are detected, and is presented using the example of single ionization at $E_0 = 102\,eV$ impact energy, where their full kinematical information is accessible.

The precise value of the magnetic field B can be found by evaluating the distance between two wiggles in the spectrum of Fig. 3.15 and by eq. (3.9). The magnetic field can be hereby determined with a precision of less than 1%. The absolute time-of-flight, like in Fig. 3.15, is not known a priori from the measurement of the arrival time of the electron, but has to be determined by extrapolating wiggles in steps of integer numbers $n \cdot t_{wig}$ (n=1,2,3,...) to earlier times. The zero point of the time-of-flight $t = 0$ is found for a particular n, since the 'first' wiggle has to be at $t = 0$ where the electrons trajectory start in the interaction point. The actual strength of the accelerating field U/a (U: acceleration voltage, a: acceleration distance) and the actual drift path d which is needed to deduce the longitudinal momentum from the time-of-flight can be calibrated by evaluating the energy sum of all detected final-state electrons. In single ionization of an atom the initial energy E_0 is shared among the electrons

$$E_0 = E_1 + E_2 + Q \tag{3.20}$$

where $E_{1,2}$ is the energy of the scattered projectile and the ejected electron after the reaction and Q is the change of internal energy. For single ionization

[4]The azimuthal angle may still be different for both electrons

in the ground-state of He^+, this is just the ionization potential $Q = IP = 24.6\,\text{eV}$. If the atom is additionally excited to an energetically higher lying state of He^+, the Q-value is increased by the excitation energy. For instance the first excited state of He^+ with principle quantum number $n = 2$ has an excitation energy of $E_{exc} = 40.8\,\text{eV}$, such that $Q = IP + E_{exc} = 65.5\,\text{eV}$. If both electrons are detected with sufficient resolution, the energy-sum $E_1 + E_2$ should have a constant value $E_0 - Q$ corresponding to the overall loss the incoming projectile-energy E_0. The energy sum sensitively depends on the individual momentum components $p_1^{\parallel}, p_1^{\perp}, p_2^{\parallel}, p_2^{\perp}$, where the acceleration field and the drift path enters into the determination of the longitudinal momentum. A wrong choice of these parameters will lead to miscalculated $p^{\parallel}$ and thus also of the energy sum. The proper calibration is found, when the energy sum is independent of transverse and longitudinal momentum of *both* individual electrons. An example showing that the energy sum is independent of the longitudinal momentum of the scattered projectile and the slow electron is presented in Fig. 3.18a, where the energy sum of the two outgoing electrons after single ionization of He by 102 eV electrons is shown as a function of the longitudinal momenta and $p_1^{\parallel}$ and $p_2^{\parallel}$. The distribution is clustered along two parallel vertical lines, where the first line at $E_{sum} \approx 80\,\text{eV}$ represents the ionization into the ground state of He^+. The second line represents excitation into the levels with $n = 2$ and $n \geq 3$, visible as additional peaks in the energy-loss (Fig. 3.18b). The proper distance between those peaks is a further indication of a good calibration.

The width of the peaks gives the resolution in the determination of the longitudinal $p^{\parallel}$ and transverse momentum $p^{\perp}$ of the final state electrons. As the energy resolution is determined by the individual momenta, the resolution of the three momentum components will be addressed.

The relations eq. (3.8), (3.12) and (3.13) which are used to reconstruct the electron momentum $(p^{\parallel}, p^{\perp}, \phi)$, can be used to estimate the influence of uncertainty in the measurement of the time-of-flight δt and the position on the detector δr by gaussian error propagation. For the longitudinal momentum this results in a lengthy expression. For the transverse components the analytical expression has some instructive features.

$$\Delta p^{\perp}(r, \delta r, t, \delta t, B) \propto \frac{B}{2|\sin(\frac{1}{2}\omega t)|}\sqrt{(\delta r)^2 + \left(\frac{r \cdot \omega \delta t}{2\tan(\frac{1}{2}\omega t)}\right)^2} \quad (3.21)$$

$$\Delta\phi(r, \delta r, t, \delta t, B) = \sqrt{(\frac{\delta r}{r})^2 + (\frac{1}{2} * \omega\delta t)^2} \quad (3.22)$$

For the longitudinal component the resolution $\Delta p^{\parallel}$ only depends on the time-of-flight, whereas $\Delta p^{\perp}$ and $\Delta\phi$ additionally depend on the radial position $r \propto |\sin(1/2\omega t)|$ on the detector. Both can be translated to longitudinal

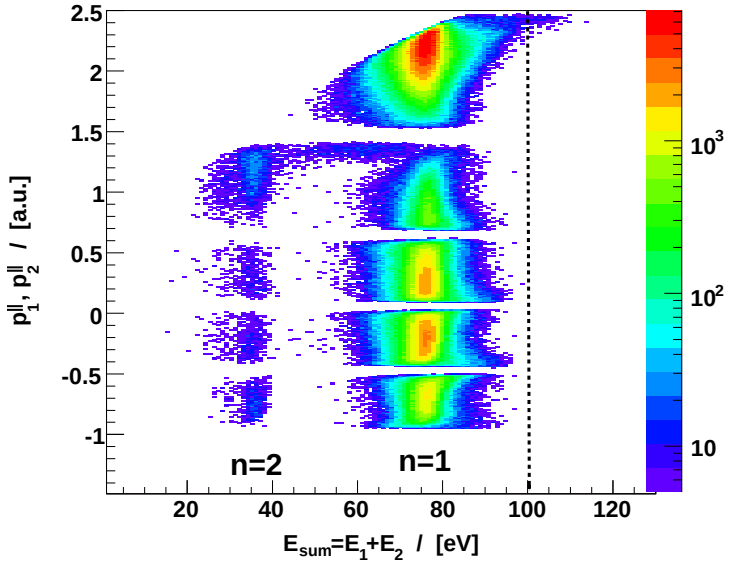

(a) Energy-sum as a function of the individual longitudinal momenta of the final state electrons (1) and (2).The dotted line denotes the energy of the incoming projectile.

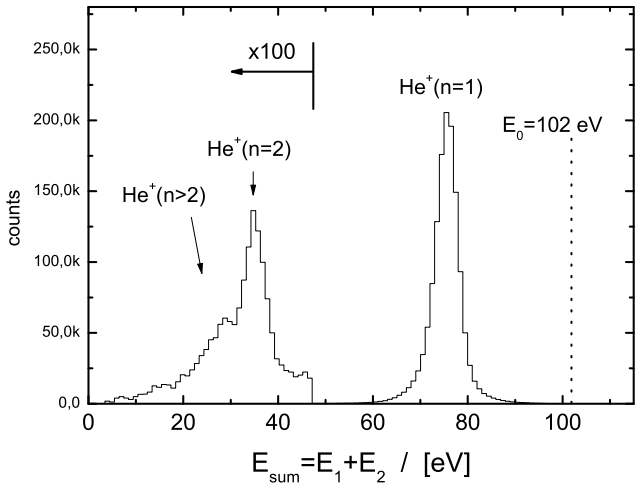

(b) Energy-sum showing the individual states of the residual He^+-ion with n=1 and n=2 after single ionization. The width of the peak is a measure for the resolution of the electron momentum.

Figure 3.18: Energy sum of both final-state electrons in single ionization of helium with 102 eV projectile energy.

and transverse momentum with eq. (3.8) and eq. (3.12) , and the resolution can be plotted as a function of these two quantities as in Fig. 3.19. The uncertainty in the time-of-flight measurement is given by the time-structure of the projectile pulse of 1.5 ns, which prevails over the timing resolution of the electronic circuit. The spatial resolution δr is determined by the finite transverse extension of the interaction volume and the position resolution of the delay-line anode. The transverse extension of the interaction volume is given by the beam focus (<1 mm). Together with the position resolution of the delay-line anode of about 0.5 mm and the resolution in determining the arrival position on the detector, the net resolution is estimated to $\delta r \approx$1 mm. These are the values which enter the calculated resolution shown in Fig. 3.19 for a specific spectrometer setting, namely 18.5 V acceleration voltage and a magnetic field of 6 Gauss.

For the transverse components the expressions in eq. (3.21) show an interesting and important feature. The dependence on the absolute time-of-flight t only enters by periodic factors, which accounts for the cycling motion and the wiggles. Electrons arriving at the detector with this particular time-of-flight, are near the spectrometer axis where there is no resolution. Otherwise, the dependency with respect to the uncertainty in the time-of-flight measurement depends only on $\delta t/\omega$, which is the uncertainty relative to the time for one cyclotron revolution. Therefore even for high energy scattered electrons with very short flight times the good resolution for the transverse component persists, whereas the uncertainty δt makes it impossible to resolve the longitudinal component, because of the very short time-of-flight. The magnetic field can be adjusted accordingly, such that the absolute time-of-flight of the scattered projectiles is in between two wiggles, where the resolution for the transverse components is best.

The width of the energy sum ΔE_{sum} is a measure for the resolution of the electron momentum spectroscopy and is a function of the individual momentum components of both electrons $p^1_\parallel$, $p^1_\perp$, $p^2_\parallel$, $p^2_\perp$ (see Fig. 3.18). For the presented case in Fig. 3.18 the energy resolution of $\Delta E_{sum} \approx 6.5$ eV (FWHM) is dominated by the poor longitudinal resolution of the fast scattered projectile. Its energy resolution is estimated to be around $\Delta E_1 \approx 4.5$ eV (FWHM). The energy spread of the projectile beam presents a minor contribution and is estimated to be less than 0.5 eV, which is a typical value for the electron gun used in the experiment. The angular resolution $\Delta\phi$, however, doesn't enter the energy sum and cannot be really 'tested'.

In conclusion, the detection of all final state electrons opens the way to accurately calibrate the electron-side of the spectrometer and to monitor the resolution of the measurement.

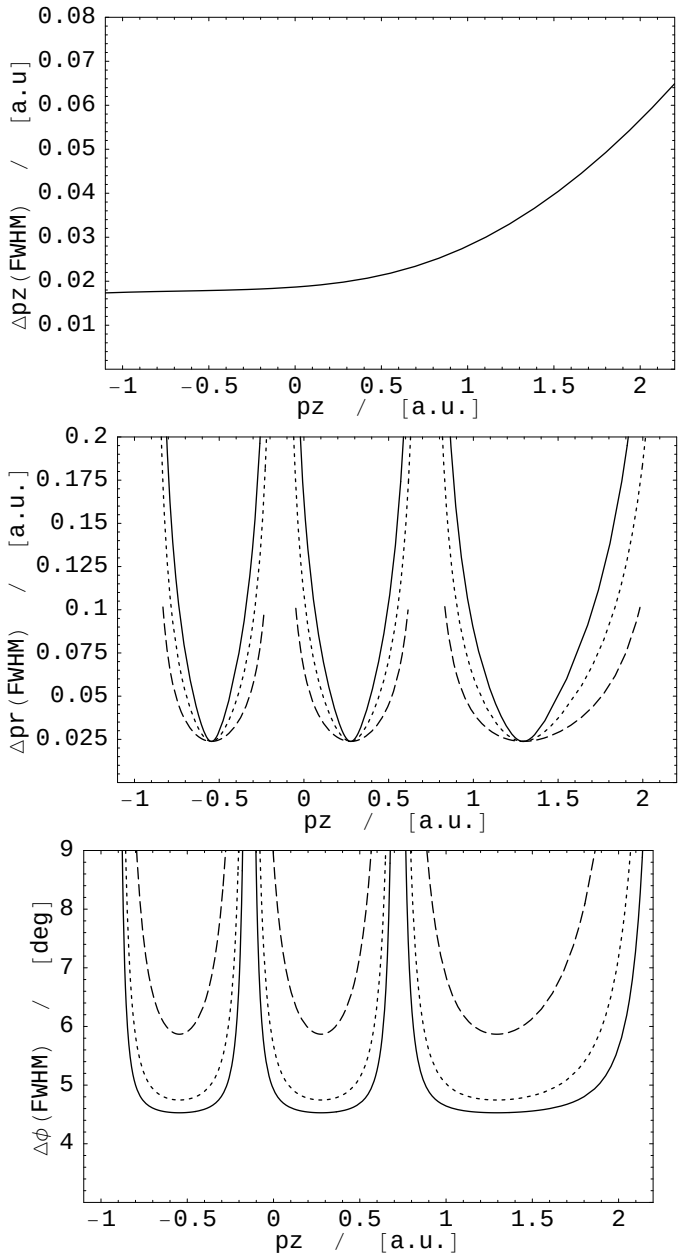

Figure 3.19: Resolution for determination of the momentum components $(p^{\parallel}, p^{\perp}, \phi)$ for a spectrometer voltage of $U = 18\,\mathrm{V}$ and a magnetic field of $B = 6\,\mathrm{Gauss}$. The curves are calculated using gaussian error propagation assuming an error of $\delta t = 1.5$ ns and δr =1 mm in the determination of the time-of-flight and the arrival position respectively. The curves show the resolution for electrons with three different transverse momenta : $p^{\perp} = 1.5$ a.u. (—), $p^{\perp} = 0.75$ a.u. $(\cdots)$, $p^{\perp} = 0.35$ a.u. (- - -).

3.4.3 Calibration and Resolution for Ions

Again using the example of single ionization of He at $E_0 = 102\,\mathrm{eV}$, the overdetermined kinematics allows to check the momentum conservation in all three spatial directions x,y and z:

$$\vec{p_0} = \vec{p_1} + \vec{p_2} + \vec{p_{ion}}. \tag{3.23}$$

Since the electron spectrometer can be calibrated from energy conservation, which only depends on the momenta of the electrons, the ion spectrometer can be calibrated by making use of momentum conservation, where the properties of all final state particles enter. The sum of their momenta has to be equal to the momentum of the incoming projectile $(p_0^x, p_0^y, p_0^z) = (\sqrt{2E_0}, 0, 0)$.

Like for the electrons, the precise time-of-flight of ions with zero longitudinal momentum $E^{\parallel} = 0$ has to be found. If all final-state particles are detected, the sum of their momenta in longitudinal direction has to be equal to the initial projectile momentum and the proper value of $t(E^{\parallel} = 0)$ can be thus found (Fig. 3.20b).

For the transverse components of the ion momentum, the momentum balance allows to precisely calibrate the spectrometer. As mentioned previously, the kinetic energy due to the momentum transferred through the collision is as low as a few meV. Therefore, the ion trajectory is far more sensitive to field inhomogeneities, such as a lensing effect caused by curved equipotential surfaces inside the spectrometer. Such lensing appears in the transition between acceleration and drift region resulting from the inevitable gap in between. Its influence has to be estimated by ray-tracing simulations (e.g. SIMION, see [MFK03]) or by making use of momentum conservation. By rescaling the displacement r of the arrival position of the ion, the lensing effect can be corrected for, such that the momentum conservation is ideally fulfilled. In addition to the lensing effect the ion is slightly deflected by the magnetic field. Because of the ion's high mass, it typically fulfills a small fraction of a cylcotron motion, however this effect can be accounted for by rotating the position of the ion around the symmetry point r_0. The proper calibration has been found when the summed electron momenta balances the momentum of the ion (see Fig. 3.20a).

The resolution of the recoil ion momentum spectroscopy critically depends on the temperature of the target species. For helium the velocity-distribution at room temperature (300 K) leads to a momentum distribution with a width of 6 a.u. The transfered momentum during a collision, which is in the order of 1 a.u., therefore cannot be resolved if the target is not internally cooled. With the present setup the estimated internal temperature is estimated to be approximately 1 K. With the succeeding apertures atoms with high velocity components transverse to the target beam are filtered out, which leads to further cooling to an estimated temperature of 0.8 K.

Hence the resolution is poorest *in* target-beam direction (i.e. y-direction) and cannot be reduced. To summarize this, the initial target temperature leads to following spread in terms of momentum

$$\Delta p^x_{thermal} = 0.12\, a.u.$$
$$\Delta p^y_{thermal} = 0.24\, a.u.$$
$$\Delta p^z_{thermal} = 0.12\, a.u.$$

In the x-and y-direction the errors from the finite size of the interaction volume have to be considered in addition to the initial temperature spread. In longitudinal z-direction the time-focussing geometry cancels the effect of the target extension and the uncertainty of the time-of-flight measurement plays a negligible role.

The uncertainty of the determination of the position δr states a significant contribution which enters into the relation of eq.(3.5) for the reconstruction of the transverse momenta.

$$(\Delta p^x_{ion})^2 = \left(\frac{1}{2a}\sqrt{\frac{1}{2}qUM}\right)^2 \cdot \delta r^2 + (\Delta p^x_{thermal})^2$$
$$(\Delta p^y_{ion})^2 = \left(\frac{1}{2a}\sqrt{\frac{1}{2}qUM}\right)^2 \cdot \delta r^2 + (\Delta p^y_{thermal})^2.$$

Adding up the contributions from the finite temperature and the limited position resolution ($\delta r = 1\,\mathrm{mm}$) leads to following values:

$$\Delta p^x = 0.28 \text{ a.u.} \tag{3.24}$$
$$\Delta p^y = 0.38 \text{ a.u.} \tag{3.25}$$
$$\Delta p^z = 0.12 \text{ a.u.} \tag{3.26}$$

For the longitudinal direction $p^{\parallel}$ the distribution peaks at the value corresponding the initial projectile energy of 102 eV (Fig. 3.20b). The width is given by the poor resolution of the ion and of the rather fast scattered projectile. The result of 0.16 a.u. (FWHM) favorably agrees with the expected value calculated from the presented formulas and clearly indicates the low temperature in the transverse target-beam direction of less than 1 K.

The momentum balance in the transverse direction is shown in Fig. 3.20a, where the sum-momentum of the final state particles has to be zero, since the incoming projectile has a vanishing transverse momentum. The width reflects the summed resolution to determine the momentum of the two electrons and the ion. The larger width of the momentum components in y-direction (which is the direction of the jet) reveals the higher temperature

as opposed to the temperature transverse to jet stream (i.e. x-direction). That the resolution is worse than the estimated values in eq. (3.24) is due the additional uncertainties from the electron momenta and inhomogeneities of the electric field. Apart from the possibility to calibrate the reconstruction of the ion momenta, the determination of the resolution allows to confirm the quality of the imaging properties of the spectrometer.

The apparent upper limit of the width Δp^y in jet-direction shows the efficient cooling during the expansion and that the information gained out of the spectroscopy is not 'contaminated' by hot target atoms. Further it provides the proof, that there is no background present which is of major importance, since elastically scattered electrons may not be separated from inelastically scattered projectiles without selective elements in the arrangement of the detector.

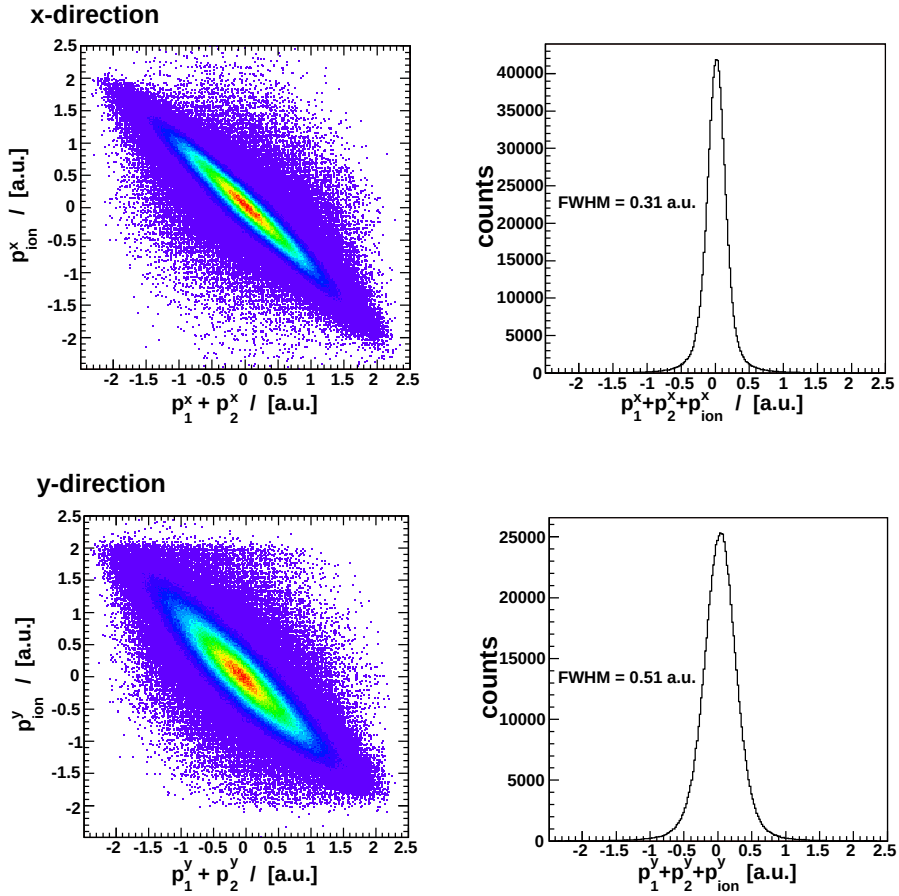

(a) The left column shows, how the sum-momentum of all final state electrons balances the momentum of the recoil ion for the x- and y-direction, respectively. The right column shows the width of the summed momentum of all final state particles, providing information on the momentum resolution of each component.

Figure 3.20: The spectra show the momentum balance of the final state particles (2 electrons and a He^+-ion) after single ionization of He with $E_0 = 102\,\text{eV}$ electrons.

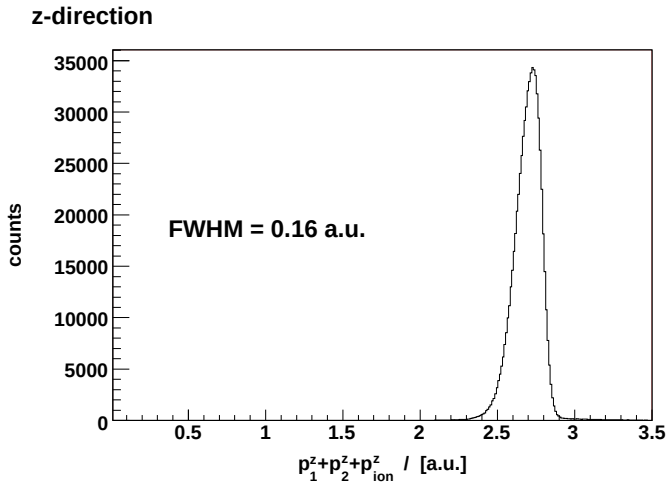

(b) The sum momentum of all three final state particles in the z-direction after single ionization of He by 102 eV electrons. The peak position is at the position of the initial momentum of the incoming projectile $p_0^{\parallel} = 2.72$ a.u.

Figure 3.20: continued.

Chapter 4

Experimental Results

Kinematically complete experiments on single ionization, also known as the (e,2e) process, have been extensively performed starting with the experiment by Ehrhardt et al. in 1969 [ESTW69]. Later the studies were extended to double ionization, or correspondingly the (e,3e) process, by Lahmam-Bennani et al. in 1989 [LBDD89]. With the introduction of reaction microscopes in 1994 [MUS$^+$96], for the first time kinematically complete experiments in ion impact could be studied. The modern imaging technique marked a great leap forward and provided comprehensive data sets, which were not conceivable in electron impact ionization with the mentioned 'conventional' techniques. For this reason, the imaging technique was applied also for electron-impact studies hat high energies beginning from 1999 [DMS$^+$99], which however lacked from several drawbacks resulting from the peculiarities, which occur when an electron projectile beam is used [UMD$^+$03].

In the present chapter the results from three different fragmentation studies of helium are presented. These have only become possible by the technical refinements which were undertaken on the original reaction microscope used for electron-impact ionization studies. The new advanced reaction microscope surpasses existing conventional techniques in angular acceptance, aquisition time and background suppression and thus provides a set of complete and consistent data. The refinements represent a step forward, which now allows to obtain single ionization cross sections with a resolution so far unreachable with the previous reaction microscope. Furthermore, cross sections for ionization-excitation and double ionization, both processes with typically low cross sections, were recorded at so far not accessible impact energies, neither by 'conventional' techniques nor by the previous reaction microscope.

4.1 Single Ionization at $E_0 = 1\,\mathbf{keV}$ and $E_0 = 102\,\mathbf{eV}$

Most electron impact experiments measuring the fully differential cross section were restricted to the so called coplanar scattering geometry where the ionized electron is ejected into the scattering plane spanned by the incoming and scattered projectile momentum vectors $\vec{p_0}$ and $\vec{p_1}$. That this might not be a sufficient test was demonstrated in the recent kinematically complete experiment for fast ion impact (100 MeV/u C^{6+}) ionization of helium where for the first time, the full 3D emission pattern of the slow ($E_2 = 6.5\,\mathrm{eV}$) ionized electron was measured [SMF$^+$03]. The experiment was performed in the perturbative regime at small energy and momentum transfer, at a projectile velocity of $v_P = 60\,\mathrm{a.u.}$ and a projectile charge of $Z_P = 6$. Thus, the perturbation parameter $Z_P/v_P = 0.1\,\mathrm{a.u.}$ is small and perturbative methods are expected to hold. However, the cross sections revealed an unexpected strong electron emission out of the scattering plane which could not be reproduced by a state-of-the-art continuum distorted wave calculations which, on the other hand, showed good agreement inside the scattering plane (see Fig. 2.7). Since the observed structure violates the axial symmetry with respect to the direction of $\vec{q}$, which is characteristic for first order processes, it is a clear signature of a higher order process. The troubling issue is however, that all models going beyond a first order description fail to reproduce the out-of-plane structures. So far, no quantitative theoretical description has been reported, however, the failure of the calculation presented in Fig. 2.7 has been traced back to its deficiency of describing situations in which all three collision partners are close together [MFF$^+$03].

Here the question arises whether similar out-of-plane structures are present for electron impact ionization as well and if present state of the art theories which so far have been tested mainly in coplanar geometries are able to reproduce the experimental results outside the scattering plane. Corresponding out-of-plane studies for electron impact are scarce and the main interest concentrated on low impact energies ($E_0 \leq 100\,\mathrm{eV}$) [MWR92, MR92, RRF$^+$92b, RBFM96], where the correlation between all three participants of the collision is strong and theory is severely challenged. For asymmetric kinematics at intermediate impact energy of 105 eV Beaty et al. [BKHM78] measured the FDCS in non-coplanar geometry, where the shape of the binary lobe was studied. However, no peculiarities were found. In conclusion, the existing differential data in electron impact is only available in selected cuts revealing small patches of the full final momentum space. Until now, comprehensive cross sections presented in three-dimensional images have been available for ion impact ionization only, showing unprecedented details of the collision process. The 'advanced' reaction microscope allows to record high-resolution 3D images, and to provide FDCS for almost all angles of low energy electron emission ($E \leq 15$ eV) in an (e,2e) experiment. Therefore two (e,2e) experiments were performed at two different impact-energies, one at

the high impact energy of 1 keV and a second at $E_0 = 102$ eV which is in the 'intermediate' regime. In the present chapter following issues will be addressed:

1. At the high impact energy of 1 keV, which corresponds to a projectile velocity of $v_P = 8.57$ a.u., the perturbation Z_P/v_P has almost the same strength as in the collision using 100 MeV/u C^{6+} projectiles, where the results remain puzzling up to the present day. At the same momentum and energy transfer, the FDCS of both collisions can be directly compared with each other for projectiles with different charge sign. The behavior under the change of the sign of Z_P/v_P can serve as a guide to unravel some of the dynamics, leading to the strong out-of-plane emission in the case of ion impact.

2. The motivation is to deliver a comprehensive set of the fully differential cross section for collision at small momentum and energy transfer, covering a large part of the final-state momentum space where most events occur in electron impact ionization. Firstly it should be clarified, whether similar out-of-plane structures are observed in the cross section as for ion impact ionization and, secondly, if present state of the art theories, like the Convergent Close Coupling (CCC), are able to reproduce the experimental results. Therefore the FDCS was measured at 102 eV impact energy, where it can be compared with the CCC calculation. At 1 keV calculations using this method are not yet available.

3. Moreover, with the 'advanced' reaction microscope used in the electron impact experiments, the FDCS is obtained with a higher resolution for the momentum transfer compared to the previous ion impact data and allows to cross check the influence of the resolution on the measured cross sections. In a recent publication [OF05] it was claimed, that some discrepancies between experimental and theoretical cross sections in ion impact ionization can be explained by the limited resolution of the reaction microscope for the momentum transfer. This point should be addressed with the experimental opportunities given with the 'advanced' reaction microscope.

4.1.1 Notation for the FDCS

As already outlined in chapter 2, single ionization of an atom or molecule is a very basic and also simple dynamical few-body process. So-called (e,2e) experiments proved to provide the most detailed insight into the dynamical mechanisms and the most stringent test for theory. The measured quantity, the fully differential cross section (FDCS), is usually expressed

as $d^3\sigma/d\Omega_1 d\Omega_2 dE_2$, where $d\Omega_{1,2}$ are the solid angles of the two outgoing electrons. The relation with the T-matrix is

$$\frac{d^3\sigma}{d\Omega_1 d\Omega_2 dE_2} = (2\pi)^4 \left(\frac{p_1 p_2}{v_p}\right) |T_{fi}|^2. \tag{4.1}$$

For high incident energy, most collisions occur at low momentum and energy transfer to the target, leading to the so-called asymmetric scattering geometry. Exchange effects can be neglected and the fast final-state electron is identified with the scattered projectile and is labeled with (1). The slow electron (2) is the electron ejected from the target, which leaves the reaction with the kinetic energy E_2. In this case the FDCS is very often presented as a function of the emission angle of the ejected electron at fixed scattering angle θ_1 and a fixed energy of the ejected electron E_2 (see Fig. 4.1). The incoming projectile direction together with the direction of the scattered projectile define the 'scattering plane' (see Fig 4.1). The fully differential cross section is represented as a function of the emission angle of the ejected electron θ_2 and ϕ. Coplanar geometry corresponds to $\phi = 0°$, the perpendicular geometry to $\phi = 90°$.

As can be seen from energy conservation

$$E_0 = \mathrm{IP} + E_1 + E_2, \tag{4.2}$$

the final-state electrons carry the excess energy. The energy of the ion can be safely neglected due to its high mass. Here E_0 is the energy of the incoming projectile, IP is the binding energy of the ejected electron (=ionization potential≈24.6 eV for He) and $E_{1,2}$ is the energy of the two outgoing electrons, respectively.

By keeping the scattering angle θ_1 and the energy of the ejected electron fixed, the momentum transfer vector defined by $\vec{q} = \vec{p_0} - \vec{p_1}$ is uniquely determined. This representation is chosen, because the momentum transfer plays an important role in the collision dynamics in the asymmetric geometry, which is revealed in the angular emission pattern of the ejected electron.

4.1.2 (e,2e) on Helium at 1 keV Impact Energy

The primary goal of arranging the projectile beam parallel with the imaging fields was to study electron impact ionization at low projectile energies. However, even at high projectile energies the new arrangement gives rise to a number of advantages, because now the scattered projectile can be detected. For low energy and momentum transfer (i.e. for the collisions of interest in this work), the scattered projectile is still fast, such that the longitudinal momentum cannot be resolved (see Fig. 3.19). This does not result in any major drawback, due to the specific kinematics at high impact energies and asymmetric geometry, which is discussed in the appendix (see

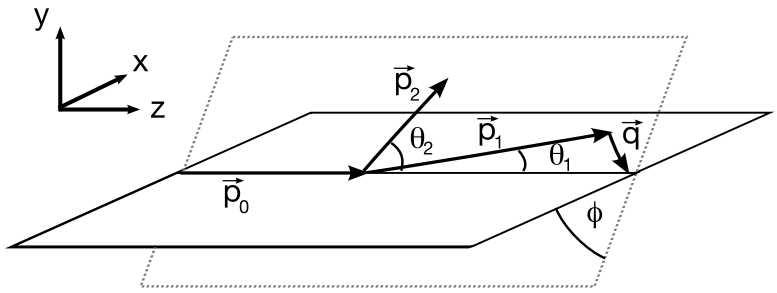

Figure 4.1: Schematical view of the collision geometry for the studied (e,2e) reactions. The solid lines represent the scattering plane, with the scattering angle of the scattered projectile θ_1. The emission plane of the ejected electron is represented by the grey dotted lines.

sec. A.1.1). Nevertheless, the transverse momentum of the fast scattered electron can still be determined with a resolution, which is by factor two to three better than in ion impact experiments, where this information has to be inferred from the target fragment momenta. With the coincidence electronics triple coincidences of two electrons and an ion were recorded. Although only two of the three final state particles have to be detected for full kinematics, the triple coincident detection leads to suppression of background. In addition, spectrometer properties like the resolution can be tested by checking momentum conservation in a similar way as it was discussed in sec. 3.4.3.

3D images of the Cross Section

In Fig. 4.2 the three dimensional electron emission pattern is plotted for single ionization of He by 1 keV electron impact and three different momentum transfers of $q = (0.5 \pm 0.11)$ a.u., $q = (0.75 \pm 0.11)$ a.u. and $q = (1 \pm 0.2)$ a.u. The energy of the ejected electron is chosen to be $E_2 = (10 \pm 3.5)$ eV. Hereby the scattering angles become fixed and can be calculated from the resulting collision geometry. In this representation the FDCS for a particular direction is given as the distance from the origin of the plot to the point on the surface which indicates the direction of $\vec{p_2}$. The 3D polar plots are not presented on the same absolute scale, instead each plot has been rescaled such that they all have approximately the same size. The absolute FDCS can be taken from the cuts applied to the three dimensional emission pattern which are discussed later.

The cross section patterns are governed by the well known double lobe structure already discussed in sec. 2.1.2, with the larger binary lobe in direction of the momentum transfer vector $\vec{q}$, and the smaller recoil lobe in the opposite direction. With increasing momentum transfer the relative height of binary lobe relative to the recoil lobe increases with intensity, which can

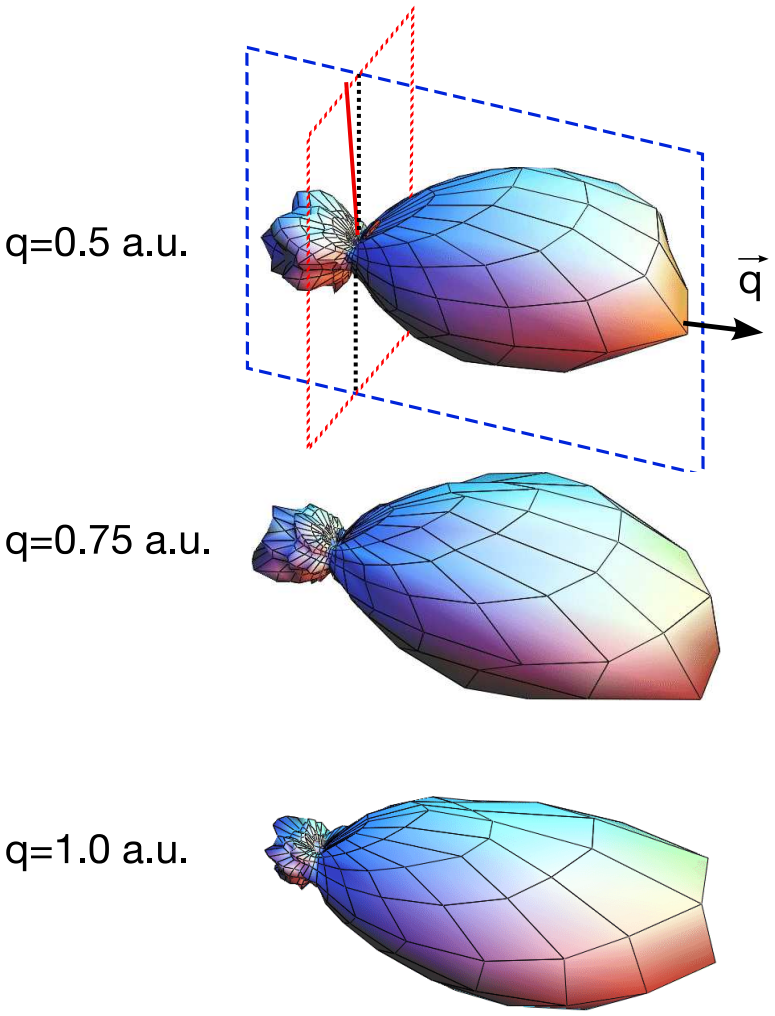

Figure 4.2: Three dimensional FDCS for single ionization by 1 keV electrons showing the emission of electrons with $E_2 = 10$ eV. The cross sections are presented for three different momentum transfers $|q| = 0.5$ a.u. (top), 0.75 a.u. (middle) and 1 a.u. (bottom). In the image showing the cross section at $q = 0.5$ a.u., the scattering plane (dashed lines) and the plane perpendicular to the scattering plane (dotted lines) are displayed. In addition the axis of the incoming (dotted line) and scattered projectile (solid red line) are shown.

be understood easily remembering the expansion of the first Born interaction operator in eq. (2.35). At larger momentum transfer beyond the regime of the dipole limit higher-order multipoles contribute stronger, giving rise to increasing deviation of the cross section of the dipolar pattern. Moreover, the momentum transfer of 1 a.u. corresponds nearly the momentum of the ejected electron with 10 eV energy. At this kinematical condition where the momentum transfer is equal to the momentum of the ejected electron, the so called Bethe-Ridge, the electron can be ejected by a binary knock-out collision with the projectile. In such hard collisions, the nucleus remains a spectator and hardly participates in the collision. Then, to some extent, the shape of the binary peak is not determined by the dynamics of the collision, but rather due the initial momentum of the bound electron, representing the so-called Compton profile. Even though the compton profile plays a role for all kinematical situations, it only becomes 'unmasked' under the binary knock-out conditions, which is also used in (e,2e) spectroscopy.

For the FDCS presented in Fig. 4.2, the out-of-plane electron emission is far less pronounced than for ion impact (Fig. 2.7). Secondly, it becomes increasingly visible at large momentum transfer. Especially for $q = 1$ a.u. the binary and the recoil lobe are connected by some sort of bridge. Clearly, the out-of-plane emission violates the symmetry with respect to the momentum transfer $\vec{q}$ and therefore has to be attributed to higher-order interactions between the projectile and the target.

For a quantitative comparison of the cross sections (Fig. 4.3), two cuts are applied for each of the 3D cross sections, one in the scattering plane ($\phi = 0°$ in Fig. 4.1) and the second in the perpendicular plane ($\phi = 90°$ in Fig. 4.1). The data are compared with predictions of a first Born calculation (FBA) and a calculation using three Coulomb waves (3C). In both cases the initial state is described by a product of an incoming plane wave representing the incoming projectile and a correlated Hylleras wavefunction representing the ground state of helium. In the FBA the final state is represented by an outgoing plane wave for the outgoing electron and a Coulomb wave for the ejected electron. In the 3C calculation the two continuum electrons in the final state are represented by Coulomb waves, which represent the motion of the electrons on the field of the residual He^+ ion. An additional Coulomb factor accounts for the interaction between the two outgoing electrons, hence the name 3C. Despite the rather high impact energy, where the interaction of the fast scattered projectile with the fragments should be weak, the cuts in the scattering plane show a visible disagreement between the FBA calculation and the absolute data. The disagreement becomes stronger with increasing momentum transfer, which can be understood in following intuitive picture. Classically, the momentum transfer, or alternatively the scattering angle, can be related to the impact parameter of the collision. Larger scattering angles appear for close collisions, whereas at lower scattering angles a glancing collision between the projectile and the target occurred. At close

collisions multiple interactions become more probable.

However, the inclusion of higher-order interactions between the scattered projectile and the fragments within the 3C model shows perfect agreement in the scattering plane. That such higher-order effects have to be included in the description of the FDCS, even for asymmetric kinematics with a slow electron and a fast projectile, is a well known fact and is attributed to the long range nature of the Coulomb force [ACF$^+$87, LBAFS88]. The contributions from higher-order interactions between the projectile and the target, are only observed in higher differential cross sections at high energies. For the FDCS in asymmetric geometry, full experimental agreement with the FBA is established only at the very high impact energy of 4 keV [DCLB$^+$87]. On the other hand, the total single ionization cross section is practically insensitive to higher-order terms down to 1 keV imapct energy [SEMG88].

The so-called post-collision interaction (PCI) between the charged particles in the final state continuum changes the ratio of the binary and recoil peak. At lower impact energies it leads to a considerable shift of the position of the peaks, breaking the symmetry with respect to $\vec{q}$ [EFJ$^+$82]. A slight shift of the peaks with respect to the momentum transfer direction (indicated by an arrow in Fig. 4.3) is hardly observable from the data points alone, but becomes visible comparing the calculations, where the 3C calculation shows much better agreement. Another feature well reproduced by the 3C calculation within the scattering plane is the trend of the binary peak becoming narrower with increasing momentum transfer. The comparison between the calculation and experiment restricted to the scattering plane yields perfect agreement.

Turning the attention to the plane perpendicular to the scattering plane never investigated previously, the situation changes dramatically. The peak centered around 180 ° is the contribution from the recoil peak, which 'leaks' into the perpendicular plane. The respective data points are absent due to the detector hole, through which electrons emitted in the direction of the projectile axis can escape. The out-of-plane electron emission observed in the 3D plots in Fig. 4.2 gives rise to cross section maxima at $\theta_2 = 90°$ and $\theta_2 = 270°$ in the perpendicular plane cuts. For higher momentum transfer they become more pronounced due to the decreasing recoil lobe intensity. The FBA and the 3C calculation show a strong disagreement, even though the 3C calculation excellently reproduces the data in the scattering plane. The reason may be due to a well known deficiency of the 3C wavefunction to describe the system correctly when all three collision partners are close together [LRW99].

The three-dimensional cross sections exhibit emission in the perpendicular plane, like in the case of ion impact in Fig. 2.7. Attention has to be paid to the kinematics, which is different for electron than for ion impact. Because of the high velocity of the projectile compared to the electron impact case, the longitudinal momentum transfer $q^{\|}$ essentially vanishes (see

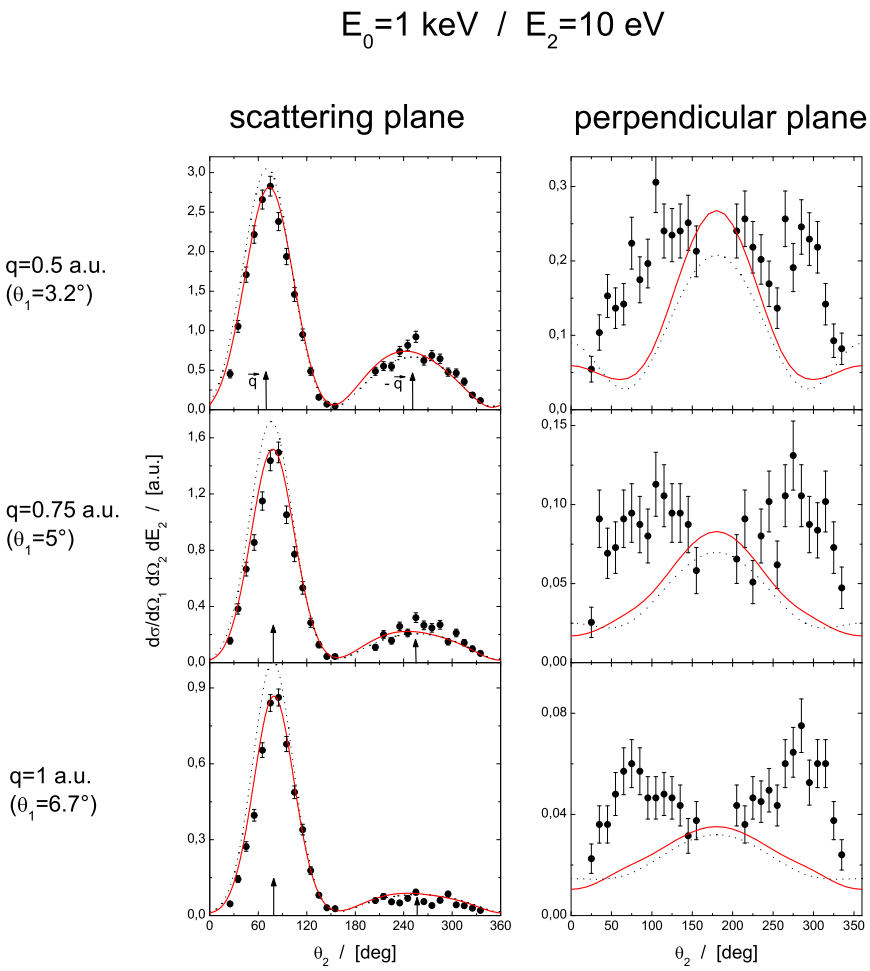

Figure 4.3: Cuts through the three dimensional cross sections from Fig. 4.2. The FDCS (in atomic units) is plotted as a function of the angle of the emitted electron θ_2 with respect to the incoming projectile beam direction, for a fixed momentum transfer q and a fixed emitted electron energy $E_2 =$ 10 eV. The cuts represent the cross section in the scattering plane (left) and in the perpendicular plane (right). The arrows in the scattering plane indicate the direction of the momentum transfer. Theoretical curves: $\cdots$ First Born; — 3C.

A.1.1). Therefore the momentum transfer is almost perpendicular to the incoming projectile axis, and the cut in the perpendicular plane shows the electron emission pattern perpendicular to $\vec{q}$. This is no longer the case for slower projectiles as for $v_P = 8.57$ a.u. in the present electron impact experiment, where due to the non-vanishing $q^{\parallel}$ the momentum transfer is not perpendicular to the incoming projectile axis. As a consequence the plane perpendicular to the scattering plane is not perpendicular to $\vec{q}$, which has to be kept in mind in the further discussion.

Thus it can be stated, that the three-dimensional FDCS in electron impact provides a detailed insight into the ionization process. Surprisingly, a previously unobserved dynamical mechanism appears, which is not apparent in the scattering plane. The great advantage of the non-coplanar geometry is the possibility to study particular scattering geometries, where the dominating first order process leading to the well known and extensively studied dipolar structure is strongly suppressed. In addition, the full emission pattern is recorded at fixed momentum transfer and ejected electron energy. Since the dynamics is generally characterized by the momentum-transfer $\vec{q}$ and the ejected electron energy, only the three-dimensional emission can be seen as a 'complete' picture of the process. This implies, that only models reproducing the data for all emission angles can be seen as adequate description of the process. The 3C calculation apparently fails in this respect.

As discussed earlier, the pronounced features in the perpendicular plane can be attributed to higher-order interactions between the projectile and the target. So far, it can be speculated that these are due to short-range interactions between the projectile and the target, since the long range PCI-effects are incorporated in the 3C calculation which perfectly reproduce the shift of the binary peak as well as the ratio between binary and recoil peak in the scattering plane. In order to gain more insight to the process, the three-dimensional cross section obtained for 1 keV electron impact can be compared with the ion impact data from [SMF$^+$03]. In this way, charge-sign effects of the higher-order contributions can be studied, which so far has been only discussed in theoretical treatments [BBK93, JM03b, VU03]. This is the first time that fully differential data is compared for two different charge signs on such a detailed scale.

Comparison with Ion Impact

First of all the question has to be answered, whether there is any sense in comparing the FDCS on absolute scale for the two collision systems. The answer can be found in the perturbative treatment of the collision, especially in view of the first Born transition amplitude for single ionization. The property of the projectile which enters in a first order calculation is the perturbation $\eta = Z_P/v_P$, i.e. the ratio of the projectile-charge and velocity. In the regime where the perturbative first order treatment is justified, the

total cross section for constant Z_P/v_P is the same for all projectiles, no matter what charge sign, velocity or mass they have. This has been verified for single ionization by protons and electrons and their respective anti-particles [SEMG88, AHK$^+$86, KBNCP90].

For the fully differential cross section the additional important properties entering the transition amplitude are the momentum transfer and the ejected electron energy. In the present case the strength of the perturbation of the 100 MeV/u C^{6+} ion impact collision ($v_P = 60$ a.u.) amounts 0.1 a.u. The perturbation at 1 keV electron impact is slightly larger with $|\eta| = 1/8.57$ a.u.≈ 0.117 a.u., but this difference shouldn't affect the comparison too strongly. Then the experimental FDCS can be directly compared, if the momentum transfer q and the ejected electron energy are chosen to be same. Thus, for the cross sections presented for the two different projectiles the absolute value of the momentum transfer, $|\vec{q}| = |\vec{p_1} - \vec{p_0}|$ has been fixed to $|\vec{q}| = 0.75$ a.u. and the energy of the emitted electron is $E_2 = 6.5$ eV for both cases.

One little detail has to be considered, when comparing the FDCS. Though the transition amplitude considered here is essentially identical for both projectiles, the FDCS in the representation $d^3\sigma/d\Omega_1 d\Omega_2 dE_2$ usually employed in (e,2e) experiments is strongly mass dependent, since equal scattering angles correspond to strongly different momentum transfers. Therefore a better choice is to represent the cross section differential in momentum transfer, and not differential in scattering angle. Such a representation is commonly used in ion impact ionization, where it is more convenient because many different projectiles with different masses and charge states are studied. After some manipulations starting with eq. (4.1) the fully differential cross section can be written as

$$\frac{d\sigma}{d\vec{p_2} d\mathbf{q}^\perp} = \frac{(2\pi)^4}{v_P^2} |T_{fi}|^2 , \tag{4.3}$$

where the transition amplitude is evaluated at the longitudinal momentum transfer $q^\parallel = \Delta E/v_P$. Further $\mathbf{q}^\perp$ is the transverse component of the momentum transfer. The relation is only valid in the perturbative regime and for the case of small scattering angles, i.e. where the momentum transfer in longitudinal direction is independent from the projectile scattering angle. On this formal ground one sees the possible difference of projectiles with different velocities. The longitudinal momentum transfer differs for both systems: for the present case with $E_2 = 6.5$ eV it takes the value of $q^\parallel \approx 0.02$ a.u. for ion impact, which is close to zero. For electron impact with 1 keV the longitudinal minimum momentum transfer is $q^\parallel \approx 0.13$ a.u.

The comparison of the three-dimensional cross section for both projectiles is shown in Fig. 4.4. Integration intervals of the present electron impact data are $\Delta|q| = \pm 0.2$ and $\Delta E_2 = \pm 1$ eV. As mentioned earlier, the momentum transfer is not perpendicular to the incoming projectile axis for the

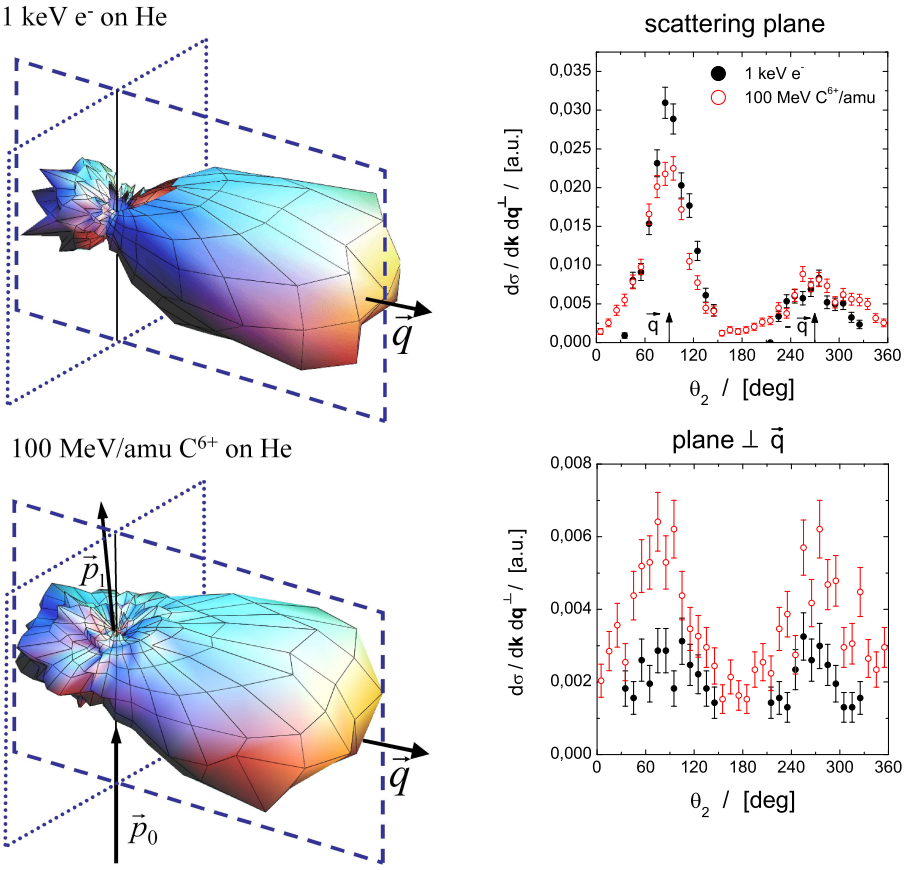

Figure 4.4: Comparison of three-dimensional images of electron emission from single ionization of He by 1 keV electrons (top left) and 100 MeV/u C^{6+} ions from [SMF+03] (bottom left) on the same absolute scale. The momentum transfer $|q| = 0.75$ a.u. and the emitted electron energy $E_2 = 6.5$ eV are fixed to the same value. $\vec{p_0}$, $\vec{p_1}$: incoming and scattered projectile momentum. Two cuts are applied to the three-dimensional cross sections, one in the scattering plane and another in the plane perpendicular to $\vec{q}$, which are indicated by dashed and dotted lines, respectively. The resulting FDCS are given in the right column. Top right : scattering plane; bottom right : perpendicular plane.

electron projectiles. For electron impact, due to the lower v_P the momentum transfer $\vec{q}$ is kinematically shifted forward by 11° with respect to $\vec{q}$ in the ion collision, which is almost perpendicular to the incoming beam. In order to simplify the comparison, this difference is removed in the figures by rotating the electron impact cross section correspondingly, such that $\vec{q}$ is perpendicular to the rotated z-axis. Both emission patterns show a very similar double-lobe structure. Again the out-of-plane emission is far less pronounced than in the ion impact case. Another point which needs to be addressed is the effect of the experimental resolution. All cross sections obtained by electron impact were evaluated using two different methods of inferring the momentum transfer $\vec{q}$. In the (e,2e) data shown so far, the transverse momentum transfer was calculated from the scattered projectile, i.e. $\mathbf{q} = -\vec{p_1}^{\perp}$. To check the effect of the poor momentum resolution for the recoil ion, the FDCS was generated calculating the momentum transfer from the target fragments $\vec{q} = \vec{p_2} + \vec{p_{ion}}$. This did not show any effect on the shape nor absolute magnitude of the cross sections for momentum transfers larger than 0.5 a.u (for details see also appendix, sec. A.1.2).

In the scattering plane the cross sections are very similar in shape and magnitude for both projectiles, which are presented on the same absolute scale. This indicates that second and higher order contributions are small in this plane and a first order description should work well, even for fully differential cross sections which are very sensitive to the collision dynamics. At this point one should recall, that the energy of the projectile in the ion collision amounts 1.2 GeV and is by a factor 10^6 larger compared to 1 keV of the projectile electron!

However, there are clearly observable differences in the scattering plane which may have following two reasons:

- The magnitudes of the binary peaks differ by about 30%. This can be caused by the remaining small difference of the perturbation η for both collision systems ($\eta_e/\eta_{ion} \approx 1.17$). In the first order the cross section scales with η^2, which leads to an effect of about 30% and has to be kept in mind when comparing the heights of the binary (recoil) peak for the different projectiles.

- The ratio of binary and recoil peak is different for both collision systems, which may be due to the long range PCI between the projectile and the target. This is a well known behavior of the PCI, which changes with the sign of the projectile [VNU03]. In theoretical calculations treating higher order PCI the height of the binary peak with respect to the FBA increases for positively charge projectiles and decreases for projectiles with negative charge. Similar effects are observed for the recoil peak.

For a comparison with the ion collision, the second cut in the image

obtained in electron impact is now applied *perpendicular to the momentum transfer* rather than in the perpendicular plane, since the momentum transfer defines the 'quantal' axis. For both projectiles the cross section shows the oscillating feature with peaks appearing near the angles 90° and 270°. As already visible in the 3D plots, the maxima are significantly higher for ion impact compared to electron impact. This is not only a clear indication of a higher order process, but it allows to assign the out-of-plane contribution to a charge-dependent term within a perturbative treatment. The significant difference in absolute magnitude of the FDCS features in the plane perpendicular to $\vec{q}$ between electron and ion impact can be only due to the projectile charge-sign dependent $(Z_P/v_P)^3$ term (or any higher odd order) in the perturbation series, since both cases differ in the sign of Z_P/v_P. Accordingly, the contribution in this emission plane originates from the interference between different orders of the projectile-target interaction. To support this statement the cross sections for electron impact are compared with second Born calculations, where the charge sensitivity of the cross section should be reproduced.

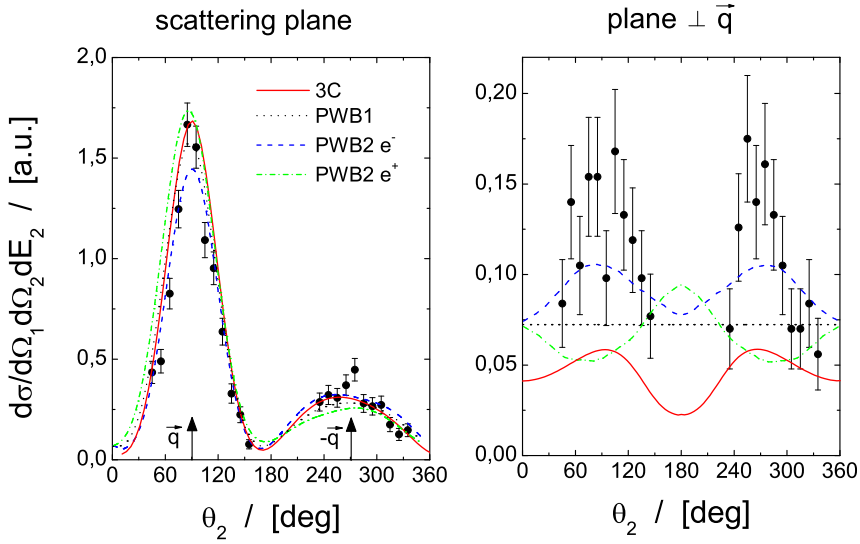

Figure 4.5: The FDCS for single ionization by electron impact in the scattering plane (left) and the plane perpendicular to $\vec{q}$ in comparison with a first order and second-order Plane Wave Born calculation. Theoretical curves: — 3C; ··· PWB1; - - - PWB2 for electron impact; −·− PWB2 for positron impact. Kinematical parameters as for in Fig. 4.4.

A second Born calculation is shown for electrons and positrons in Fig. 4.5

together with the first Born result. The calculation describes the incoming and outgoing projectile by plane waves, and is therefore labeled PWB1 and PWB2 respectively. Already in the scattering plane the discussed charge-sign sensitivity of the ratio of binary and recoil peak together with a small shift of the peak positions is observed. Interestingly, the agreement between the (e,2e) data and the calculation gets worse upon inclusion of the second Born term. The reason may be that the scattered projectile is represented by a plane wave and that the post-collision interaction is only included by the second-order amplitude. This may not be sufficient to describe the long-range PCI, where the 3C calculation seems to be more powerful since it is in good agreement with the experiment. For better agreement higher orders would have to included correctly, for example by representing the projectile by a distorted wave.

As expected, in the plane perpendicular to $\vec{q}$ the PWB1 calculation gives almost a constant value, since the first order cross section has to be isotropic with respect to the momentum transfer direction which is in accordance with the symmetry. The PWB2 calculation for electron impact exhibits the two peaks in the emission pattern and shows reasonable agreement. When changing the charge sign in the PWB2 calculation, the cross section maxima change into minima. Hence the calculation predicts just the opposite behavior in the plane perpendicular to $\vec{q}$ compared to the observation in the ion impact experiment. The out-of-plane emission in electron impact was correctly attributed to the charge-sensitive interference term between the first and second Born amplitude. The remaining discrepancy between data and the PWB2 calculation is probably due to the same reasons as in the scattering plane, namely the missing treatment of the long range interaction.

As a further comparison, the 3C calculation is shown as well in the plane perpendicular to the momentum transfer $\vec{q}$. The calculation exhibits a clear breaking of the symmetry with respect to the momentum transfer and shows two peaks at the same position as in the experimental data. However, the magnitude is by a factor three to small. In order to account for the experimental finite angular intergration range of $\pm 10^\circ$ for electron momenta out of the emission plane, the theoretical curves were convoluted. This did not show any significant effect.

4.1.3 (e,2e) at 102 eV Impact Energy

In addition to the measurements at 1 keV impact energy, a second (e,2e) measurement was performed at 102 eV, corresponding a projectile velocity of $v_P = 2.74$ a.u. The out-of-plane contributions observed in 1 keV electron impact should become stronger at reduced projectile velocity, because higher order effects are of increasing importance. This can be easily seen in the perturbation expansion (eq. (2.8)), where higher order terms are no longer negligible at larger perturbation. Besides, lower impact energies are more

in favor for 'exact' formalisms like the Convergent Close Coupling which uses a partial wave expansion, and at lower impact energies only smaller angular momenta contribute to the cross section. At higher impact energies, and thus shorter wavelengths, a larger number of partial waves has to be included.

A sophisticated 'approximative' model applicable at 102 eV impact energy is the second Born distorted wave calculation. The advantage of the perturbative treatment is, that the significance of particular amplitudes, and hence different dynamical mechanisms, can be examined.

Regarding the experiment at the chosen impact energy of $E_0 = 102$ eV, the scattered projectile is slow enough, in order to resolve its longitudinal momentum. Therefore the full kinematical information of both final state electrons is available, which enables to determine the total energy-loss or alternatively the Q-value of the reaction[1]. By the known energy loss, which can be determined for each recorded triple coincidence, processes leaving the He^+ ion in different states with principal quantum number $n = 1$, $n = 2$ or $n \geq 3$ can be identified. In the previous ion impact and 1 keV electron-impact FDCS measurements, where the momentum of scattered projectile remains (partly) undetected, the final state of the ion remained unresolved. For all electrons, including the scattered ones, the transversal resolution is estimated to $\Delta p^{\perp} \approx 0.1$ a.u and $\Delta\phi \approx 10°$. The longitudinal resolution for the slow ionized electrons is $\Delta p^{||} \approx 0.02$ a.u., while for the scattered projectiles at $E_0 = 102$ eV the estimated resolution is $\Delta p^{||} \leq 0.08$ a.u.

Regarding the normalization, the absolute scale of the cross section cannot be determined by the procedure used at high impact energies. One reason is the smallest accessible momentum transfer $q_{min} = \Delta E / v_P$, resulting from the energy transfered during the reaction, which becomes larger at smaller projectile velocities. In combination with increased higher order effects leading to strong shifts of the binary and recoil lobe, this makes the extrapolation used at 1 keV impact energy unreliable. However, since the data is recorded in one 'run' of a measurement, all scattering geometries are internormalized. Fortunately, the present reaction microscope data includes the geometry measured by Röder et al. at 100 eV impact energy using the conventional (e,2e) technique and our FDCS can be scaled to the absolute cross section published in [BF96b]. Once the normalization factor has been fixed, all the cross sections of all other geometries are internormalized across all recorded scattering angles and all ejected electron energies.

3D Images of the Cross Section

The absolute FDCS are presented as three dimensional cross sections in Fig. 4.6 for three different scattering angles $\theta_1 = (10 \pm 1)°$, $\theta_1 = (15 \pm 1)°$,

[1] Since the (e,2e) measurement at 102 eV served as an example in the section describing the apparatus, the reader is referred to chapter 3.

and $\theta_1 = (20 \pm 2)^\circ$ and an energy of the ejected electron of $E_2 = (10 \pm 1)$ eV. The cross section shows again the dipolar structure, however significant differences compared to the cross section at high impact energies appear.

- Both lobes are tilted away from the direction of the scattered projectile, which can be attributed to the post-collision interaction between the scattered projectile and the ejected electron and the residual ion. The scattered projectile is much slower than in the 1 keV case, and therefore the tilt is much stronger.

- The recoil lobe is quite large, and at small momentum transfers it dominates the cross section.

- Similarly to high impact energies, the relative intensity of the out-of-plane contributions increases at larger momentum transfer forming a 'bridge' between the binary and recoil lobe.

Hence, the underlying dynamics leading to the FDCS is more complicated than in the high energy case, where the first Born limit provides an intuitive frame for the collisions. At low impact energies, the three-body nature of the collision unfolds and the resulting complexity of the system cannot be reproduced by first order calculations. A quantitative comparison with theoretical calculations is performed for cuts in the scattering and the perpendicular plane.

Comparison with Theory

With the dynamics getting increasingly complex, the requirements to the theoretical description of the process are far higher than in the perturbative regime. The interaction between all three collision partners - the correlated dynamics - should be incorporated in theory. At this low impact energy, there is no sense in comparing with the first Born approximation, since it no longer serves as an adequate description. The 3C calculation shown for 1 keV impact energy, incorporates the correlation between all three particles and can also be applied at this low energy. Furthermore, the data are compared with a state-of-the-art second Born distorted wave calculation [CMWW04, CM05], where the out-of-plane geometry apparently serves as valuable testing ground for various details of the calculation. Finally, in comparison with the Convergent Close Coupling, claiming to solve the three-body system 'exactly', the cross section critically tests the description treating the ionization process as an effective three-body system. The three theoretical models are compared for two different electron energies, namely $E_2 = 10$ eV and $E_2 = 5$ eV (Fig. 4.7 and 4.8).

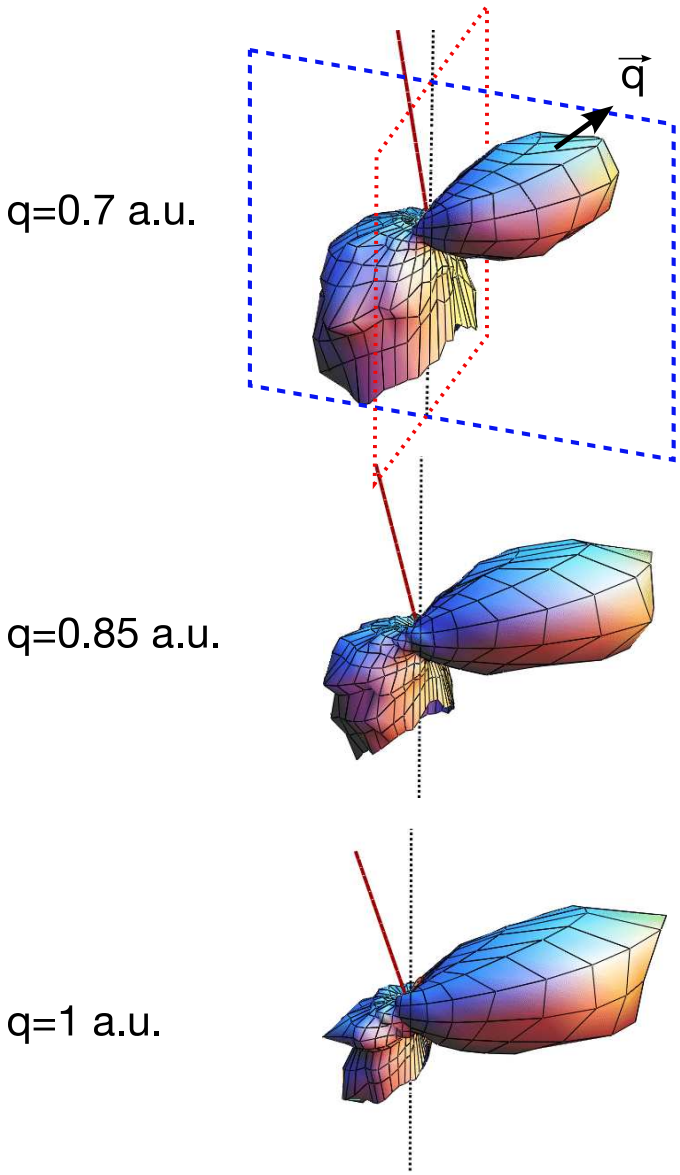

Figure 4.6: Three dimensional FDCS for single ionization by 102 eV electrons showing the emission of electrons with $E_2 = 10$ eV. The cross sections are presented for three different momentum transfers $|q| = 0.7$ a.u. (top), 0.85 a.u. (middle) and 1 a.u. (bottom).

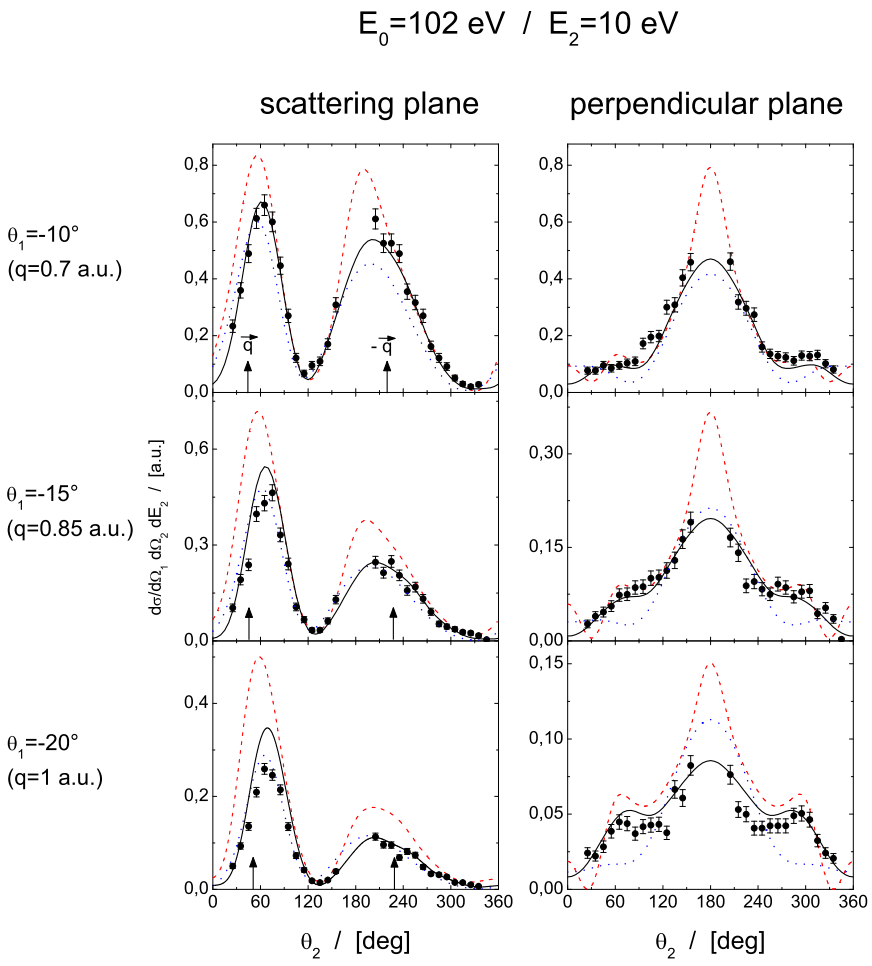

Figure 4.7: Cuts through the three dimensional cross sections from Fig. 4.6. The FDCS (in atomic units) are plotted as a function of the angle of the emitted electron θ_2 with respect to the incoming projectile beam direction, for a fixed scattering angle θ_1 and a fixed emitted electron energy $E_2 = 10\,eV$. FDCS in the scattering plane (left), in the perpendicular plane (right) Theoretical curves: — CCC; - - -DWB2; ⋯ 3C

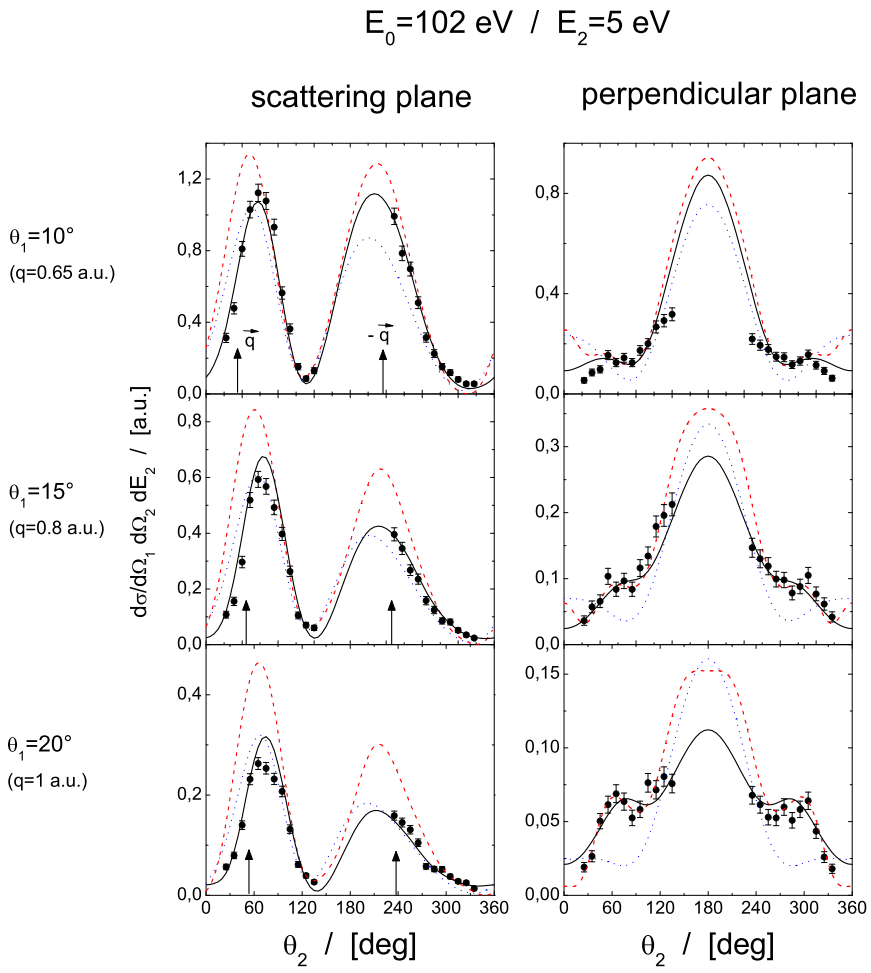

Figure 4.8: The same as in Fig. 4.7 but for $E_2 = 5\,\mathrm{eV}$.

3C In the scattering plane, the 3C calculation shows generally shows good agreement on the absolute scale. Slight discrepancies with respect to the shape and the position of the binary and recoil peak exist. The reason is due to the approximative treatment of the correlated motion of the three particles, which is apparently appropriate at high-impact energies and for the scattering plane, only [FA91, BBB90]. An attempt to improve the approximation is achieved by including the so-called dynamical screening [BB94], which additionally introduces mutual screening effects in the description of the three-body dynamics. However, the so-called DS3C treatment does not improve the agreement with the data (not shown in the figure). In the perpendicular plane the situation is similar as for 1 keV impact energy. At around 70° and 290° the experimental cross section again shows enhanced emission which becomes more pronounced at higher momentum transfer. The 3C calculation again fails to reproduce the experimental data.

DWB2 A different calculation on-hand is the second-order distorted wave calculation reported by Chen et al. [CM05, CMWW04]. With respect to the post-collision interaction, the model is superior to the second-order plane wave calculation presented at 1 keV impact energy. Instead of representing the incoming and projectile as plane waves, thus neglecting any interaction with any other charged particles, the incoming projectile and the two outgoing electrons are represented by distorted waves. The distortion potential accounts for the interaction of the incoming projectile with the atom. The distortion for the outgoing final state electrons reflects the interaction with the residual target. The better treatment of the interaction of the incoming and outgoing projectile with the target-ion, accounts for increasing correlation between the collision partners at the reduced velocity of the projectile electron at 102 eV. Due to the asymmetric energy of the electrons, electron exchange-effects are neglected in the calculation. In their recent work, Chen et al. present calculations, where the second-order amplitude is evaluated without approximations, apart from numerical ones. One widely applied approximation for asymmetric kinematics is the so-called closure approximation (see sec. 2.2.2), which can be tested now for the electron impact ionization of helium.

The comparison with the data in the scattering plane shows a trend to better agreement at low scattering angles. The binary peak is overestimated for all presented geometries. For the recoil peak there is good agreement for the smallest scattering angle 10° which gets worse for larger scattering angles. It is well known that the second-order description reaches its limits at impact energies lower than 150 eV [CMWW04], where the authors claim that third and higher orders may become important. Another point which may lead to the large discrepancies of the binary peak is the lacking description of the post-collision interaction of the projectile with the ejected

electron. Interestingly, the agreement is very good in the perpendicular plane. Apparently for this geometry the DWB2 approximation is sufficient to describe a large part of the dynamics.

With respect to the second-order calculation at 1 keV impact energy using pane waves, the calculation presented for 102 eV projectile energy marks an improvement. In the perpendicular plane the data is reproduced nearly perfectly for all momentum transfers and for both ejected-electron energies. For a selected scattering geometry, a first order distorted wave is compared with the second-order calculation for the non-coplanar cut (Fig. 4.9). It shows a strong difference between the two calculations, again confirming the origin of the pronounced out-of-plane structures. A very interesting aspect is the high sensitivity of the non-coplanar geometry: apparently the very common closure approximation usually made in the evaluation of the second-order amplitude, is not valid in the out-of-plane geometry [CM05, Che06]. So far, any possible implications for calculations at high impact energy and with positive projectiles still have to be analyzed on theoretical side.

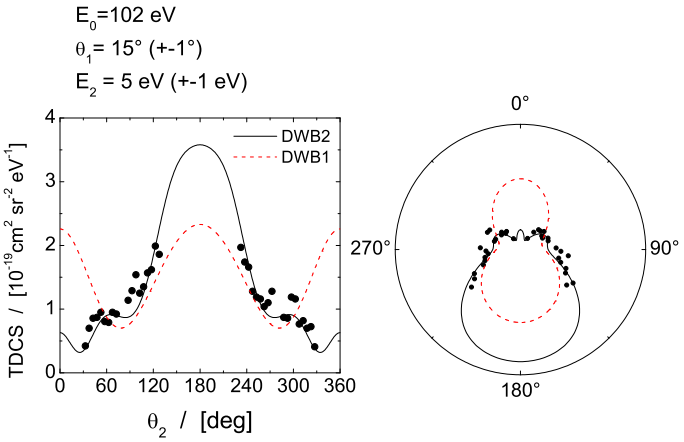

Figure 4.9: The fully differential cross section in the perpendicular plane shows the large difference between the first and second Born distorted wave calculations (dashed and solid curves).

CCC Until now, the CCC calculations describing single ionization of helium were performed within the 'frozen-core' model, i.e. the remaining bound electron does not take actively part in the collision dynamics. In other words, throughout the collision process the 'passive' electron remains in its assigned ground state. Even for very low impact energies approaching the ionization threshold and where the coupling between projectile and target becomes stronger, the 'frozen-core' approximation leads to good agreement

[SBFB05]. For the cuts shown in Fig. 4.7 and Fig. 4.8, very good agreement is observed between the CCC calculations and the experimental data. Only at 10 eV and $\theta_1 = 20°$ the binary peak is overestimated.

The comparison of the three dimensional images of the 3C and the CCC calculation clearly shows the differences in the emission pattern, the CCC calculation exhibiting the 'ring'-like structure centered around the incoming projectile axis.

4.1.4 Concluding Remarks

The unsolved situation in the single ionization of helium by fast ions reported in [SMF+03], where the disagreement with all theoretical models remains an urgent question, was addressed by measuring the same process using 1 keV electrons as projectiles. For the first time, the experimental FDCS of an ionizing collision in the perturbative regime can be compared for projectiles of different charge sign but at the same strength of the perturbation $|Z_P/v_P|$. Within the first order treatment, the cross section should be essentially identical. On one hand the cross sections at this particular momentum transfer confirm this prediction in the scattering plane. On the other hand second order effects are clearly visible in the angular electron-emission perpendicular to the momentum transfer, which strongly differs for electrons and ions. This encourages to assign the observed difference, which is particularly pronounced in the non-coplanar geometry, to the interference between different orders of the perturbation series which are charge-sign dependent.

For electron impact a second Born treatment qualitatively explains the enhanced emission of electrons perpendicular to the momentum transfer. Therefore the data confirm all predictions of the perturbative models for negatively charged projectiles, which on the other hand lead to strong disagreement for single ionization with positively charged ions.

Before implications can be extracted from the new results of electron impact ionization, they should be viewed in the context of the discussion of the three-dimensional cross sections for ion impact showing the strong discrepancies by Schulz et al. [SMF+03]. The authors discuss a possible mechanism, which is made responsible for the enhanced out-of-plane emission of slow electrons. They propose a double-scattering mechanism, where in the first step the electron is ionized in a binary collision. In a second step, the projectile scatters elastically of the nucleus and transfers additional momentum to the nucleus. Since the energy transfer should be vanishingly small, the additional scattering of the projectile only changes the direction of the projectile, such that the ejected electron is finally emitted outside the scattering plane. Such a mechanism would also explain the ring-like shape of the out-of-plane emission (Fig. 2.7). Such a two-step mechanism is included in the second-Born amplitude, which leads to agreement for electron impact.

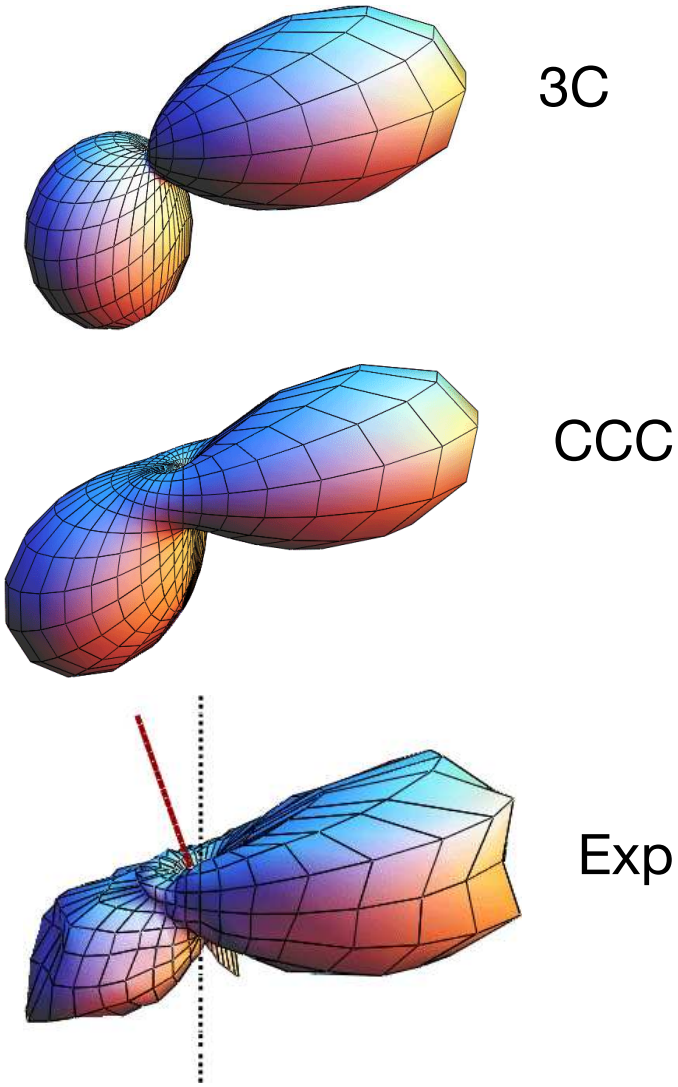

Figure 4.10: Comparison of three-dimensional images of the cross section for $E_0 = 102\,\text{eV}$ impact energy, a scattering angle of $\theta_1 = 20°$ and an energy of $E_2 = 5\,\text{eV}$ of the ejected electron. Top: 3C calculation, Middle: CCC, Bottom: Experiment.

Several other calculations (Eikonal- and Glauber-approximations) show the same trend [VNU03]. The failure of the 3C method may result from the deficiency in describing situations, in which all three collision partners are close. For the almost identical distorted-wave model applied in ion impact, similar arguments are presented, and it is stated, that the out-of-plane contributions result from collisions in which the scattered projectile comes close to the nucleus [MFF$^+$03].

However, all approximative models, like the second Born treatment, still fail for ion impact, although they should be able to describe such close collisions, which is indicated by the correct predictions for the electron impact results. Even though it seems, that the two collisions with 1 keV electron impact and 100 MeV/u C^{6+} ion impact can be directly compared with each other, there is still the difference of the minimal momentum transfer q_{min}, which leads to differing coefficients in the perturbative expansion (2.8). To provide an ultimate experimental test, it would be necessary to use antiparticles (either positrons or antiprotons), since only here the charge sign can be changed without changing q_{min}.

Another possible reason for the failure of the treatments for positive projectiles may be due to the challenging treatment of the ground state of the helium atom. After all, the electron remaining in the ground state of the residual ion may play an important role in the two step scattering mechanism: if the projectile elastically scatters of the nucleus in a second step, a proper description of the bound electron may be important. On the experimental side, this could be tested by performing experiments studying ion impact single ionization of atomic hydrogen, which is a true three-body system. Regarding electron impact, the new refinements of the reaction microscope allow to gain three-dimensional cross sections for practically all gaseous targets. In that sense it would be interesting to check the sensitivity of the non-coplanar low-energy electron emission with respect to different target-atoms. Another interesting question is, whether the out-of-plane scattering geometry can serve as a sensitive and interesting probe for electron correlation in atoms or molecules [vBWC$^+$06].

In conclusion, using the 'advanced' reaction microscope, three dimensional images of the fully differential cross section could be measured for electron impact at low momentum and energy transfer. Two different projectile energies were considered, the impact energy of 1 keV representing the regime where reasonable agreement is reached within a first Born description. The second impact energy at 102 eV, which is at the maximum of the total ionization cross section, represents the intermediate regime where the three-body nature of the system unfolds. Since the majority of the collisions occur at asymmetric geometry, the obtained data provide a comprehensive benchmark for theories treating the single ionization process in particular and of the dynamical three-body problem in general.

The non-coplanar scattering geometry reveals to be very sensitive to dif-

ferent descriptions of the few-body process. More importantly, the benchmarks are provided for a large fraction of momentum space where most ionizing collisions occur. In case of full agreement, (e,2e) on one and two electron systems can be regarded as completely understood.

4.2 Ionization-Excitation at $E_0 = 105\,\mathbf{eV}$

In the single-ionization process presented in the previous chapter, the electron remaining in the bound state of the residual ion plays a mere spectator role. In most cases, the bound electron merely exercises a screening of the ion for the two outgoing electrons in the final state. The ejection of an electron with a simultaneous excitation of the remaining bound electron into n≥2 states of the residual ion involves in total four particles[2]. This process can be seen as a double-excitation of the He-atom by electron impact, and therefore represents a system where the correlation between both target electrons and the projectile becomes important. Hence it presents a great challenge for theory, and at a same time an ideal testing ground for further development of the frameworks describing single ionization to $He^+(n = 1)$.

The ionization and excitation of the helium atom

$$e^- + \mathrm{He}(^1S) \rightarrow e^- + e^- + \mathrm{He}^+(nl), \tag{4.4}$$

where the residual ion is in the excited state with principal quantum number $n \geq 2$ and represents the most fundamental system for such reactions. Practically all existing electron impact studies concentrate on the excitation into the $n = 2$, because here only s- and p-states exist. The higher lying levels include higher angular momenta and are closer to each other in energy, such that they are difficult to separate in the experiment. Furthermore the cross sections are considerably lower for the $n \geq 3$ states.

The process of ionization-excitation of He can be studied in various ways: first, just like for pure single ioniziation, the kinematical complete information in form of the triple differential cross section is gained in (e,2e)-type experiments detecting both emitted electrons. In such type of experiments the energetically degenerate sublevels of $n = 2$ states (2s and 2p) cannot be discriminated. A second class of experiments are (e,γe)-studies, where the photon which is emitted after decay of the ion from the He^+(2p) to the He^+(1s) state as well as one of the outgoing electrons is detected [HW96]. However, the full kinematics remains undetermined in such electron-photon coincidence studies. The reason, that the so-called 'quantum mechanically complete experiment' [BB99], where the outgoing electrons and the emitted photon are detected with angular resolution, has not yet been performed is due to the low coincidence rates. So far, the only reported (e,γ2e) experiment using a reaction microscope [SDH$^+$05] still lacked the angular resolved measurement of the photon[3].

The measurement of the fully differential cross section with a conventional (e,2e) spectrometer is a challenging task, since the cross sections for

[2] For the hydrogenlike He^+ here the internal states are described by the quantum numbers (n,l,m_l)

[3] Alternatively, the polarization can determined, instead of the angular emission pattern of the emitted photon.

ionization-excitation is by about two orders of magnitude lower than the mere ejection of an electron. The number of (e,2e) studies on helium, where the final ion is in the $n = 2$ state, is far less than in pure ionization, mainly given by the fact, that the cross section is low and thus accumulation times are long. There are generally two types of (e,2e) experiments: one type are those where the process is studied in 'impulsive' collisions, i.e. at high impact energy and at symmetric energies of the two outgoing electron similar to the studies used as momentum spectroscopy of the bound electron. These experiments are sensitive to the description of the correlated wavefunction of the target He-atom [CMSW84, WKT$^+$05]. The second type are those dedicated to study the dynamics of the process at low energy and momentum transfer, just like the (e,2e) studies in the previous section [SAC90, DLBD$^+$92, ACM$^+$98, RRP$^+$00, DC00].

In the previous chapter, the single ionization leaving the residual ion in the ground state was studied with the advanced reaction microscope. The process was identified by determining the energy-loss Q of the projectile by filtering ionization events with $Q = 24.6\,\mathrm{eV}$, which is the ionization potential for the ejection of one electron. This could only be achieved with new refinements of the reaction microscope, which allows to determine Q from the summed energy of the two outgoing electrons. Apart from this simple reaction, processes where the residual ion is in an excited state can be identified, in which the projectile loses additional energy and Q is substantially larger in these reactions. As there is very good agreement between theory and experiment for three-body processes like single ionization of helium, dedicated measurements where performed at an impact energy of $E_0 = 105\,\mathrm{eV}$. A great benefit of the reaction microscope is, that it can cover a wide range of scattering geometries. Similar as in single ionization, only the asymmetric scattering geometry is considered, with one 'fast' electron identified as the scattered electron and one slow electron identified as the ejected electron.

Mechanisms for Ionization-Excitation

If the projectile is sufficiently fast, such that a perturbative treatment of the interaction with the target atom is justified, the process of ionization and excitation can be basically described within two mechanisms.

1. The projectile interacts subsequently with each of the two electrons, ejecting one and exciting the other for instance by the exchange of two virtual photons. Within the perturbative treatment such a mechanism will be described by the second Born amplitude and is also named the 'Two-Step' mechanism.

2. The projectile transfers energy and momentum to one of the electrons within a 'single-photon' interaction described by the first order Born amplitude. Through the electron-electron correlation of both bound

electrons, one electron is ejected, and the second dwells in the final excited state of the He^+-ion (so-called Shake-up). Alternatively, the projectile transfers momentum and energy to one of the electrons, which in turn inelastically excites the second bound electron in an 'internal' e^--He^+ collision.

The first order treatment critically depends on the description of the correlated initial target wavefunction and also on the description of the interaction of the outgoing electron and the excited electron bound in the ionic core [ACM+98]. In fact, the different calculations in literature 'converged' to similar results, such that is can be claimed that the first order Born amplitude can provide a basis for further theoretical developments [KBB99]. Compared to direct single ionization the fully differential cross section strongly depends on the details in the description of the transition amplitude. Here the recent approaches using 'pseudo'-states describing the continuum of the He^+ atom like 'Convergent Close Coupling' and R-matrix coupled channels calculations provide an accurate representation of the three-body subsystem, consisting of the ion, the bound and the ejected electron. However, even at the high impact energy of 5.5 keV, there is still disagreement between theory and experiment in the absolute FDCS. These discrepancies may due to following two reasons: (1) higher order contributions have to be taken into account, since they may contribute to the process even at high impact velocities. (2) The disagreement is due to interference with autoionizing resonances of doubly excited helium. These decay to an excited state He^+ under emission of a monoenergetic electron and the process cannot be distinguished from the direct ionization-excitation process. This leads to an interference between both pathways to the final state and can therefore effect the absolute magnitude as well as the shape of the angular emission pattern discussed in [FB01]. Because these autoionization resonances themselves establish an interesting topic, this phenomenon is highlighted in more detail in the following section.

Doubly Excited States of He

Doubly excited states of neutral helium were discovered in studies of inelastic electron collisions [SL64]. At specific energy-losses of the incoming electrons there is an increased probability for an inelastic collision. This indicates the existence of resonant channels. These resonances could be identified as autoionizing states, where the neutral helium is excited into a doubly-excited state He^{**} which decays within short time, by emission of one electron into the continuum and a transition of the second into a energetically lower bound state of the He^+-ion. The energy-levels of the doubly excited states are energetically in the continuum of the singly charged ion. They can be classified in a series of levels, which approach the exited states

of the He^+-ion as in Fig. 4.11a. The nomenclature which is often used, orients itself by the principle quantum number n of the excited He^+-ion to which the series of doubly excited states converges to. The notation from effective one-electron states cannot be applied for the doubly excited states, because of the strong electron correlation, by which the assignment of one-electron quantum numbers fails. In fact these states represent the paradigm of electron correlation in atoms, where the one-electron classification scheme of doubly excited states fails and a different scheme has to be found, which is still subject of actual research (for a review see [TRR00]).

Energetically, all doubly excited states can decay into the ground state of He^+. The lowest doubly excited states 2l2l' are energetically lower than the exited state of $He^+(n = 2)$ and therefore can only decay to $He^+(n = 1)$, and are said to be below the N=2 threshold (see Fig. 4.11a). However, the 3l3l' states below the N=3 threshold can decay into the $He^+(n = 2)$, and therefore these decay channels contribute to the ionization-excitation process. In terms of the transition amplitude T_{fi}, the direct path of ionization and excitation as well as the indirect path via the decaying doubly excited state to the same final state, can be expressed by two different amplitudes T_{fi}^{dir} and T_{fi}^{indir}, since these are two different processes. In the measured cross section the two indistinguishable paths interfere

$$\sigma(\mathrm{He}(1^1S) \rightarrow \mathrm{He}^+(n = 2)) \propto |T_{fi}|^2 = |T_{fi}^{dir} + T_{fi}^{indir}|^2 \qquad (4.5)$$

The energy profile, i.e. the cross section as a function of the ejected electron, around the resonances sensitively depends on the details (i.e. mean values and relative phases) of the direct amplitude describing the ionization-excitation process and the indirect amplitude which describes the decay of the doubly excited state. The resulting famous Fano-Profile is a characteristic consequence of quantum mechanical interference which is observed in many areas of physics. At the low impact energy of $E_0 = 105\,\mathrm{eV}$, however, the presence of the slow projectile electron is expected to influence the doubly excited states and hence the resonances. These effects have been studied for the 2l2l' resonances [BSKW97, SCB+97], where the so-called post-collision interaction (PCI) causes a shift of the resonance position and/or a change of the shape is expected. The influence of the scattered projectile is not easily seen, since by changing any of its kinematical parameters the change in the profile may be either due to the PCI or the change of the amplitude T_{fi}^{dir}.

4.2.1 Experimental Results

A typical energy-loss spectrum has already been presented in chapter 3 in Fig. 3.18. For the evaluation of cross sections, events were filtered, which have an energy sum corresponding to an energy-loss of $Q = 65.42\,\mathrm{eV}$ for ionization of one target electron and excitation of the remaining bound electron

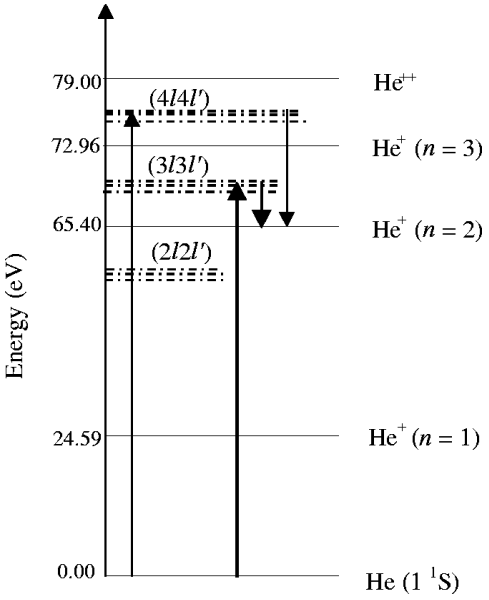

(a) Energy-levels of neutral and singly-charged helium. The arrows indicate the excitation from the neutral ground state to doubly-excited states, which subsequently decay into the levels of singly-charged He^+ (Adapted from [DC02]).

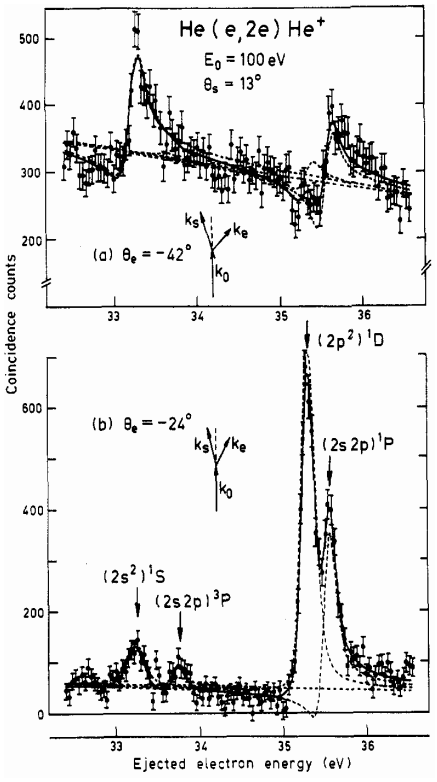

(b) Experimental energy profiles and the corresponding Fano-fits of the emitted electron after excitation of the 2l2l' autoionizing levels at a fixed scattering angle of the scattered projectile. The two profiles were recorded at two different angles of the emitted electron. (From [LW90])

Figure 4.11

to $n = 2$ state. Therefore processes into the s- and p-states are not resolved, which has to be kept in mind when comparing with theoretical calculations. For the ionization-excitation the projectile loses a large fraction of its kinetic energy due to the high inelasticity of the reaction. This means that for a given projectile energy, the scattered electron has a smaller velocity than in the case of single ionization. In the dedicated experiment this was considered and the electric extraction potential and the magnetic field were set to such values, that the scattered projectile is in between two 'wiggles' in order to achieve the best possible resolution for its transverse components. A great advantage of the reaction microscope is, that together with the ionization-excitation, also pure single ionization events are recorded. In the present experiment absolute excitation cross sections are obtained by scaling the FDCS for ionization into the ground state to a 3C-calculation for a chosen scattering geometry. From the previous chapter the absolute value of the calculations coincides for several theories and has been independently established in the experiment on single ionization at very similar impact energy (see sec. 4.1.3).

3D Images of the Cross Section

The fully differential cross section can be extracted just like in single ionization. In order to have a direct comparison, the three dimensional image is presented for an energy of the ejected energy of $E_2 = (10 \pm 2)\,\mathrm{eV}$ and a scattering angle of $\theta_1 = (20 \pm 2)^\circ$. The first apparent feature is the strong difference in the emission pattern compared to single ionization. Nevertheless, there is still a double lobe structure, with one lobe pointing roughly in the direction of $\vec{q}$, and a second pointing roughly in the opposite direction. For simplicity, the two lobes are called binary and recoil peak, even if the intuitive picture behind this nomenclature may not apply to the ionization-excitation process. The 3D-emission exhibits only a rudimentary binary peak whereas the recoil peak is the dominant feature (which makes the acceptance hole in the backward direction for electrons appear very large). Two qualitative arguments can be given for the difference of the characteristic binary-recoil emission with respect to pure single ionization.

- The angular emission measured in ionization-excitation contains contributions where the residual ion is in a 2s- or in a 2p-state. This is in contrast to pure single ionization, where the final ionic state is an s-state and hence the emission pattern originates from p-wave emission. For ionization-excitation into the 2p-state, the emitted electron exhibits s- and d-wave characteristics.

- In ionization-excitation multiple scattering plays an important role, and therefore it cannot be expected that the dipolar character 'survives' even when the description by a single virtual photon exchange

is applied.

At this low impact energy of $E_0 = 105\,eV$ additionally post-collision interaction effects should be strong, which additionally affects the emission pattern.

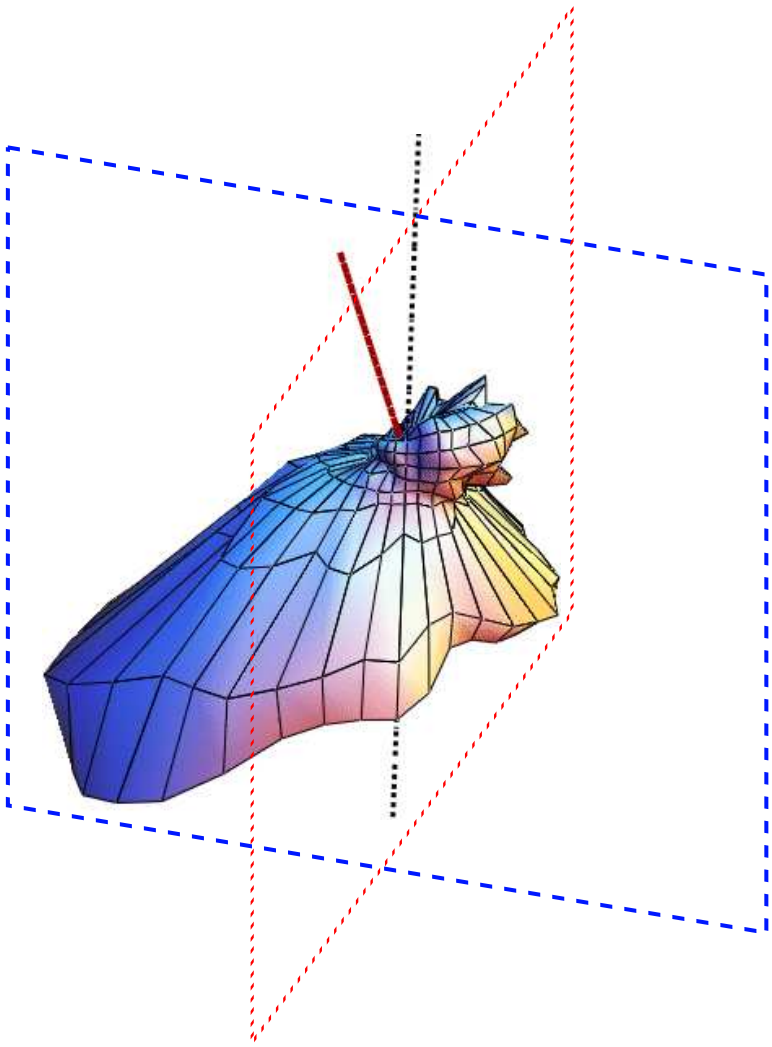

Figure 4.12: Three dimensional FDCS for single ionization by 102 eV electrons showing the emission of electrons with E_2=10 eV. The cross sections is presented for a scattering angle of $\theta_1 = 20°$ which corresponds to a momentum transfer of $|q| = 1.4$ a.u.

The cuts in Fig. 4.13 reveal more details and are shown for two more scattering angles $\theta_1 = (10 \pm 2)°$ and $\theta_1 = (15 \pm 2)°$. The cross sections are integrated over angles $\pm 10°$ above and below the cutting plane. In the scattering plane for instance, it can be seen that the binary and recoil

'peaks' are partly merged. The binary region seems to have some double-peak structure, especially at the projectile scattering angle of $\theta_1 = 20°$. In the perpendicular plane, the situation is very similar to the one found in pure single ionization. Again the recoil peak reaches into the perpendicular plane and is therefore the dominant feature. Side-lobes are observed at around $\theta_2 = 60°$ and $\theta_2 = 300°$, just like in pure single ionization. Without comparison with a calculation, it is however difficult to make any statements about the importance of different mechanisms.

Autoionization Resonances

As already discussed earlier, the presence of autoionizing resonances has to be accounted for. When the residual ion is excited into the $n = 2$ state, the 3l3l' resonances have been studied in an electron photon coincidence experiment [DC02]. However, their appearance was not yet investigated in an (e,2e) experiment, but is debated to influence the absolute magnitude of the cross section [FB01]. This issue becomes important, because most of the available experimental fully differential cross sections have been taken at energies of the ejected electron, where the resonances may contribute. This in turn could explain discrepancies with theory, where often disagreement is found with respect to the absolute scale of the cross section.

In the reaction microscope experiments, the 3l3l' resonances become clearly visible in the momentum spectra of the emitted slow electron. Here the doubly excited state decays into the $He^+(n = 2)$ state under emission of a monoenergetic electron. In Fig. 4.14 the distribution of electron momenta as a function of $p^{\parallel}$ and $p^{\perp}$ is shown for emission in the scattering and the perpendicular plane. The displayed cross section is integrated over all scattering angles of the projectile ($10° \leq \theta_1 \leq 35°$). A resonant emission of an electron should enhance the cross section at a given resonance energy, which should result in a circular ridge of the cross section in the $p^{\parallel}$-$p^{\perp}$-plane, since E=1/2$((p^{\parallel})^2 + (p^{\perp})^2)$. Although the enhancement is weak, it can be seen at forward emission angles of the emitted electron in the distributions shown in Fig. 4.14. For these emission angles the direct process is weak. To support this statement, two circles at the two different resonance energies have been inserted into the distribution, which is displayed in the same spectrum on the right hand side of Fig. 4.14.

In a high resolution measurement using an electrostatic electron analyzer, the positions and line-shapes of the 3l3l' resonances were studied by Brotton et al. [BCC+97]. In their experiment the non-coincident rate of scattered electrons is recorded as a function of the energy-loss of the incoming projectile. The excitation of doubly-excited states of neutral helium appears at the resonance positions corresponding the specific energy needed to excite the state from the ground state E_{exc}. The profile is shown in Fig. 4.15, which shows a rich structure in a small energy range of less than 2 eV. In this

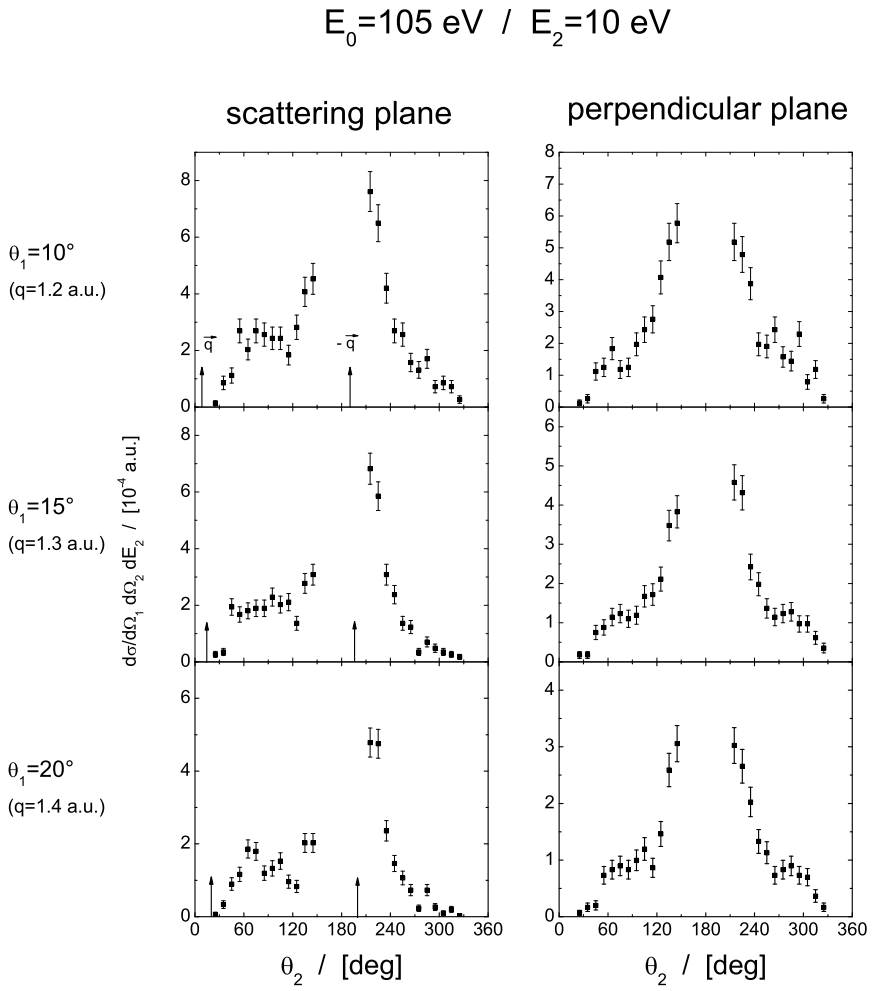

Figure 4.13: The FDCS (in atomic units) is plotted as a function of the angle of the emitted electron θ_2 with respect to the incoming projectile beam direction, for a fixed scattering angle θ_1 and a fixed emitted electron energy $E_2 = 10\,\text{eV}$. The cuts represent the cross section in the scattering plane (left) and in the perpendicular plane (right). The arrows in the scattering plane indicate the direction of the momentum transfer as well as the inverse direction.

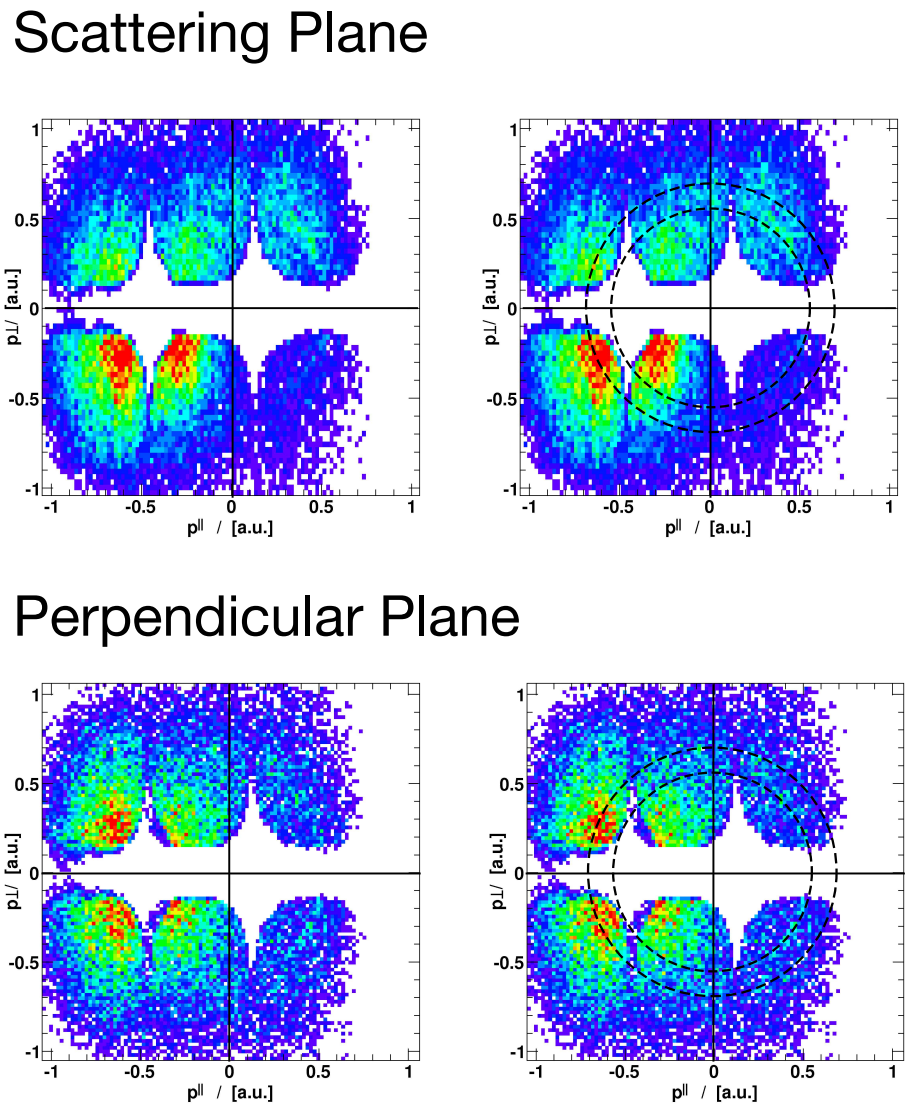

Figure 4.14: The electron momentum distribution of the ejected 'slow' electron as a function of $p^{\parallel}$ and $p_{\perp}$ in the scattering plane (top row) and in the perpendicular plane (bottom row). In order to make the dominant resonances visible, the spectra are shown twice, where on the right column the two strongest resonance positions $E = 4.2\,\mathrm{eV}$ and $E = 6.1\,\mathrm{eV}$ are indicated by two circles.

energy range there are in total 13 resonances, where the calculated width varies from 20 meV to 180 meV (see [BCC$^+$97] and the references therein). The situation is further complicated through the interference with the direct ionization-excitation and the peak positions and line shapes strongly depend on the impact energy and the angle of the scattered projectile. Luckily, the energy profile was measured under very similar conditions as in the present experiment, at similar impact energy and scattering angle of the projectile ($E_0 = 90\,eV$, $\theta_1 = 20°$).

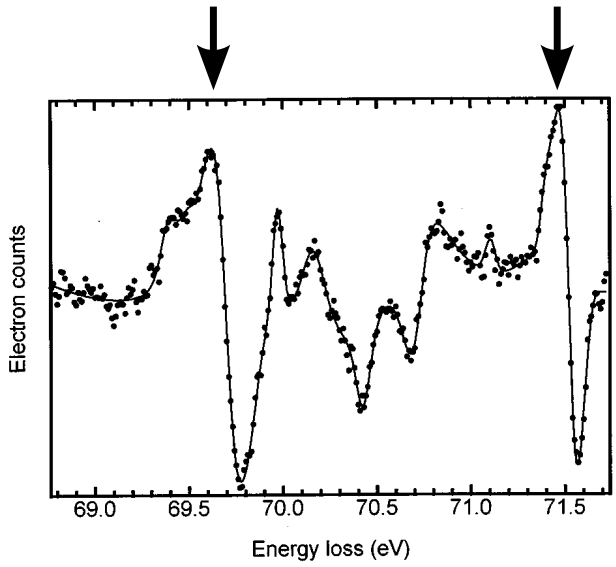

Figure 4.15: High resolution energy-scan over the 3l3l' resonances for a residual energy of 20 eV and a scattering angle of 20° of the analyzed outgoing electron. The solid line represents a fit. The arrows denote the energies, which correspond to the circles drawn in the momentum distribution of Fig. 4.14. (From [BCC$^+$97])

In order to be able to compare the profile in Fig. 4.15 with the reaction microscope measurement, both representations have to be brought to the same energy scale. The energy E_2 of the low energy electron emitted after decay of the doubly excited state, can be linked to the excitation energy E_{exc} (dubbed energy loss in Fig. 4.15) by $E_2 = E_{exc} - Q$, where Q is the total Q-value of the ionization-excitation process leaving the He^+-ion in the $n = 2$ state. Here the precise value is $Q = 65.42\,eV$. The two distinct peaks at an energy loss of $E_{exc} = 69.6\,eV$ and $E_{exc} = 71.5\,eV$ would then correspond to an energy of $E_2 = 4.2\,eV$ and $E_2 = 6.1\,eV$ of the ejected electron in the present analysis.

For the reaction microscope measurement the energy resolution for the slow emitted electron is estimated to be $\Delta E_2 \approx 0.5\,eV$. Therefore the details

of the energy profile cannot be resolved, however the two distinct peaks in Fig. 4.15 measured with high resolution seem to be reflected in the emission spectrum of the ejected electron of Fig. 4.14. The circles in the figure correspond to an energy $E_2 = 4.2\,\mathrm{eV}$ and $E_2 = 6.1\,\mathrm{eV}$, and hence the observed enhancement coincides with the two peaks observed in the high-resolution measurement shown in Fig. 4.15. It should be noted, that for the FDCS at $\mathrm{E}_2 = 10\,\mathrm{eV}$ the 4l4l' resonances should contribute as well.

4.2.2 Concluding Remarks

In conclusion, the fully differential cross section for ionization into $\mathrm{He}^+(n = 2)$ states has been obtained on an absolute scale for a wide range of scattering angles ($10^\circ \leq \theta_1 \leq 30^\circ$) and energies of the ejected electron ($4\,\mathrm{eV} \leq E_2 \leq 10\,\mathrm{eV}$). A small selection of cross sections was presented at 10 eV ejection energy. So far, there are no reported FDCS at the low impact energy of $E_0 = 105\,\mathrm{eV}$ and thus they provide benchmarks for the treatment of the dynamical four-body system. Theoretical calculations so far do not exist for this kinematics. Compared to double ionization, the ionization-excitation represents a system with a reduced complexity of the final state, with only three particles in the continuum. Hence, this process forms the ideal starting point for the further development of existing three-body descriptions. In contrast to all other existing data, the emission pattern over the whole geometry of the ejected electron has been recorded, which is gives more information than coplanar measurements as it has been revealed for pure single ionization. In this respect it will be interesting to compare with the perturbative treatments, like second-Born distorted wave methods, and critically test the underlying approximations in the evaluation of the second-order amplitude (e.g. closure). Encouraging progress has been recently achieved by the Convergent Close Coupling [PNB$^+$04] and also by the Exterior Complex Scaling (ECS) [HMR05a, HMR05b] models.

The autoionization resonances from the 3l3l' states could be observed over the full angular range of the emitted electron. A reaction microscope measurement shows great potential in particular since it provides essentially background-free data. The interference between direct ionization-excitation and the indirect channel via the excitation of the autoionizing doubly excited state allows to gain a unique insight into the relative phases and magnitudes of the amplitudes by analyzing the energy profile and angular distribution of the ejected electron [BMC96]. With respect to the presented data, the resolution and the statistics can be improved, such that a better quality can be expected in future. The doubly excited states are far more complex in electron impact compared to photoionization experiments, since electron projectiles can induce non-dipole transitions.

4.3 Double Ionization at $E_0 = 105\,\mathbf{eV}$

In contrast to single ionization, the double ionization of helium does not manifest a process, which is of major importance for applications, because the cross section is typically small. Comparing the total cross sections of single and double ionization, the latter is more than two orders of magnitude smaller. The great interest originates from the fact, that double ionization is a highly correlated process. The helium atom represents one of the most fundamental correlated bound two-electron systems, and serves as an ideal 'laboratory' to study correlated multi-electron dynamics. One way to approach this rather 'complex' process is by breaking it down into different mechanisms which are responsible for the ejection of the two target electrons by the incoming projectile (see also [McG82]). These mechanisms stand in close relation to the perturbative treatment in different orders of interaction between the projectile and the target within the Born series. Usually three mechanisms are proposed: Shakeoff (SO), Two-Step-1 (TS1) and Two-Step-2 (TS2), where the first two can be described within a first order interaction. For the TS2 process, at least two virtual photons have to be exchanged for the ejection process.

The target can be doubly-ionized by the so-called 'Shakeoff' of an electron (SO). Here, one electron is first ejected in a binary collision with the projectile. The second electron now feels the unscreened field of the nucleus, and with non-zero probability the electron can be in the continuum of the doubly-charged ion. This process should only occur, when the ejection of the first electron is 'fast' and the remaining 'bound' electron experiences a non-adiabatic change of the binding potential. The second first order mechanism is due to an interaction of the projectile with one of the target electrons by the exchange of one virtual photon (described for instance by first order Born amplitude), which in turn knocks out the second electron which finally leads to double ionization. This mechanism is sometimes called the Two-Step-1 process (TS1), where the '1' indicates, that only one interaction between the projectile and the target takes place.

Finally, the two bound electrons can be ejected by two independent and subsequent knockouts through the projectile. This process is called the Two-Step-2 process (TS2), since it is only conceivable in a second order description of the interaction of the projectile with the target. These three presented mechanisms are the simplest possible processes and where introduced as a phenomenological description of the double ionization by fast projectiles and by photons (see [McG82] and references therein).

Since the total system consists of four particles, exact formalisms are still far out of reach, therefore approximative and perturbative treatments have to be applied. Even for fast particle impact, the first order processes (SO and TS1) already show the great challenge which is met in describing double ionization. The first Born amplitude $T_{fi}^{FBA} = \langle \phi_f | V | \phi_i \rangle$ amplitude

will only yield a non-zero cross section, when the correlation between the electrons in the description of the ground state of the initial target $|\phi_i\rangle$ or the final state $|\phi_f\rangle$ is included. For double ionization one important aspect is, that the transition is extremely sensitive to the actual choice of the ground state wavefunction [BJ67]. The situation becomes more intricate through the strong electron correlation also present in the two-electron final state $|\phi_f\rangle$ (the fast scattered projectile is simply represented by a plane wave), where only approximative analytical representations exist. As a result the first Born cross section strongly depends on the chosen representation of the final and initial states. However, the framework using convergent close coupling (CCC) claims to present a numerical exact representation of the two-electron continuum. For the prediction of the total cross section in the first order regime, this issue seems to be settled. On the basis of fully differential cross sections for (e,3e) on helium, there is still disagreement even with the sophisticated CCC calculation [KBLB$^+$99]. For calculations using perturbative methods there is still an ongoing discussion about different effects and approximations, for example regarding the treatment of the initial ground state [JM03a, AMC04]. Another open question is the effect of second-order or even higher order contributions in the cross section.

In order to solve this problem, only kinematical complete experiments can provide detailed insight into the (e,3e) process. Starting from high projectile energies, at 5.6 keV reported in [LBTD$^+$99], the strong similarity between double ionization by fast charged particles and a single photon is revealed for small momentum transfers $\vec{q}$, approaching the optical limit ($q \rightarrow \Delta E/c$, ΔE: energy transfer, c: speed of light, see sec. 2.1.2). The equivalence of photoionization and charged-particle ionization allows to reduce the system to an effective three-body system when the interaction between the projectile and the target can be described in a perturbative treatment. The lowest reported impact energy is the experiment performed with the reaction microscope at $E_0 = 500$ eV, where a second-order CCC calculation shows satisfactory agreement with the relative FDCS (see Fig. 2.8). However, the coupling between the fast scattered projectile and the target fragments is still weak. Similar conclusions can be drawn from an (e,3e) experiment performed with conventional electron spectrometers at similar energy of 600 eV [ECLBC05]. In order to obtain a truly coupled four-body Coulomb system, the projectile energy has to be lowered further. Then, at projectile energies near the double-ionization threshold, the incoming projectile loses most of its initial kinetic energy in order to eject the two bound electrons from the helium atom and all final-state particles propagate at low relative velocities. This allows to gain insight into the four-body nature of electron-impact double ionization and into the strongly correlated motion of three electrons in the field of the doubly charged ion. With the present reaction microscope, (e,3e) experiments at low impact energies have become feasible such that this hitherto unexplored dynamical range can be covered.

This chapter will present results from an (e,3e) experiment performed at an impact energy of $E_0 = 105\,\mathrm{eV}$ and is organized in the following way: first an introduction to near threshold fragmentation processes is given together with a brief outline of the classical treatment first proposed by Wannier [Wan53]. Then some features of the experiment which are specific for (e,3e) measurement are discussed, followed by two sections presenting the experimental results. One section is dedicated to integrated cross sections which provide a global overview over the process. A more detailed insight is given in the discussion of fully differential cross sections.

4.3.1 Threshold Behavior for Three-Electron Escape

Going away from the quantum mechanical treatment, near-threshold fragmentation can also be treated classically or semi-classically (see 2.2.4). So far, no differential measurements of fragmentation processes with three final-state electrons have been reported. The total double ionization cross section for electron impact on He near the ionization threshold has been measured by Brion and Thomas [BT68] from excess energies of 25 eV to the ionization threshold. Their data is consistent with the characteristic square power law. More recently, a second measurement was reported for a smaller energy range (7 eV above threshold) which is consistent with the predicted Wannier exponent [DGF$^+$02]. Deviations from the simplified Wannier treatment of three-electron escape are reported for triple ionization of atomic oxygen, neon, argon and lithium by photoabsorption near the ionization threshold [SA88, WPH$^+$00, BLW04]. Very close to the threshold the experimental cross section first rises with increasing photon energy in agreement with the predicted Wannier-exponent (see Fig. 4.16). However, a few electron volts above threshold the cross section rises less steeply with a different exponent, which is described as a 'secondary' threshold law. In a theoretical treatment by Feagin [FF90], a second configuration of electron emission besides to the one predicted by the earlier treatment by Klar and Schlecht [KS76] (see sec. 2.2.4) leads to an appearance of a secondary power law for three-electron escape. The predicted secondary exponent agrees well with the one measured experimentally with oxygen and neon.

This statement has been doubted by a later calculation reported by Kuchiev and Ostrovsky [KO98], and also by Wehlitz et al. [WPH$^+$00] who presented the experimental cross section of triple ionization of Li (Fig. 4.16). There a very similar behaviour of the power law of the total cross section is observed. First the cross section rises as predicted by classical Wannier theory and few electron volts above the ionization threshold the cross section increases with a different power law which however disagrees with the secondary power law derived by Feagin. Instead the behaviour is attributed to the specific structure of Li, with one weakly bound valence electron and two strongly bound electrons in the core, where additional ionization mech-

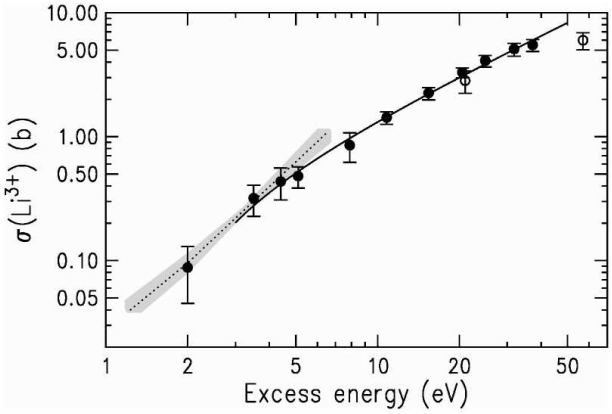

Figure 4.16: The experimental total cross section for triple ionization of lithium by by a single photon near the ionization threshold [WPH+00]. The grey-shaded line depicts the classicaly derived Wannier power law. Several eV above the threshold for full fragmentation, a different power law is observed.

anisms open up beginning a few eV above threshold.

With these questions still open, the present highly differential data for the first time provide a detailed insight to the strongly correlated three-electron continuum. At an impact energy of $E_0 = 105\,\mathrm{eV}$ used in the experiment, the total cross section still follows the cross section described by the Wannier power law (see inset in Fig. 4.17). The correlation between all three outgoing electrons should be so strong, that a perturbative treatment within the Born series should be unjustified. The 'exact' treatments of the three-body problem (like ECS and CCC) are continuously improved, such that calculations of the FDCS within these models may come in reach. First steps into this direction have already been undertaken within a quite similar framework used for calculations of total ionization cross sections, the time-depend close-coupling (TDCC). This non-perturbative method has been extended to describe three correlated electrons and provides calculations of the total ionization cross section for complete photofragmentation of lithium [CPR04]. The method has also the potential of predicting fully differential cross sections, which was very recently demonstrated for single ionization of He at low impact energies [CPCK06] .

Experimental Issues

The following section is dedicated to the specific experimental issues. The limitations of the acceptance of the electron spectrometer and possible solutions have been already discussed in section 3.4.1. The electronic circuit allows to record the coincident detection of three electrons and the recoil

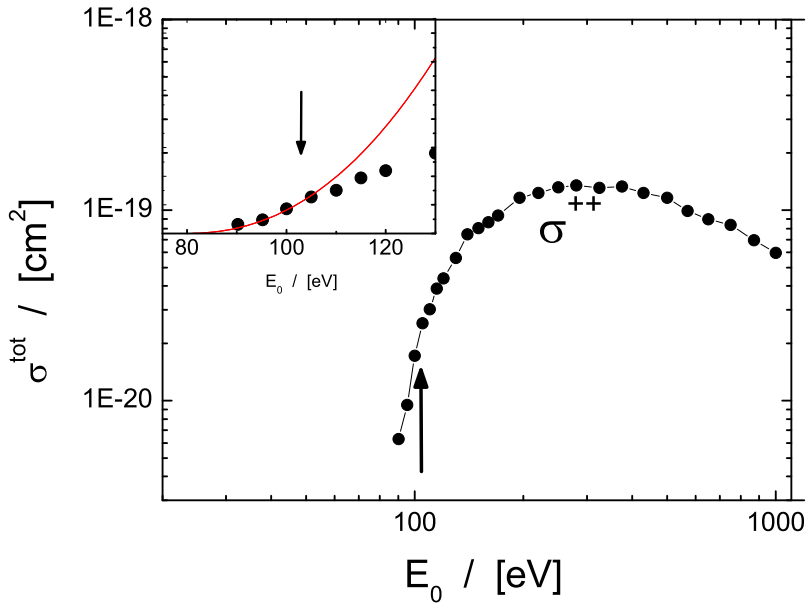

Figure 4.17: The experimental total cross section for double ionization of helium by electron impact [SEMG88]. The inset shows the expanded view on the energy range near threshold, where the curve corresponds to the predicted power law from Wannier-theory. The arrow marks the impact energy $E_0 = 105\,\mathrm{eV}$ of the current (e,3e) experiment.

ion, which is He^{++} in the case of double ionization. For the full kinematics only three of the total four final-state particles have to be detected and momentum conservation can be exploited, to reconstruct the momentum of the undetected fragment. In the evaluation of the (e,3e) cross section, only events are processed, where one ion and two electrons were detected. In the further discussion, these two electrons are labeled (1) and (2). The momentum of the undetected electron is reconstructed from momentum conservation by

$$\vec{p_{rec}} = \vec{p_0} - \vec{p_1} - \vec{p_2} - \vec{p_{ion}}, \tag{4.6}$$

where the reconstructed electron is labeled with 'rec'.

Kinematics of (e,3e) Near Threshold

The kinematics for fragmentation near the threshold strongly differs from the situation at 'high' energies. In the previous section on single ionization (sec. 4.1), the kinematics concentrated around the asymmetric geometry, where the projectile transfers only a small fraction of its momentum and energy. This allows to define the momentum transfer $\vec{q}$ and energy transfer ΔE, which are basically independent of each other. The situation in the full fragmentation of helium by electrons close to threshold is totally different. First of all, the projectile loses most of its kinetic energy E_0 and it becomes indistinguishable from the initially bound electrons. In the final state, all three electrons share the excess energy E_{exc}, which can be written down from energy conservation:

$$E_{exc} = E_0 - IP = E_1 + E_2 + E_3, \tag{4.7}$$

where $E_{1,2,3}$ denotes the energy of the three final state electrons respectively and IP is the ionization potential for double ionization ($IP = 79.0\,\mathrm{eV}$). The He^{++} carries negligible energy, due to its large mass. For the present experiment at $E_0 = 105\,\mathrm{eV}$, the electrons are left with a total excess energy of $E_1 + E_2 + E_3 = 26\,\mathrm{eV}$. On the other hand momentum conservation forces the final state particles to share the initial momentum $\vec{p_0} = (0, 0, \sqrt{2E_0})$ by virtue of

$$\vec{p_0} = \vec{p_1} + \vec{p_2} + \vec{p_3} + \vec{p_{ion}}, \tag{4.8}$$

where the z-direction is the direction of the incoming projectile beam. Without going into the detailed analysis of the kinematics one immediately sees, that neither of the electrons can carry large momentum, because none can have a kinetic energy $E_i = \vec{p_i}^2/2$ exceeding 26 eV. In order to fulfill momentum conservation, the large fraction of the initial momentum has to be carried by the ion. In the present experiment this is reflected in the momentum distribution of the recoil ion shown in Fig. 4.18 together with the sum momentum of all final-state electrons (two detected and one reconstructed). For the component transverse to the projectile beam, the fragments all have

momenta smaller than 1.2 a.u. Remembering the configuration predicted by Wannier-theory, the ion remains in the center of the three escaping electrons. This could serve as an explanation for the observed small momentum of the ion in the direction transverse to the incoming projectile momentum, since it is 'trapped' in the center of the outgoing electrons. The sum momentum of the electrons in the direction of the incoming projectile axis centers close to zero momentum. This leaves no choice for the ion but to take most of the momentum $\vec{p_0}$ of the incoming projectile. It is interesting to see, that the ion after fragmentation even has longitudinal momenta exceeding the initial projectile momentum of 2.78 a.u. (see Fig. 4.18). The large momentum transfer to the ion, in particular in the longitudinal direction, indicates that the nature of near-threshold break-up processes drastically differs from processes at high projectile velocities, where the longitudinal momentum transfer is near zero even for multiple ionization of the target [SMS$^+$00].

4.3.2 Integrated Cross Sections

In order to gain a first overview it is advisable to look at integrated cross sections. 'Integrated' is to be understood in the sense, that the cross sections presented are integrated over specific kinematical variables. This allows to gain insight into the 'global' dynamics of the process and secondly, to look for areas where the cross section is large which can be picked out to be studied higher differentially.

Energy Sharing

The partitioning of the projectile's excess energy among the three electrons in the final state continuum is shown in Fig. 4.19. The plotted cross section is differential in the energies E_1 and E_2 of the detected electrons. Electron (1) is detected first and thus has the larger forward momentum than electron (2). For each point (E_1, E_2) in the diagram the energy of the reconstructed electron E_{rec} is determined through energy conservation ($E_1 + E_2 + E_{rec} = 26\,\text{eV}$). There is a visible drop of the cross sections around the $E_1 = 15\,\text{eV}$ due to loss of momentum space acceptance resulting from the central hole in the electron detector. This particular region could not be filled by neither run of the measurement.

One can clearly identify a maximum in the cross section for the energy E_1 of the forward emitted electron close to its maximum value. This is the collision kinematics well known from fast projectile impact where collisions with small energy loss and, thus, low energies of the ejected electrons dominate. Hence electron (1) can be regarded as the scattered projectile and be distinguished from the ejected electrons with low energy. There is also an increase of the cross section, where the two detected electrons share a small fraction of the excess energy, leaving the undetected electron with the

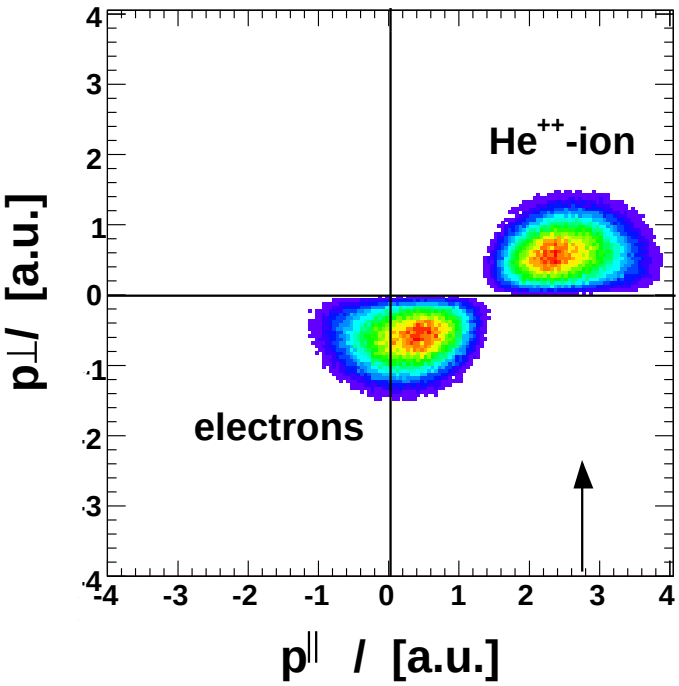

Figure 4.18: The momentum distribution of the recoil ion in longitudinal and transverse direction is shown in the upper part of the picture. The lower part shows the equivalent components for the sum-momentum of the three final-state electrons. The arrow denotes the longitudinal momentum of the incoming projectile.

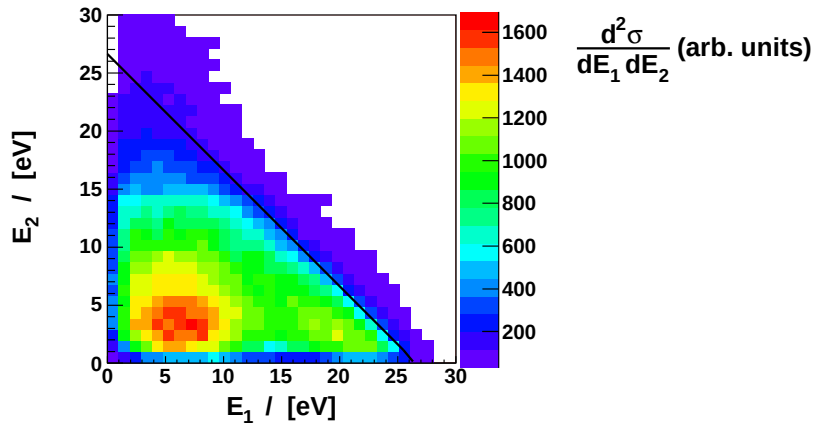

Figure 4.19: Cross sections differential in the energies E_1 and E_2 of the two detected electrons of the (e,3e) reaction with 105 eV initial projectile energy. The partition of the excess energy between the electrons shows regions with unequal energy sharing and also a further region where all three electrons have similar energy.

larger fraction. Differently from fast collisions, reactions with similar energies $E_1 = E_2 = E_{rec} \approx 9\,\text{eV}$ of all three electrons have a considerable share of the total cross section.

Mutual Angles

A further interesting aspect is the distribution of angles $P(\theta_{12}, \theta_{23})$ between the outgoing electrons. In order to treat all electrons on equal footing, the labeling of the reconstructed electron is dropped and instead all three are labeled with numbers (1), (2), (3) which are assigned randomly. For each triplet of electrons a pair of mutual angles is calculated

$$\theta_{1,2} = \sphericalangle(\vec{p_1}, \vec{p_2}) \tag{4.9}$$
$$\theta_{2,3} = \sphericalangle(\vec{p_2}, \vec{p_3}) \tag{4.10}$$

In Fig. 4.20 the angular correlation of the emitted electrons is illustrated, showing the cross section as a function of θ_{12} and θ_{23}. What is shown is the probability for specific angles, which differs from the measured rate by the weight factor $1/(\sin\theta_{12} \cdot \sin\theta_{23})$ accounting for the size of the angular line element $\sin(\theta)d\theta$. The electrons emerging from the emission show a strong angular correlation: the distribution peaks at a ridge which stretches along different 'configurations'. At the edges of the plot, there is a high

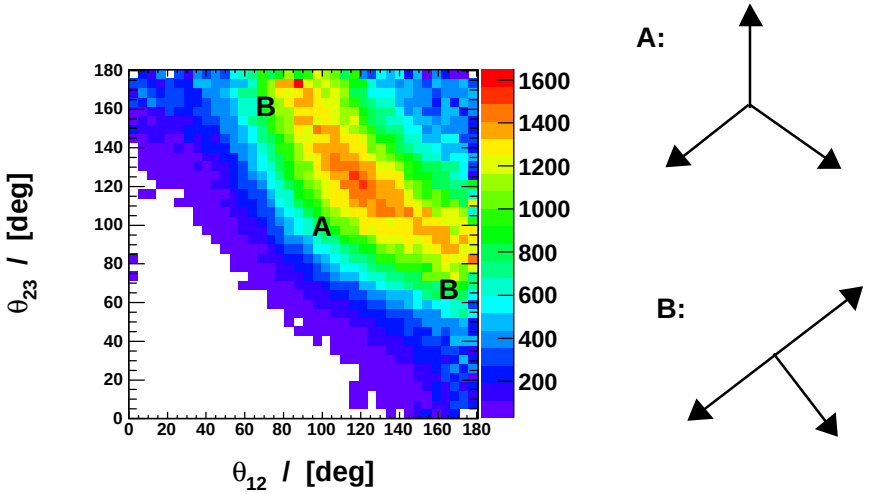

Figure 4.20: The evaluation of mutual angles between the three electrons reveals two favored configurations: one with 120°/120° (A) and another with 180°/90° (B). (Scale in arb. units)

probability for the configuration, where $\theta_{12} = 90°$ and $\theta_{23} = 180°$ or vice versa (denoted by B in the figure). This means that for these configurations, two electrons leave the ion back-to-back (i.e. at angles of 180°), and the third electron emerges perpendicular to these two. In between these extremes, there is a maximum where both electron pairs have an angle $\theta_{12} = 120°$ and $\theta_{23} = 120°$ (denoted by A). Therefore two configurations with which the electrons leave the reaction can be identified. The 120°/120° is the expected Wannier configuration predicted for three electron escape near threshold. There is a second configuration, namely the 90°/180°. It is alluring to assign the 120°/120° to the case, where all electrons share equal energy. For asymmetric energy sharing, one electron escapes with relatively high velocity, and the remaining two low-energy electrons are left in the field off the residual ion. They escape back-to-back which is also the prediction of Wannier theory to be the preferred angle for two-electron escape. However, no real consistent picture can be extracted from the data and it seems that there is no preference for a particular configuration for specific partitioning of the energy. A further difficulty in the interpretation of the data arises due to the limitations in the angular acceptance.

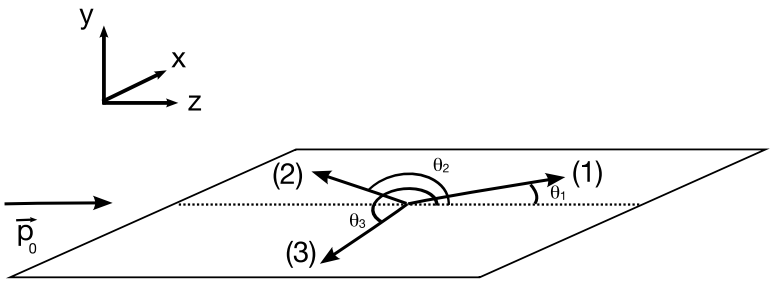

Figure 4.21: Schematical view of the coplanar collision geometry for the studied (e,3e) reactions. The solid lines represent the scattering plane. The fully differential cross section is represented as a function of the emission angle of the escaping electrons θ_1, θ_2 and θ_3.

4.3.3 FDCS for Equal Energy Sharing

The most detailed information is given by the fully differential cross section. In the following section, the discussion of the fully differential data concentrates on the equal energy sharing regime $\mathrm{E}_i = (9 \pm 3)\,\mathrm{eV}$, where the three electrons are principally indistinguishable and all the two-body interactions within the four-body system are of similar strength. Fully differential data provide the most stringent test for detailed theoretical descriptions. In analogy to (e,2e) experiments, the FDCS for (e,3e) is represented in a similar manner:

$$\frac{d^5\sigma}{d\Omega_1 d\Omega_2 d\Omega_3 dE_2 dE_3} = (2\pi)^4 \left(\frac{p_1 p_2 p_3}{v_P}\right) |T_{fi}|^2. \tag{4.11}$$

Again, $d\Omega_{1,2,3}$ are the detection solid angles of the three electrons and the fully differential cross sections are plotted as function of one electron's emission angle θ_3 for fixed emission angle of the remaining two electrons and for fixed energies $E_{2,3}$. The convention for the solid angles is to use the usual representation of spherical coordinates in the lab-frame, where the z-direction points in the direction of the momentum of the incoming projectile. The polar angle between momentum vector of the electron and the z-axis ranges from $0° \leq \theta \leq 180°$, the azimuthal angle from $0° \leq \phi \leq 360°$. This changes when the emission plane has been fixed, in which the angular emission pattern of the electron θ_3 is presented in. Then the angle between projectile axis and electron momentum, which is θ_3 in the present case, runs from 0° to 360°. In the considered emission plane, the cross sections are integrated over electron momenta within ±20° angular range above and below the cutting plane.

In the present formula (eq. (4.11)), the labeling of the electrons is arbitrary, since they are indistinguishable. For the experimentalist, this is not true, since two electrons have been detected, and the momentum of the third

undetected electron was reconstructed from the momentum of the recoil ion. There is a qualitative difference between the detected electrons and the 'reconstructed' electron. The former are detected with limited acceptance only, whereas the reconstructed electron has acceptance over the full solid angle. In the evaluation, this difference has to be handled carefully and is important for the extraction of absolute fully differential cross sections from the data set. More details about the procedure can be found in the appendix A.2.3.

Comparison with Theory on Absolute Scale

A small selection of the evaluated fully differential cross sections is shown in Fig. 4.22b. The angular correlation of the emitted electrons (1), (2) and (3) is shown for the case, where all three electron momenta lie in a common plane (coplanar scattering geometry). Absolute, fully differential cross sections are plotted as function of one electron's emission angle θ_3 for fixed emission angle $\theta_1 = 45°$ and four different angles $\theta_2 = 135°$ (a), $155°$ (b), $225°$ (c) and $315°$ (c). They are shown in a cartesian plot, where the absolute scale is the same for all presented geometries, so that the relative magnitude of each geometry becomes evident. In addition, the cross section is represented in a polar plot, which reveals the angular emission pattern. In the coplanar configuration the emission patterns are dominated by the electron - electron repulsion. In the cases (a) and (b), where electron (1) and (2) are emitted in the same half of the collision plane, electron (3) is emitted in the other half of the collision plane, evading the repulsion of the other two. For emission angles θ_3 in the vicinity of θ_1 and θ_2 the cross section is zero for an angular separation $|\theta_2 - \theta_1| = 90°$ and electron emission of the third electron in between (1) and (2) is suppressed, and only one broad peak in the cross section is observed (Fig. 4.22a).

For back to back emission of the two fixed electrons in Fig. 4.22c (i.e. $|\theta_2 - \theta_1| = 180°$), the situation gets particularly interesting. First of all, the cross section gets 'squeezed' in between the two directions of electron (1) and (2), because it has less freedom compared to the previous situations. The emission directions of the two fixed electrons form an axis. From the point of view, where only the repulsion of the electrons dominates the dynamics, the third electron should not show any preferential direction in which it is emitted: for symmetric energy sharing, the emission of electron (3) on either side of the axis formed by the back-to-back directions of electrons (1) and (2) leads to the same repulsion. However, there is a visible breaking of the 'symmetry' and electron prefers the 'forward' direction. However, the symmetry is already broken due to the direction of the incoming projectile. The initial momentum $\vec{p_0}$, which points in the direction of $0°$ has to be carried mainly by the recoil ion. For this particular geometry, the sum momentum of the two fixed electrons (1) and (2) is zero. If the third electron is emitted

in the opposite direction of the incoming projectile, the residual ion has to take the momentum of the incoming projectile and an additional component in z-direction in order to balance the momentum of the 'backward' emitted electron. Apparently, the 'forward' emission of electron (3) is preferred, where the ion carries less momentum.

If the angle of electron (2) is increased further to $\theta_2 = 315°$, the electron (3) is emitted mainly to 180°, which can be easily explained by the electron repulsion. It is however interesting, that this configuration has the largest cross section of all considered geometries.

Theoretically, the emission characteristics for low energetic ($E_{exc} = 0.5$) eV electron impact double ionization was first studied by Malcharek and Briggs [MB97]. A six Coulomb wavefunction approach (6C) is applied, which is an extension of the widely applied 3C wavefunction. The 6C is an approximative representation of the correlated four-body continuum, and similar to the 3C approach, it takes into account the interactions of all six two-body subsystems present within the four-particle system. This representation is only exact when all other particles are infinitely separated from the selected two-body subsystem. The presented results are from a 6C calculation for $E_0 = 105\,\text{eV}$ projectile energy and a six Coulomb wave model with dynamical screening (DS6C), where some of the deficiencies of the 6C model are removed. The DS6C calculation accounts for the screening of the two body potential by the presence of further charged particles [BB94, GWB03, GB].

The different behaviour of both models is obvious in Fig. 4.22a. The 6C calculation (dashed line) obtains a structure-less peak which is broader and shifted by about 30° compared to the experimental result. DS6C obtains a fairly different pattern showing two maxima with the larger one coming close to experimental peak in position and width. The smaller maximum is at a position where the experiment shows only a long tail of the main peak towards smaller emission angles. Clearly the inclusion of dynamical screening shows a great improvement in comparison with the experimental data. The same is true for the slightly larger angle $\theta_2 = 155°$, where the dynamical screening leads to a cross section which is much larger than the cross section calculated from the 6C model. For the back-to-back configuration (Fig. 4.22b) the Coulomb repulsion strongly restricts the accessible angular range θ_3. In consequence, both calculations show similar peak widths and positions agreeing well with the experiment but they differ in the relative height of the two peaks. The absolute magnitude of the DS6C calculation is again in better agreement. Here the DS6C calculation reproduces the experimental cross section very well. In the final geometry with $\theta_2 = 315°$, the two calculations reproduce the peak position and the width, but have the wrong magnitude. From the data one cannot decide, whether the dip predicted by the DS6C calculation is present or not.

Finally in Fig. 4.23 we show a geometry where the momentum vector of electron (2) is perpendicular to the plane containing the incoming beam

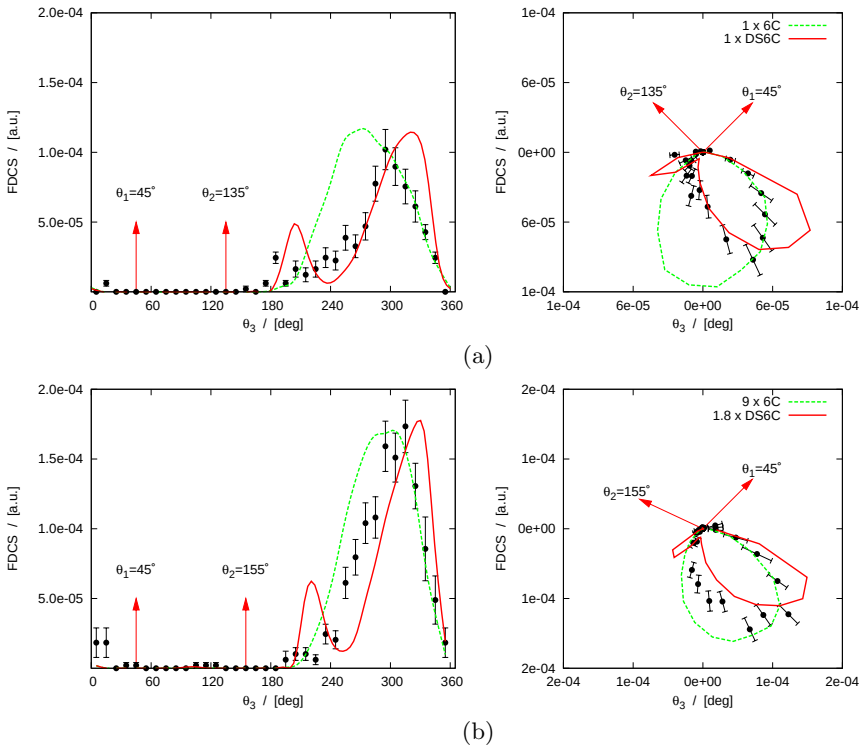

Figure 4.22: The plots show the absolute fully differential cross section for coplanar geometry and equal energy sharing in a cartesian plot (left) and in a polar plot (right). The angular emission of one electron is shown, with the polar-angle of the two other electrons remaining fixed. The scaling factors for the theoretical calculations 6C and DS6C are displayed in the upper right of the polar plot.

and the other two electrons. Thus the electron repulsion between this electron and the electron (3) varied in angle is constant over the full angular range of θ_3. Since now the angular emission pattern of the scanned electron is not dominated by final state repulsion, it shows more structure with a broad peak at 180° and a second peak around 300°. Calculations now differ strongly, while 6C shows only one maximum, DS6C obtains a second peak coming closer to the experimental result.

There are possible reasons for an apparent disagreement with the calculation. On one hand the size of the cuts can effect the shape and the magnitude of the cross section. On the other hand details of any structures in the emission pattern can be blurred by the limited angular resolution. The resolution is worst for the reconstructed electron, since there the limitations due to the finite jet-temperature appear. Here the angular resolution can be estimated from the resolution of recoil ion, which in turn can be determined

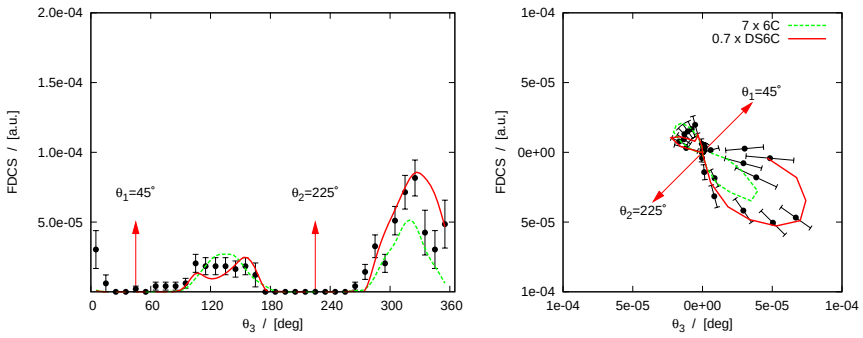

(c)

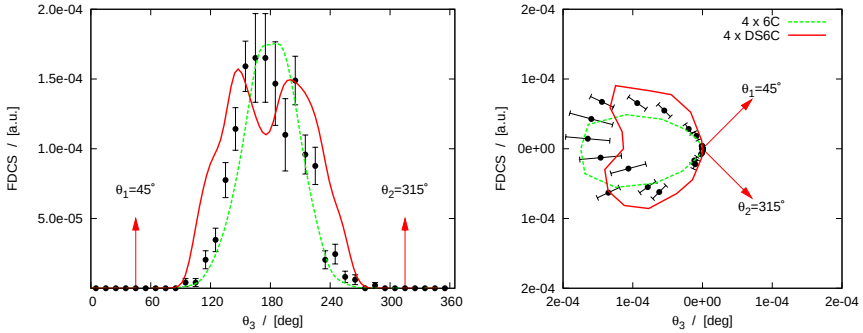

(d)

Figure 4.22: continued

experimentally from the fourfold coincidences (see Fig. A.4). Depending on the emission direction of the reconstructed electron, the resolution ranges from approximately $\Delta\theta = 10° \ldots 30°$, which can serve as an upper limit. To fully explore the effects of the size of the cuts and the resolution would require to apply a folding procedure on the theoretical curves. At the present status this is still beyond reach, considering the fact that the calculation in each single scattering geometry needed a computation time of several days.

The disagreement is possibly also based on the calculation. Similar to the 3C calculation used for description of three-body continuum, the 6C wavefunction is only an approximative approach of the four-body continuum. For the symmetric energy sharing, the division of the four-body system into two-body subsystems as it is done with the 6C approach, is actually not justified. The added dynamical screening leading to the DS6C wavefunction provides a great improvement for most geometries presented here. Therefore the data clearly confirm this statement.

Concerning the absolute magnitude of the cross section, the two presented models 6C and DS6C are not expected to yield accurate results [GWB03]. Further, it is already known, that for single ionization the approach of using an 'ansatz' with Coulomb wavefunctions leads to good agree-

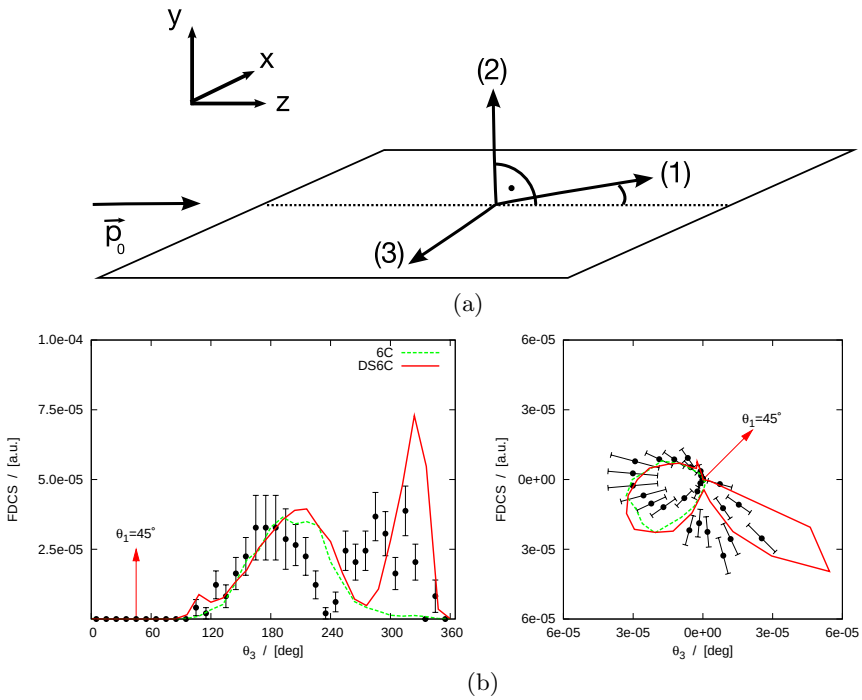

Figure 4.23: The absolute fully differential cross section for symmetric energy sharing non-coplanar geometry, as depicted in the schematical view in the top of figure.

ment at some geometries, and to disagreement to others. To some extent this depends on the choice of the dynamical screening, where many different approaches are in principle possible. For (e,2e) cross sections the complementary 3C and DS3C approaches show a trend to better agreement, where the FDCS is dominated by the final-state electron-electron interactions. On the other hand the 3C and DS3C approach do less well, when other interactions become more important. Often the failure of these approaches is traced back to the missing treatment of the coupling between target and the incoming projectile in the incident channel [LRW99, JM00]. It is very interesting to see, that these statements are partly confirmed in the (e,3e) cross sections presented here: the electron-electron interaction of the final state should be very strong in the case of Fig. 4.22c, where $\theta_2 - \theta_3 = 180°$. Here the calculation shows very good agreement. On the other hand, the agreement gets worse, where electron (3) has a larger freedom with respect to the available angular range, where it can avoid the repulsive force of the other two electrons.

4.3.4 FDCS for Unequal Energy Sharing

In the introducing chapter, experimental cross sections at two different impact energies, $E_0 = 2\,\mathrm{keV}$ and $E_0 = 500\,\mathrm{eV}$, where presented for double ionization. The overall shape was consistent with a perturbative calculation describing the process by the exchange of one and two virtual photons at the higher and lower impact energy, respectively. At the impact energy of $E_0 = 105\,\mathrm{eV}$, the cross section is dominated the dynamics of the final state, which is the repulsion of the three escaping electrons and their mutual screening by the He^{++}-ion. This marked difference can be highlighted by comparing the emission of the electrons in the coplanar geometry for a chosen energy of $E_2 = E_3 = (5\pm2)\,\mathrm{eV}$ for all three impact energies. The problem is, that near threshold the momentum transfer is mainly given by the energy transfer, and does not dominate the dynamics as in the perturbative regime. In order to define the full kinematics, the scattering angle of the electron with the high energy ($E_1 = 15\,\mathrm{eV}$) was kept fixed at $\theta_1 = (45\pm20)°$, which was partly given by the constraints in acceptance and the statistics. The detector hole leads to zero acceptance for $-20° \leq \theta_{2,3} \leq 20°$ and $160° \leq \theta_{2,3} \leq 200°$. The coplanar emission for near threshold impact energies is shown as a function of the planar emission angles θ_2 and θ_3 (labeled θ_b and θ_c in the figure) in Fig. 4.3.4 in comparison with the already presented results at the higher energies. In the perturbative regimes, the nodal lines resulting from the dipolar selection-rules are inserted (solid and doted lines). In the plot at the low impact energy of $E_0 = 105\,\mathrm{eV}$, these selection rules do not make any sense, however, the angles at which the repulsion suppresses the emission lines have been drawn. In the coplanar geometry, these lines go along $\theta_2 = 45°$ and $\theta_3 = 45°$, which result from the repulsion from the

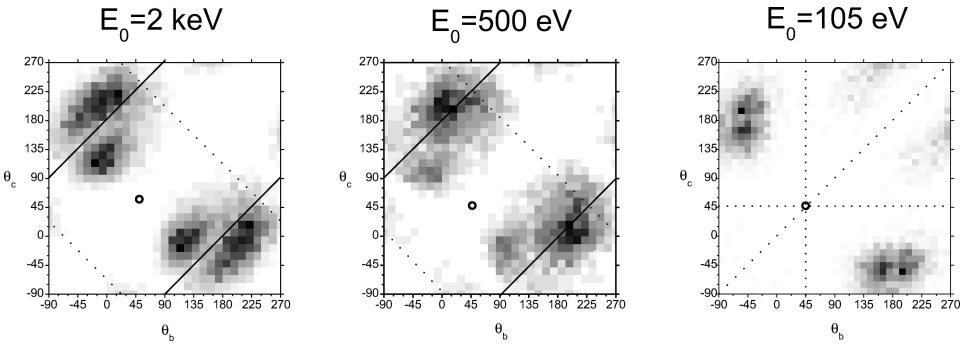

Figure 4.24: Comparison of the coplanar emission of two 5 eV electrons in (e,3e) on He at three different impact energies 2 keV, 500 keV and 105 eV. At the high impact energies (2 keV and 500 eV), the circle indicates the direction of the momentum transfer. At the low impact energy of 105 eV the circle denotes the emission angle of the third electron.

electron fixed at $\theta_1 = 45°$ and also the mutual repulsion of the two plotted electrons $\theta_2 = \theta_3$. The cross section is distributed in between these lines, which is just the behavior observed at equal energy sharing.

4.3.5 Concluding Remarks

In this chapter the first data obtained from a kinematically complete experiment on double ionization of helium with low energy electrons $E_0 = 105$ eV were presented. Hereby detailed insight into the correlated dynamics of in total four continuum particles is provided. The dynamics is dominated by the repulsion of the three electrons and by the positively charged ion, which screens the electrons. At this energy, the total cross section coincides with the prediction of classical Wannier theory and hence the presented cross sections have been obtained in a dynamical regime, where its predictions can be tested. The probability distribution for mutual angles reveals two preferred configurations for three electron escape from the ion. In one configuration the three electrons have mutual angles of 120°, which corresponds to the prediction by the classical analysis. A second configuration appears, where two electrons are emitted back-to-back and the remaining electron is emitted in an angle of 90° with respect to the others. A possible explanation is, that at the excess energy of 26 eV one is already beyond the regime, where the threshold laws can be applied. However, no theoretical predictions of such a second configuration, besides the one predicted by Wannier, exist. In a classical simulation of triple-photoionization of lithium, also representing a three electron escape process, a similar trend was observed. Within the so-called classical trajectory monte carlo calculation (CTMC), two preferred configu-

rations of electron emission like the ones seen in the (e,3e) experiment were observed [ER04]. However, there is strong difference of the lithium target compared to helium, and this measurement will hopefully stimulate further CTMC calculations describing electron impact double-ionization of helium. First calculations of this system have already been published at a higher impact energy of $E_0 = 250\,\mathrm{eV}$ [Gey04].

Apart from these global views, fully differential data were obtained. These provide insight which go well beyond reach of any prediction by threshold laws, since there the collision dynamics is neglected. These cross sections, which were obtained on an absolute scale, provide benchmarks for theoretical descriptions of the four-body Coulomb continuum. Also on the highly differential scale, the strong influence of the electron-electron repulsion is clearly visible in the angular distribution. At close sight, details of a more complex four-body dynamics show up, which is also supported by comparison with a theoretical calculation. The data were compared with a 6C and the more sophisticated DS6C calculation including additional screening effects, which can be seen as a more appropriate description of the system. The dynamical screening improves the agreement with experimental data, with respect to the shape of the angular emission and also shows a richer structure. Apparently, the screening effect - the correlation between all four continuum particles - is of great importance. For some geometries, the agreement between theory and experiment is good, for others disagreement appears. The possible reasons are the well known deficiencies of the calculation, for example the missing treatment of the interaction of the incoming projectile with the target, which has to be taken into account at this low projectile velocity.

The presented experiment marks the first step, where the strongly correlated motion of three electrons has been explored in great detail. The feasibility of studying multiple fragmentation processes with the novel reaction microscope could be demonstrated. Clearly, progress has to develop hand-in-hand with theoretical models in order to gain better understanding of the process and hopefully, the present experiment will stimulate theoretical efforts towards descriptions of the correlated four-body system. For the lively debated field of double ionization of helium by charged particle impact, the kinematical complete data at low energy provide a further guideline for the existing and also future theoretical frameworks. It should be pointed out, that the discussed fully differential cross sections represent only a very small fraction of the total phase space which was recorded.

Chapter 5

Summary and Outlook

The present work is dedicated to study fragmentation of helium by electron impact with an improved reaction microscope. The experimental method relies on the combined electron and recoil ion momentum spectroscopy using an imaging technique, which is widely applied in charged particle and photon induced fragmentation experiments [UMD+03]. By aligning the projectile beam parallel to the imaging fields, all final state electrons, including the scattered projectile, can be detected, and the achievable resolution could be significantly improved. Low impact energies far below 100 eV can be realized and thus the regime, where the incoming and outgoing projectile cannot be longer regarded as a small perturbation, can be accessed experimentally. By installing a state-of-the-art position encoding device for electron detection with essentially zero dead-time, a so-called Hexanode [Jea02], the acceptance for processes where several electrons are emitted is improved.

Firstly, measurements at high energy impact single ionization of helium where undertaken, where the underlying dynamics is predominantly reproduced by a first Born description. On a very detailed scale, the fully differential cross sections represented as three-dimensional images are compared with the enigmatic results from fast ion-impact with 100 MeV/u C^{6+} projectiles [SMF+03]. For both cases the strength of the perturbation $|\eta| = |Z_P|/v_P$ is approximately 0.1 a.u. and at the same momentum and energy transfer the cross section should be essentially identical in the first order description. This is partly confirmed for the FDCS in the scattering plane, where both the angular emission pattern as well as the absolute magnitudes agree. Turning to the details, the observed differences in the angular emission upon change of the sign of η can be clearly attributed to higher order processes in the projectile target interaction. These are especially pronounced for the electron emission outside the scattering plane. For both projectile-charges distinct structures appear in the out-of-plane geometry, clearly indicating the presence of higher-order contributions. Surprisingly, the well established theoretical framework applied for both projectile

systems, based on the so-called 3C wavefunction [BBK89, MSJ$^+$01], agrees perfectly in the scattering plane, but drastically fails to reproduce the enhanced emission in the non-coplanar geometry. For electron-impact, this enhancement can be reproduced by a second Born calculation, which shows satisfactory qualitative and quantitative agreement. However, several theoretical models (second Born, Eikonal and Glauber approximation [VNU03]) which agree with negatively charged projectiles, show strong disagreement with the experimental FDCS obtained for ion-impact. The new (e,2e) data corroborate the results for ion impact, where the experimental resolution was made responsible for a part of the so far observed discrepancies with theory [OF05], by complementary measurements performed with the advanced reaction microscope for electron impact. In future, theoretical calculations which have been established in the past decades will probably have to be reviewed with respect to the underlying approximations.

In order to highlight the issue further, (e,2e) measurements on helium were performed at a lower impact energy $E_0 = 102\,\mathrm{eV}$. The FDCS are compared with one of the most sophisticated calculations available in electron impact ionization. At this impact energy, only a full treatment of the couplings between all active collision partners is expected to provide an adequate description. Indeed, the Convergent Close Coupling method, which claims to represent an 'exact' description of the dynamical three-body Coulomb-problem, shows excellent agreement for both the coplanar and also in non-coplanar geometry. The perturbative second Born treatment using distorted waves expectedly leads to poor agreement for parts of the angular emission. However, good agreement is observed in the out-of-plane geometry, which serves as an important and sensitive benchmark for approximations made in the evaluation of the second Born amplitude [CM05, Che06]. Considering the open situation in single ionization of helium by positive ions, higher differential data on positron impact ionization are urgently needed. This would allow to directly compare charge sign effects of projectiles with equal mass, which has not been possible before. With the advanced reaction microscope, such type of experiments can be performed at the newly installed facility NEPOMUC at the research-reactor FRM-II in Munich, where high-intensity positron beams can be supplied (e.g. [HSSS05]).

Furthermore, absolutely normalized fully differential cross sections for single ionization with simultaneous excitation of the second bound electron into $He^+(n = 2)$-states were obtained at 105 eV impact energy. A large part of the final momentum space was covered and the emission over almost the complete solid angle of the ejected electron can be presented for the first time. Since also a wide range of angles of the scattered projectile is recorded, the capacious data set allows to systematically study the poorly explored (e,2e) ionization-excitation cross sections at a given impact energy. Autoionizing resonances from doubly excited states of neutral helium below the N=3 threshold have been observed with resolved angle of the

emitted electron. Thus their influence, which has been recently discussed for the scarce data available on ionization-excitation obtained so far, can be studied as well. With the very recent developments, in particular in coupled-channel approaches like R-matrix or the Convergent Close Coupling (CCC) calculations, the data serve as ideal testing ground for descriptions going beyond the well established three-body treatments, because of the similarity in the final-state with two electrons in the continuum. Exact approaches like the mentioned CCC and the Exterior Complex Scaling (ECS) are currently developed towards this direction [PNB$^+$04, HMR05a], and hopefully the presented measurements will stimulate further theoretical efforts.

Finally, (e,3e) cross sections were obtained for double ionization of helium at an impact energy of 105 eV. This marks an advancement into a new dynamical regime, which has remained unexplored in previous (e,3e) experiments. At this low energy, a perturbative treatment of the projectile-target interaction is no longer justified. Therefore, the data present an ultimate challenge to theory, where the strongly coupled dynamics of four final-state particles in the continuum, three electrons and the He^{++}-ion, has to be described appropriately. In integrated cross sections, a global view over the final-state is obtained. The distribution of mutual angles reveals two different configurations, at which the electrons are emitted from the collision. Partly, the electrons leave at a mutual angle of 120°, which is the so-called Wannier configuration. The distribution of mutual angles shows a second maximum at 90°/180°, where two electrons are emitted back-to-back (i.e. in opposite directions), the third being emitted perpendicular to the directions of the two others. This appearance of two different modes of three electrons leaving the field of the ion in an atomic ejection process, is the first angular resolved experimental exploration of three-electron escape near threshold. It would be interesting to see, if such a behavior can be reproduced by a calculation, for instance by Classical Trajectory Monte-Carlo methods [ER04, ER06]. Furthermore, absolutely normalized fully differential cross sections are discussed for equal energy sharing and coplanar geometry as well as for non-coplanar geometry. The general behaviour of the angular distributions of the ejected electrons leads to the conclusion, that the shape of the FDCS is dominated by the strong repulsion of the electrons in the final state. However, not all features can be explained by the repulsion alone, and more complex dynamics, for instance due to the mutual shielding by the He^+-ion, is revealed. The cross sections are compared with two calculations: first, with a calculation using the 6C wavefunction, which is an approximate representation of the four-body continuum and only treats each two-body subsystems in an exact manner. Secondly, the effects from mutual screening, which are poorly represented in the 6C wavefunction, can be studied by the more elaborate DS6C, where the so-called Dynamical Screening is additionally included [BB94]. Although not designed to predict the absolute value of the cross section, good agreement with the DS6C calculation

for a part of the analyzed scattering geometries is observed on the absolute scale. With respect to the angular shape, the Dynamical Screening leads to a richer structure than the 6C calculation, however fails to reproduce the exact positions and the heights of the observed lobes. In order to understand this process in more detail, the data need to be compared with other calculations, which can also predict the absolute differential cross section.

Concluding, for the first time, 35 years after the pioneering (e,2e) experiment of Ehrhardt et al. in 1969 [ESTW69], the fully differential cross section for single ionization of helium was obtained for the emission of the ejected electron into all three spatial dimensions. At two different impact energies, in the high velocity regime at 1 keV and at 102 eV, the largest fraction of collision geometries could be covered, where most of the ionizing collisions occur. The presented fully differential cross sections provide a comprehensive and consistent data set on one of the most simple dynamical quantum systems, which are of utmost importance to benchmark 'exact' theories, like the recently developed CCC or ECS approaches, respectively at up to keV impact energies under any kinematical and geometrical conditions. As it was demonstrated in this work, the CCC calculations show excellent agreement for (e,2e) on He at $E_0 = 102$ eV impact energy. In case of agreement also at the high impact energy of $E_0 = 1$ keV, which will be tested in the near future, (e,2e) on one and two electron systems can be considered as completely understood! This would be a major step forward representing a sound basis for understanding of more complicated and, at the same time, more relevant systems for applications up to the interaction of slow electrons with bio-molecules and DNA. In this respect, the recorded cross sections for ionization-excitation and double ionization of He serve as guidelines for theoretical models, which treat true dynamical four-body systems. In total, an extensive and very detailed data set was acquired for three different dynamical processes of the helium atom at essentially the same impact energy.

With respect to future perspectives, the refinements of the reaction microscope opens a big field of further studies. With the possibility to detect all final-state electrons in (e,2e) processes, and thus determining the full kinematics, essentially all gaseous targets can be studied. Previously, this was not feasible, because the reaction microscope relied on the resolution of the ion momentum. Targets heavier than helium lead to a poor momentum resolution of the recoil ion, resulting from the finite temperature in the target beam. Here, atomic hydrogen or noble gas atoms are possible candidates for further studies, but also molecular targets, where cross sections in the molecular frame can be obtained by imaging the fragments after dissociation of the molecule. Such an experiment exploring 'fixed-in-space' molecules has already been performed recently [Haa06] with the present reaction microscope. A new electron source using a GaAs photocathode is ready to be implemented and can provide a cold and pulsed electron beam,

with provides better focussing abilities and a shorter temporal pulse-width than the present electron gun. This allows to perform experiments at very low energy (a few eV) and with higher resolution, where the superior imaging techniques of the reaction microscope can be applied to explore phenomena in electron-molecule reactions.

Appendix A

Appendix

A.1 (e,2e) at 1 keV

A.1.1 Kinematics at High Impact Energies

When charged particle ionization is considered at small momentum and energy transfer and at high impact energies, the collision kinematics can be considerably simplified. When the relative energy-loss $\Delta E/E_0$ being small compared to the incoming projectile energy E_0, the relation between ΔE and the change of the absolute length of momentum vector of the scattered projectile Δp can be linearly approximated

$$E_0 - E_1 = \Delta E \approx \frac{p_0}{m}\Delta p. \tag{A.1}$$

The momentum transfer is conveniently expressed in cylindrical coordinates $q^{\parallel}$ and $q^{\perp}$ due to the cylindrical symmetry with respect to the projectile axis (=z-direction). For small scattering angles Δp is in good approximation equal to the longitudinal momentum transfer $q^{\parallel}$ (see Fig. A.1). With $p_0 = mv_P$ and by inserting $\Delta E = E_2 + \mathrm{IP}$ into eq. (A.1) one reaches the useful relation:

$$q^{\parallel} = -\frac{E_2 + \mathrm{IP}}{v_P}. \tag{A.2}$$

The minus sign accounts for the fact, that the projectile has lost energy, and therefore the absolute momentum of the scattered projectile p_1 is smaller than the initial momentum p_0[1]. At fixed energy of the ejected electron, the momentum transfer cannot be less than $q_{\parallel} = (E_2 + \mathrm{IP})/v_P$ which for these reasons is sometimes called the minimum momentum transfer q_{min}. At large projectile velocities $q^{\parallel}$ is typically small. In the ion-impact collision with $v_P = 60$ a.u. the longitudinal momentum transfer is essentially zero and hence the momentum transfer vector $\vec{q}$ is perpendicular to the incoming projectile axis.

[1] which means that ΔP is negative, indicating a decrease of momentum

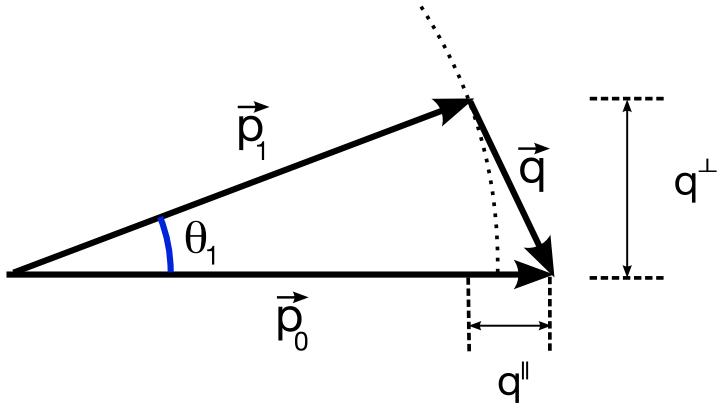

Figure A.1: Figure showing the kinematics of the scattered projectile in electron impact ionization and the asymmetric scattering geometry.

The relation (A.2) allows to obtain the longitudinal momentum transfer directly from the energy of the ejected electron E_2, such that the longitudinal momentum of the scattered projectile is not needed. In addition a much higher resolution than by the direct determination of $q^{\parallel}$ can be reached.

A.1.2 Resolution Effects

The impact of the resolution on the FDCS is an important aspect, since it may lead to apparent disagreement between theory and experimental data. For the evaluation of the FDCS the scattering plane has to be determined, since it manifests the 'reference' coordinate system of the collision. This is achieved by determining the momentum transfer $\vec{q} = \vec{p_2} + \vec{p_{ion}} = \vec{p_0} - \vec{p_1}$, where the scattered electron is labeled with the index (1), and the ejected electron with index (2). For the experiments on ion-impact performed with the reaction microscope the momentum transfer is determined from the momenta of the fragments $\vec{q} = \vec{p_2} + \vec{p_{ion}}$. As the longitudinal momentum transfer can be obtained from the energy loss by eq. (A.2), only the resolution of the transverse components of the momentum transfer $q^{\perp}$ and ϕ_q is of importance. The critical issue arises due to the poor resolution in jet-direction (y-direction in the laboratory-frame, see also discussion in sec. 3.4.3). For the present experiments, as for typical ion-impact data, the recoil-ion momentum resolution is $(\Delta p^{\perp}, \Delta p^{||}) \approx (0.25, 0.15)$ a.u., which is mainly determined by the initial temperature of the target jet. This only affects the transverse components of the momentum transfer and the resolution of the momentum transfer in ion impact experiments is estimated to $\Delta q^{\perp} = 0.25$ and $\Delta\phi = 15° - 20°$. The poor resolution of the momentum transfer can have two effects:

1. As the FDCS is evaluated for a cut in $q^{\perp}$, the limited resolution of $q^{\perp}$

will lead to contributions from higher or lower momentum transfers $q^{\perp}$. Since the FDCS strongly increases at small momentum transfer $|q|$, this effect should appear especially at small values of $q^{\perp}$.

2. The effect of the poor resolution of ϕ_q will lead to blurring of the three dimensional FDCS around the axis of the incoming projectile. In particular this may result in an increase of the cross section in the perpendicular plane, when for instance intensity from the binary-peak in the scattering plane 'leaks' into out-of-plane geometry.

With the electron impact experiments the effect of the poor resolution from the jet-temperature can be studied by comparing the FDCS evaluated at equal conditions for two different ways of determining the momentum transfer. In one case the momentum transfer is determined directly from the scattered projectile $\vec{p_0} - \vec{p_1}$ in the other from the target fragments $\vec{p_2} + \vec{p_{ion}}$.

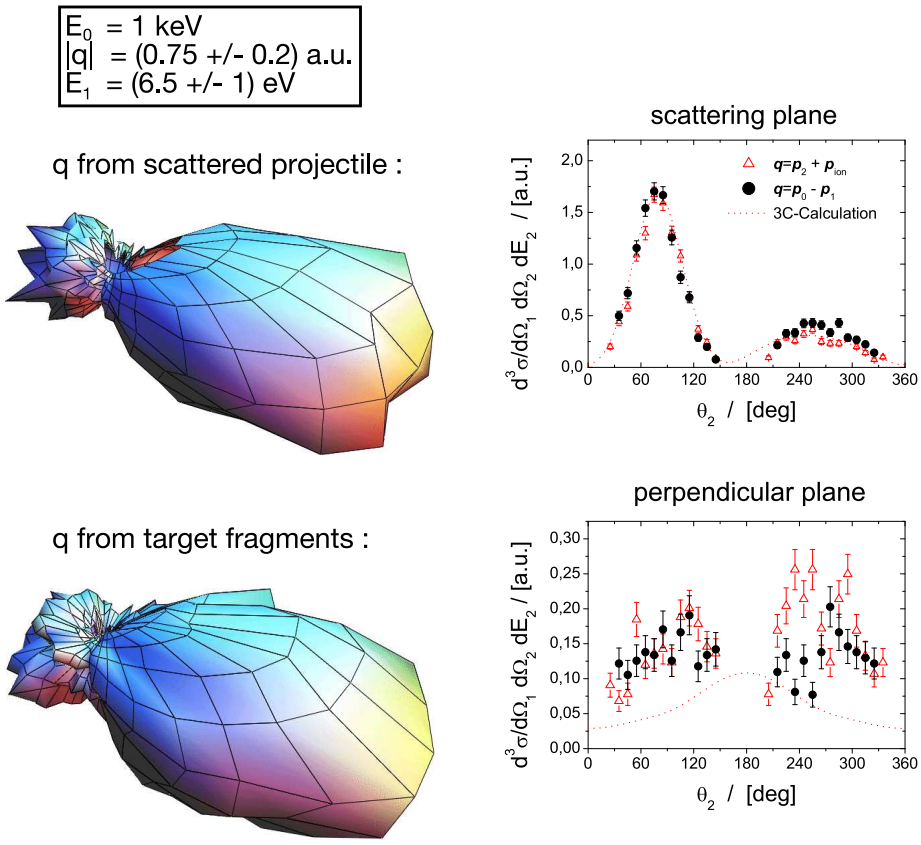

Figure A.2: Comparison of three dimensional cross section images (left) and the cuts in the scattering and perpendicular plane (right) for the two different ways of determining the momentum transfer.

Resolution of the Scattered Projectile

The resolution of the transverse momentum for the scattered projectile $p_1^{\perp}$ and ϕ_1 can be optimized by tuning the magnetic field such, that the scattered electrons are between the wiggle, where the resolution is best. At 1 keV impact energy and for the energy-losses of maximal 50 eV studied in the present experiment, the time-of-flight can be assumed to be equal for all scattered projectiles. It can be directly calculated from the total path from the interaction zone to the detector of 33 cm and amounts 17.6 ns. Therefore the magnetic field has to be matched such that the time for one cyclotron revolution t_{wig} amounts twice as much, leading to a resulting field of 10.8 Gauss. This automatically determines the transverse acceptance for both the scattered projectiles and the ejected electron. The fact that fast electrons resulting from inelastic collisions cannot be separated from elastically scattered projectiles may result in background from the latter process. Due to the threefold coincidence the background due to competing process is efficiently suppressed, which can be verified by checking the momentum-balance for the transverse components in x- and y- direction for all final-state particles. The achieved transverse resolution of the scattered projectiles is estimated to $\Delta p_1^{\perp} \leq 0.1$ a.u. and $\Delta\phi_1 \leq 6°$, which also the resolution of the momentum transfer.

A.1.3 Normalization Procedure of the FDCS

Although from the shape of the angular distribution already gives detailed information, only the absolute value of the cross FDCS provides a stringent test of theoretical descriptions of the ionization process. Recalling the formula presented in sec. 3, which links the measured rate with the FDCS

$$R = \frac{d^3\sigma}{d\Omega_1 d\Omega_2 dE_2} \cdot \Delta\Omega_1 \Delta\Omega_2 \Delta E_2 \epsilon_1 \epsilon_2 \cdot Nj, \tag{A.3}$$

one sees that for determination of the absolute scale of $d^3\sigma/d\Omega_1 d\Omega_2 dE_2$ the product of target density and beam current density Nj and the detection efficiencies have to be known. The solid angles and the accepted energy interval are given by the size of the applied cuts or the size of the binning chosen in the offline analysis. When triple coincidences are measured, then a third factor for the detector efficiency additionally enters. Experiments with the reaction microscope do not actually measure the rate, but the total number of events, i.e. the rate integrated over the measurement period. However, this can be considered by integrating over time on both sides of eq. (A.3) and doesn't change anything in the argumentation. As soon as all the experimental parameters are known, the absolute FDCS can be determined by dividing the measured rate by the factors on the right hand side of eq. (A.3). Although such a procedure is possible in principle, the deter-

mination of those parameters can be difficult and is often connected with big uncertainties ranging from 20 % up to 200 % [vWKvTdH81, BKHM78].

Instead, there are several other possibilities to normalize the measured rates relative to known cross section taken from the literature which have been measured with a different method and with high accuracy and precision. With 'conventional' reaction microscopes, where only the target fragments are detected, the absolute value of the FDCS is determined by integrating over all accepted momenta of the recoil ion and the electrons. For the vast majority of the occurring single-ionization events, the final-state momentum space of the fragments is covered by the imaging technique. This is due to the fact, that in the pertubative regime the cross section is highest at small energy and momentum transfer, and thus mainly low energy electrons are emitted. Therefore the total number of recorded events corresponds to the total cross section for single ionization. Hereby the proper scaling factor is found, which is equal to the factor on the right-hand-side of eq. (A.3).

For the present measurement, this procedure is not possible, because not all areas in momentum space can be covered. Especially for the scattered projectile only a limited range of transverse momenta and thus scattering angles can be detected, making a different normalization procedure necessary. In conventional (e,2e) experiments a large variety of alternative normalization methods have been devised, and are reviewed by Rösel et al. [RRF$^+$92a]. Some of these methods exploit the fact, that single ionization of an atom is equivalent to photoionization in the limit of zero momentum transfer ($q \to 0$). The measured FDCS is related to the photoionization cross section, which can be measured with a high accuracy with typical errors of 3% [SS02]. The normalization procedure which was applied to the 1 keV data taken with the reaction microscope is discussed in the following section.

Extrapolation of the GOS to Zero Momentum Transfer

Already in the early paper of Bethe [Bet30], the close relationship between single ionization induced by a charged particle and photoionization was shown. The theoretical treatment has been extensively reviewed by Inokuti [Ino71]. The optical property of an atom is characterized by the oscillator strength df/dE, which reflects the 'structure' of the considered atom. It characterizes the photon-induced transition between different atomic states with energy difference E, including continuum states of the active electron. This property enters into the photoionization transition probability $\mathrm{d}\sigma/\mathrm{d}\Omega$ by

$$\frac{d\sigma}{d\Omega} = 2\pi^2 \alpha \frac{df}{dE}, \tag{A.4}$$

where α is the fine-structure constant and using atomic units [FC68].

In the first Born approximation a similar relation between the FDCS and the generalized oscillator strength $df(q)/dE$, which additionally depends on

the momentum transfer, can be found:

$$\frac{d^3\sigma}{d\Omega_1 d\Omega_2 dE_2} = \frac{4p_1}{q^2 p_0 (E_2 + \mathrm{IP})} \frac{df(q)}{dE}. \tag{A.5}$$

The important point is, that the generalized oscillator strength (GOS) is equal to the optical dipole oscillator strength in the limit of vanishing momentum transfer, i.e.

$$\lim_{q \to 0} \frac{df(q)}{dE} = \frac{df}{dE}. \tag{A.6}$$

This relation is always true and is independent of the validity of the FBA for non-vanishing momentum transfer. The problem is, that the limit of zero momentum transfer cannot be reached, due to the minimal momentum transfer q_{min} present in inelastic collisions. Additionally small momentum transfers may not be accessed experimentally, since they correspond to very small scattering angles. Therefore the experimentally obtained GOS has to be extrapolated to q=0, which is a questionable procedure as it may lead to an inaccurate result. In a publication by Jung et al. [JMFS$^+$85], an extrapolation procedure is discussed, which makes use of the specific properties of the angular emission pattern in single ionization. The experimental GOS is evaluated only in the direction of the binary and the recoil peak. At high impact energies they point in the direction and in opposite direction of the momentum transfer $\theta_{\pm q}$, respectively. The experimental GOS is given by the unnormalized intensity of the FDCS in the binary (or recoil) peak as a function of the momentum transfer:

$$\frac{df(q)}{dE}^{exp} = q^2 \frac{d^3\sigma(\theta_2 = \theta_q)}{d\Omega_1 d\Omega_2 dE_2} \tag{A.7}$$

For the present measurement the data points are extrapolated by fitting the polynomial function

$$\frac{df(q)}{dE}^{exp} = \sum_{i=1}^{7} A_i q^i, \tag{A.8}$$

for the binary and recoil peak intensity, separately. The constrain on the fit is, that the zeroth-order coefficient A_0 has to be the same for both curves. This just reflects the fact, that in the photoionization limit both the binary and the recoil peak have the same intensity, since the angular distribution in photoionization is dipolar. The obtained value for the fit-parameter at q=0 has to be scaled to the known value of df/dE calculated from the photoionization cross section using eq. (A.4). In turn, the scaling factor allows to normalize all FDCS for all other scattering geometries, since all scattering angles and electron energies are internormalized. For the 1 keV data the already normalized GOS as a function of momentum transfer is shown in Fig. A.3 for an energy of 5 eV of the ejected electron.

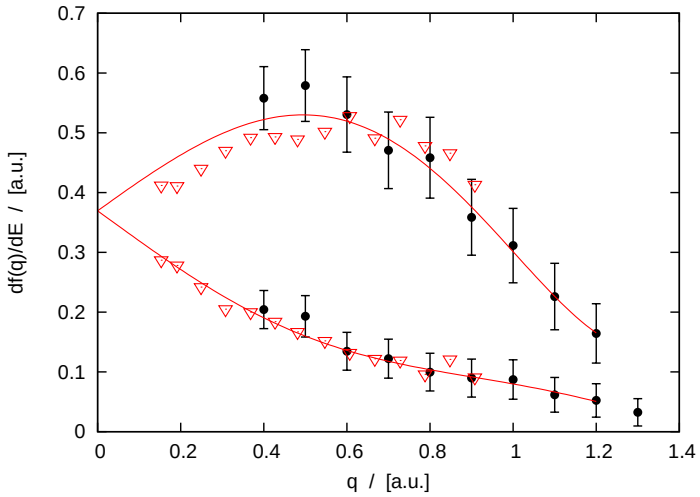

Figure A.3: The GOS at $E_0 = 1\,\text{keV}$ determined in the measurement with the reaction microscope after normalization for $E_2 = 5\,\text{eV}$ (Points). For comparison, the measurement reported in [DCLB$^+$87] at $E_0 = 4106\,\text{eV}$ and $E_2 = 4.3\,\text{eV}$ is included (empty triangles). The fit (solid line) is used to extrapolate the measured GOS to q=0.

The constraint of equal binary to recoil ration on the fit increases the accuracy of the extrapolation method and leads to reliable results, as can be shown by cross-checking the method with other normalization procedures [LBCD87]. The error made through the extrapolation is estimated to around 15% and critically depends on the smallest measurable momentum transfer. In order to be able to judge the quality of the extrapolation of the measured data, it is compared with the experimentally obtained GOS from a measurement with a conventional (e,2e) spectrometer where lower values of the momentum transfer could be reached (see Fig. A.3).

A.2 (e,3e) at $E_0 = 105\,\text{eV}$

A.2.1 Normalization

In the measurement of double ionization with the reaction microscope, triple coincidences resulting from single ionization were recorded simultaneously. In the offline analysis this allows to extract the absolute fully differential cross section for (e,3e) by normalizing it to well established and tested (e,2e) cross sections.

Once more one should recall the relation between the measured rate R^+ and the fully differential cross section for (e,2e):

$$R^+ = \frac{d^3\sigma}{d\Omega_1 d\Omega_2 dE_2} \cdot \Delta\Omega_1 \Delta\Omega_2 \Delta E_2 \cdot \epsilon_{(1,2,+)} \cdot Nj. \tag{A.9}$$

Here $\epsilon_{(1,2,+)}$ denotes the detection efficiency for three particles, two electrons and a singly charged ion. Here Nj is the product of the electron current density and number of target atoms. The 'geometrical' parameters are determined by the chosen width of the applied cuts and the binning in order to extract the experimental FDCS for (e,2e). Scaling the experimentally determined differential cross section to the cross section calculated by the well tested models (e.g. 3C, CCC - see also section 4.1.3) yields the factor $\epsilon_{(1,2,+)} \cdot Nj$.

Since the (e,2e) cross section was measured simultaneously with the (e,3e) and over the same accumulation time, the absolute scale of the fully differential cross section can be determined, since the beam current, the number of target atoms and the detection efficiency for triple coincidences is now known:

$$\frac{d^5\sigma}{d\Omega_1 d\Omega_2 d\Omega_3 dE_2 dE_3} = \frac{R^{++}}{\Delta\Omega_1\Delta\Omega_2\Delta\Omega_3\Delta E_2\Delta E_3 \cdot \epsilon_{(1,2,+)} \cdot Nj} \tag{A.10}$$

Here R^{++} is the experimentally obtained fully differential cross section for (e,3e). One uncertainty remains, which is the detection efficiency for the singly charged ion, which enters into the value $\epsilon(1,2,+)$. For double ionization the detected ion is doubly charged, and the detection efficiency may depend on the charge state. The reason lies in the details of the ion detection: after traversing the spectrometer, the ion is accelerated by a voltage larger than 1 keV before hitting the MCP used for electron multiplication. Ions of different charge states then impinge with different kinetic energies, which may in turn lead to different detection efficiencies. The detection efficiency is essentially the same for He^+ and He^{++} as long as the discriminator thresholds are set properly, which was verified in the present experiment. Thus it can be concluded, that the detection efficiency extracted from single ionization $\epsilon_{1,2,+}$ is the same for double ionization.

A.2.2 Calibration and Resolution

Another important question, is the proper calibration of the imaging properties. There are two steps of testing a proper calibration of the spectrometer properties.

1. Together with double ionization, the coincidence electronics allows to simultaneously record triple coincidences of single ionization events. For this process all final state particles are recorded, and the parameters of the electron-spectrometer can be calibrated from overdetermined kinematics as it was discussed in the experimental chapter 3.

2. The previous step allows to calibrate the electrons. However, the ion spectrometer arm is then calibrated for the singly charged He^+.

The imaging properties of the doubly charged can differ and therefore, the parameters for the He^{++}-ion are extracted from double-ionization events, where *fourfold* coincidences were recorded. Then the ion-spectrometer can be calibrated for the doubly charged ion.

When all four final-state particles are detected, the momentum of the recoil-ion p_{ion} balances the summed momentum of all three electrons. The total sum of the components adds to the initial momentum of the projectile (see Fig. A.4a. The fourfold coincidences do not only allow to carefully calibrate the ion-spectrometer arm, but they also allow to check the resolution. This information is vital for an accurate determination of the fully differential cross section, since the momentum vector of the reconstructed electron is reconstructed from the recoil ion.

A second way to control the accuracy of the calibration is to check energy conservation using triple coincidences. If the energy of the two detected electrons is denoted by $E_{1,2}$ and the energy of the reconstructed electron by E_{rec}, whose momentum has been calculated from the recoil ion, they have to fulfill energy conservation $E_1 + E_2 = 26\,eV - E_{rec}$ as shown in Fig. A.4b. The sum of the energy of the two first electrons arriving the detector $E_1 + E_2$ and that of the third electron is constant. The width reflects the limited resolution for E_{rec}, which results from the poor momentum of the recoil ion. Another important issue of the spectrum in Fig. A.4b is, that it offers a unique possibility to ensure, that the two electrons and the recoil ion detected originate from the same collision event and that there is essentially no background present. Only for 'true' triple-coincidences the energy of the detected electrons is balanced by the energy of the reconstructed electron. The absence of background marks the great advantage of recoil-ion momentum spectroscopy over the conventional electron spectrometers used for (e,3e) experiments, where only the outgoing electrons are detected. There, random coincidences resulting from single ionization lead to considerable background, which has to be subtracted in the offline analysis (see for example [LB91]). For this reason (e,3e) experiments using the conventional technique are increasingly difficult near threshold, since the ratio of the total cross section for double- and single-ionization drops down to a range of 10^{-4} and at the same time the total cross section for double ionization is very low (see Fig. 4.17). For the data presented here and for all three runs the total measurement period was approximately 6 weeks.

A.2.3 Generation of the Experimental FDCS

For the time being and until stated otherwise, electron (1) is the electron which arrived first on the detector, and electron (2) is the one which arrived later and both will just be named as the 'detected' electrons. For the present the third undetected electron is labeled with 'rec'. In the evaluation of the

Momentum balance:

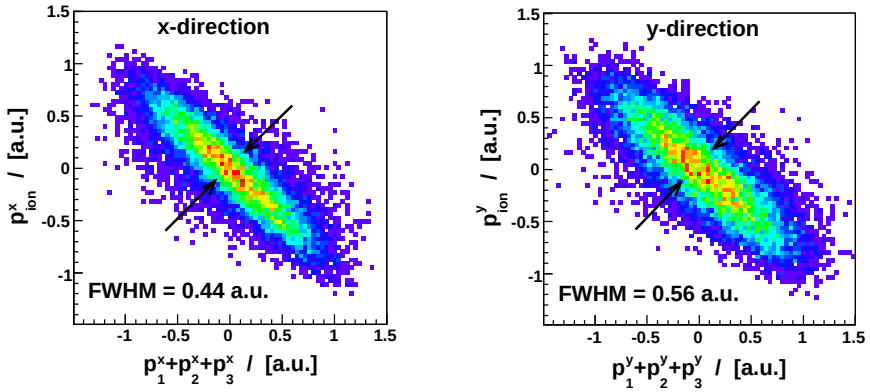

(a) Momentum balance of all final-state particles in double ionization in the transverse x- and y-direction.

Energy balance:

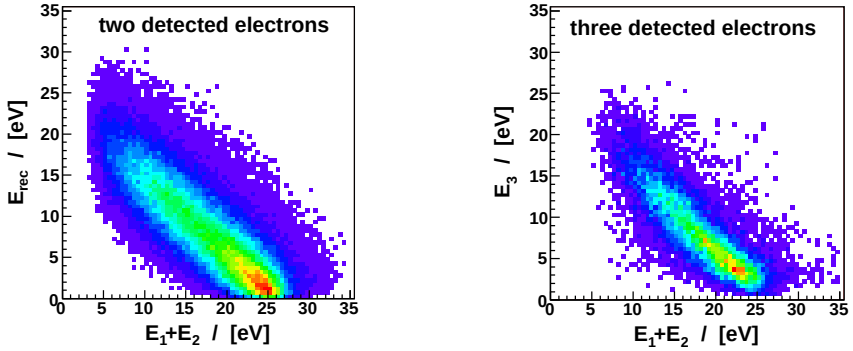

(b) Energy balance for the final-state electrons. On the left only two electrons were detected. The momentum on the undetected electron can be inferred from the momentum of the recoil ion, which allows to reconstruct its energy E_{rec}. The same spectrum for fourfold coincidences is shown on the right, where the energy of the third electron can be calculated directly.

Figure A.4: Spectra proving the proper calibration of the electron- and recoil-ion-spectrometer. At the same time, the resolution of the recoil-ion momentum spectroscopy of doubly-charged ions can be checked by means of momentum and energy conservation.

experimental FDCS in sec. 4.3.3, cuts in the polar angle θ of two from the in total three electrons are applied in the offline analysis. The fully differential cross section is then plotted as a function of the polar angle θ of the third electron. In the offline analysis three different possibilities of applying these cuts arise. These are indicated in Fig. A.5 where one electron is held fixed at $\theta = 45°$, a second at $\theta = 135°$ and where then the measured number of counts can be plotted as a function of the angle of the third electron. First, the two fixed electrons can be both detected electrons, which is situation (a) in the Fig. A.5. Secondly (b), one detected electron is fixed at the smaller angle $\theta = 45°$, and the reconstructed is held fixed at the larger angle. The FDCS in this situation is then the number of counts as a function of the angle of the second detected electron. Finally (c), the electrons with 'fixed' angles swap their role and now the reconstructed electron is fixed at the smaller angle. Again the FDCS is obtained from the number of counts of the other detected electron. For the absolute cross section the number of counts for all three situations (a), (b) and (c) shown in Fig. A.5 have to be added, since they all represent the same 'scattering' geometry.

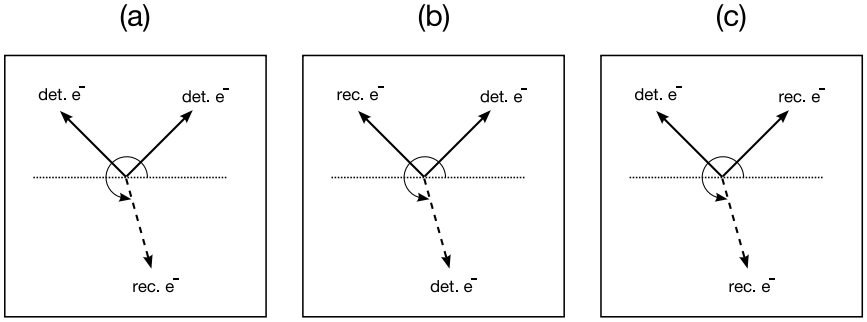

Figure A.5: In the (e,3e) experiment with the reaction microscope, two final state electrons are detected and the momentum of the third is reconstructed from the momentum of the recoil ion. For the extraction of the fully differential cross section at a particular scattering geometry, three different angular combinations (a), (b) and (c) of the detected and reconstructed electron lead to the same scattering geometry.

As discussed earlier, the angular-acceptance interval depends on the energy of the detected electrons. For example if the FDCS is evaluated for a cut in electron energies $E_{1,2} = 6\ eV - 12\ eV$, the resulting acceptance for the polar angle of detected electrons is $30° \leq \theta_{1,2} \leq 160°$ when all three measurement runs are combined. This fact has to be considered for the individual situations, under which the angular emission pattern is shown. If the FDCS is plotted as a function of the reconstructed electron, which would be situation (a) in Fig. A.5, the full angular range is available. In contrast, accpetance-holes will appear, if the FDCS is plotted as a function of the angle of the detected electron. Since the absolute FDCS results from

the sum of all emission patterns generated from (a), (b) and (c), there will be 'missing' events at angles $\theta \leq 30°$, $160° \leq \theta \leq 200°$ and $\theta \geq 330°$. The absolute cross section at these angles can be 'filled up' by scaling the cross section gained from the reconstructed electron by a factor of 3. There is one last remaining point. In order to avoid any further complications, the angles of the two fixed electron are chosen to be inside the accepted angular range of the detected electrons.

With this issue settled and in order to simplify the discussion, the electron with the small fixed angle θ_1 now gets the index (1), the electron fixed at larger θ_2 angle gets the index (2). The fully differential cross sections are then plotted as function of one electron's emission angle θ_3 for fixed emission angle of the remaining two electrons.

A.3 Atomic Units

It is convenient to use atomic units, which is oriented on the scale given by the hydrogen atom and the bound electron. The natural constants are chosen to be $\hbar = m_e = e = 1$ (e: electron charge, m_e : electron mass). In the following table lists some of the factors for the conversion from SI-units to atomic units (a.u.).

$a_0 = 1\ a.u.$=$0.5291772083 \times 10^{-10}\ m$	Bohr Radius
$m_e = 1\ a.u.$=$9.10938188 \times 10^{-31}\ kg$	electron mass
$e = 1\ a.u.$=$1.602176462 \times 10^{-19}\ C$	electron charge
$v_e = 1\ a.u.$=$2.1877 \times 10^{6}\ m/s$	classical velocity of bound electron
$\hbar = 1\ a.u.$=$1.054571596 \times 10^{-34}\ Js$	angular momentum
$\xi_0 = 1\ a.u.$=$5.1422 \times 10^{11} V/m$	electric field of the proton at distance a_0
$E = 1\ a.u.$=$4.36 \times 10^{-18}\ J = 27,22\, eV$	2 × Rydberg energy of bound electron
$t = 1 a.u.$=$2,41888 \times 10^{-17}\ s$	classical orbital time of bound electron

A.4 Electronic Circuit

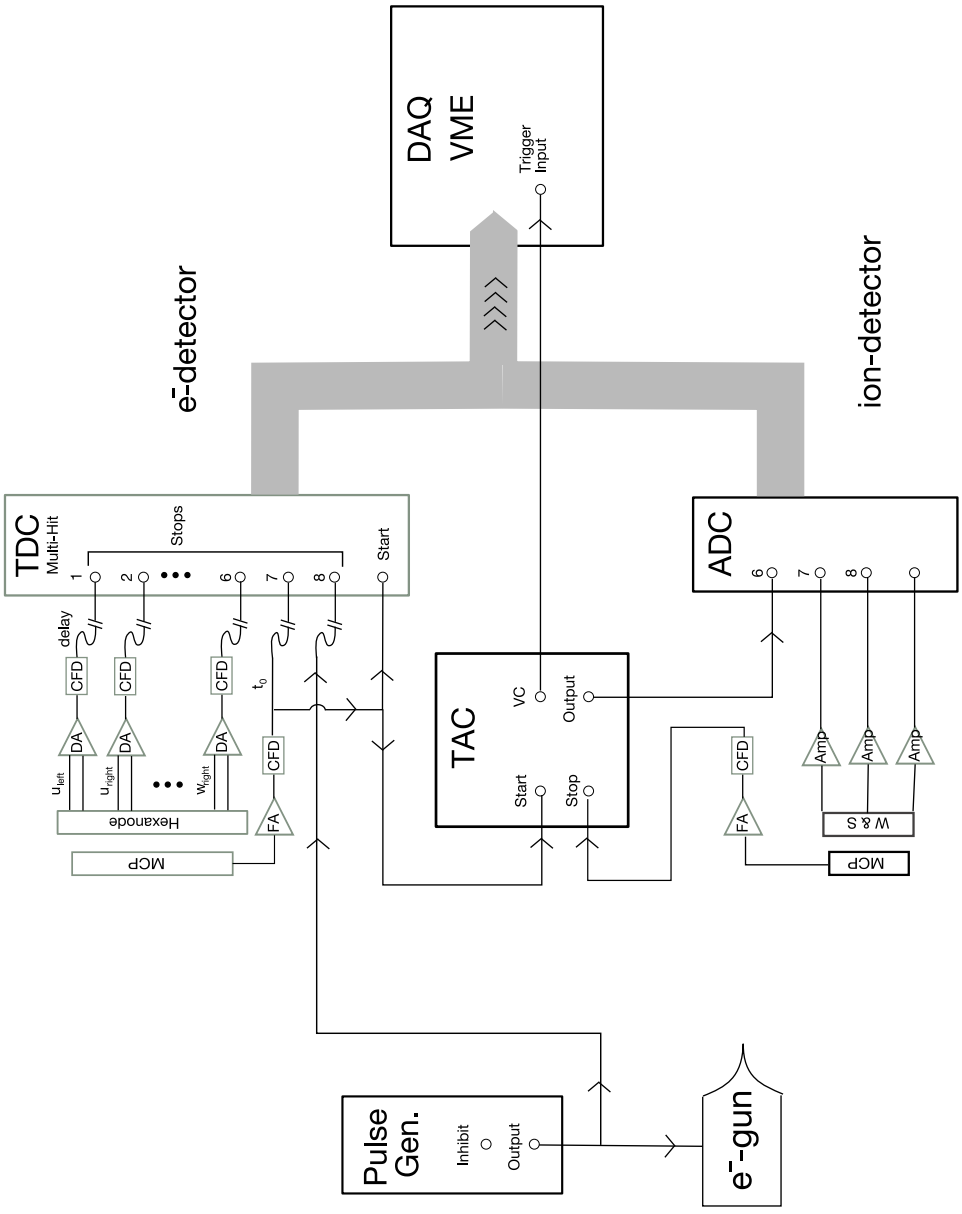

Figure A.6: Electronic circuit used for the measurements with the reaction microscope. FA : Fast Amplifier; CFD : Constant Fraction Discriminator; W & S : Wedge and Strip Anode.

Bibliography

[ACF+87] L. Avaldi, R. Camilloni, E. Fainelli, G. Stefani, A. Franz, H. Klar, and I. E. McCarthy. Absolute tripple differential cross sections for electron impact ionisation of He at 1024.6 eV incident energy. *J. Phys. B*, 20:5827, 1987.

[ACM+98] L. Avaldi, R. Camilloni, R. Multari, G. Stefani, J. Langlois, O. Robeaux, R. J. Tweed, and G. Nguyen Vien. Absolute measurement of ionization-excitation of helium at intermediate energies and their interpretation. *J. Phys. B*, 31:2981, 1998.

[AHK+86] L. H. Andersen, P. Hvelplund, H. Knudsen, S. P. Møller, K. Elsner, K.-G. Rensfelt, and E. Uggerhøj. Single and Double Ionization by Fast Antiproton and Proton Impact. *Phys. Rev. Lett.*, 57(17):2147, 1986.

[AMC04] L. U. Ancarani, T. Montagnese, and C. Dal Capello. Role of the helium ground state in (e,3e) processes. *Phys. Rev. A*, 70, 2004.

[BB94] J. Berakdar and J. S. Briggs. Three-Body Coulomb Continuum Problem. *Phys. Rev. Lett.*, 72(24):3799, 1994.

[BB99] V. V. Balashov and I. V. Bodrenko. Triple coincidence (e,2eγ) measurements as a 'perfect experiment' instrument for ionization-excitation studies. *J. Phys. B*, 32:L687, 1999.

[BBB90] M. Brauner, J. S. Briggs, and J. T. Broad. Triply differential cross sections for ionization of helium by electrons. *J. Phys. B.*, 24:287, 1990.

[BBK89] M. Brauner, J. S. Briggs, and H. Klar. Triply-differential cross sections for ionisation of hydrogen atoms by electrons and positrons. *J. Phys. B*, 22:2265, 1989.

[BBK93] J. Berakdar, J. S. Briggs, and H. Klar. Scaling behaviour of the triply differential cross section for the ionization of atomic hydrogen. *J. Phys. B*, 26:285, 1993.

[BC99] Gy. Bencze and C. Chandler. Impossibility of distinguishing between identical particles in quantum collision processes. *Phys. Rev. A*, 59(4):3129–3132, 1999.

[BCC+97] S. J. Brotton, S. Cvejanovic, F. J. Currell, N. J. Bowring, and F. H. Read. Electron-impact excitation of the doubly excited states of helium below the N=3 He^+ threshold. *Phys. Rev. A*, 55:318, 1997.

[BCH+00] B. Boudaïffa, P. Cloutier, D. Hunting, M. A. Huels, and L. Sanche. Resonant Formation of DNA Strand Breaks by Low-Energy (3 to 20 eV) Electrons. *Science*, 287:1658, 2000.

[Bet30] H. Bethe. Zur Theorie des Durchgangs schneller Korpuskularstrahlen durch Materie. *Ann. d. Physik*, 25:325, 1930.

[BF96a] I. Bray and D. V. Fursa. Calculation of ionization within the close-coupling formalism. *Phys. Rev. A*, 54(4):2991–3004, 1996.

[BF96b] Igor Bray and Dmitry V. Fursa. Convergent close-coupling method: A "Complete scattering theory"? *Phys. Rev. Lett.*, 76(15):2674–2677, 1996.

[BHS+96] K. Bartschat, E. T. Hudson, M. P. Scott, P. G. Burke, and V. M. Burke. Convergent R-Matrix with pseudostates calculation for e^--He collisions. *Phys. Rev. A*, 54:R988, 1996.

[BJ67] F. W. Byron and C. J. Joachain. Multiple Ionization Processes in Helium. *Phys. Rev.*, 164:1, 1967.

[BKHM78] E. C. Beaty, K. H. Kesselbacher, S. P. Hong, and J. H. Moore. Measurements of the triple-differential cross section for low-energy electron-impact ionization of helium. *Phys. Rev. A*, 17(5):1592–1599, 1978.

[BLBC03] J. Berakdar, A. Lahmam-Bennani, and C. Dal Cappelo. The electron-impact double ionization of atoms: an insight into the four-body Coulomb scattering dynamics. *Phys. Rep.*, 374:91, 2003.

[BLW04] J. B. Bluett, D. Lukić, and R. Wehlitz. Triple photoionization of Ne and Ar near threshold. *Phys. Rev. A*, 69:042717, 2004.

[BMC96] V. V. Balashov, S. E. Martin, and A. Crowe. (e,2e) in the vicinity of an autoionizing state as a 'perfect experiment' to measure parameters of the electron-impact ionization process. *J. Phys. B*, 29:L337, 1996.

[Bor26a] M. Born. Quantenmechnik der Stoßvorgänge. *Zeitschr. f. Phys.*, 38:803, 1926.

[Bor26b] M. Born. Zur Quantenmechnik der Stoßvorgänge. *Zeitschr. f. Phys.*, 37:863, 1926.

[Bra99] I. Bray. Reply to: "Possibility of distinguishing between identical particles in quantum collision processes". *Phys. Rev. A*, 59(4):3133, 1999.

[Bra02] I. Bray. Close Coupling Approach to Coulomb Three-Body Problems. *Phys. Rev. Lett.*, 89:273201, 2002.

[BS92] I. Bray and A. T. Stelbovics. Convergent close-coupling calculations of electron-hydrogen scattering. *Phys. Rev. A*, 46:6995, 1992.

[BS00] J. S. Briggs and V. Schmidt. Differential cross sections for photo-double-ionization of the helium atom. *J. Phys. B*, 33:R1, 2000.

[BS02] I. Bray and A. T. Stelbovics. Comment on "Status of the convergent close-coupling method within the framework of the rigorous Coulomb scattering theory". *Phys. Rev. A*, 66(3):036701, 2002.

[BS04] P. L. Bartlett and A. T. Stelbovics. Threshold Behaviour of e-H Ionizing Collisions. *Phys. Rev. Lett.*, 93:233201, 2004.

[BSKW97] M. J. Brunger, O. Samardzic, A. S. Kheifets, and E. Weigold. A study of autoionization phenomena in helium using (e,2e) spectroscopy. *J. Phys. B*, 30:3267, 1997.

[BT68] C. E. Brion and G. E. Thomas. A versatile 'monoenergetic' electron impact spectrometer for the study of inelastic collision processes. *Int. J. Mass Spectrom. Ion Phys.*, 1:25, 1968.

[Che06] Zhangjin Chen. private communication, 2006.

[CM05] Zhangjin Chen and D. H. Madison. Second-order distorted wave calculation for electron impact ionization of helium to He^+(n=1 and 2). *J. Phys. B*, 38:4195, 2005.

[CMD94] M. A. Coplan, J. H. Moore, and J. P. Doering. (e,2e) spectroscopy. *Rev. Mod. Phys*, 66:985, 1994.

[CMSW84] J. P. D. Cook, I. E. McCarthy, A. T. Stelbovics, and E. Weigold. Non-coplanar symmetric (e,2e) momentum profile measurements for helium: an accurate test of helium wavefunctions. *J. Phys. B*, 17:2339, 1984.

[CMWW04] Zhangjin Chen, D. H. Madison, Colm T. Whelan, and H. R. Walters. Second-order distorted wave calculation for electron impact ionization of hydrogen. *J. Phys. B*, 37:981, 2004.

[CPCK06] J. Colgan, M. S. Pindzola, G. Childers, and M. A. Khakoo. Low-energy electron-impact single ionization of helium. *Phys. Rev. A*, 73:042710, 2006.

[CPR04] J. Colgan, M. S. Pindzola, and F. Robicheaux. Lattice Calculations of the Photoionization of Li. *Phys. Rev. Lett.*, 93:053201, 2004.

[CR74] S. Cvejanović and F. H. Read. Studies of the threshold electron impact ionization of helium. *J. Phys. B*, 7:1841, 1974.

[CVB+05] G. Da Costa, F. Vurpillot, A. Bostel, M. Bouet, and B. Deconihout. Design of a delay-line position-sensitive detector with improved performance. *Rev. Sci. Instrum.*, 76:013304, 2005.

[DC00] M. Dogan and A. Crowe. Correlation studies of excited states of the helium ion. *J. Phys. B*, 33:L461, 2000.

[DC02] M. Dogan and A. Crowe. Coincidence studies of the influence of resonances on simultaneous-excitation of helium by electron impact. *J. Phys. B*, 35:2773, 2002.

[DCLB+87] A. Duguet, M. Cherid, A. Lahmam-Bennani, A. Franz, and H. Klar. High-accuracy (e,2e) cross sections for helium: reference data in the first born approximation. *J. Phys. B*, 20:6145, 1987.

[DGF+02] S. Denifl, B. Gstir, L. Feketeova, S. Matejcik, K. Becker, A. Stamatovic, P. Scheier, and T. D. Märk. Multiple ionization of helium and krypton by electron impact close to threshold: appearance energies and Wannier exponents. *J. Phys. B.*, 35:4685, 2002.

[DGH+82] J. B. Donahue, P. A. M. Gram, M. V. Hynes, R. W. Hamm, C. A. Frost, H. C. Bryant, K. B. Butterfield, D. A. Clark, and W. W. Smith. Observation of Two-Electron Photoionization of the H^- Ion Near Threshold. *Phys. Rev. Lett.*, 48:1538, 1982.

[DKP+96] R. Dörner, H. Khemliche, M. H. Prior, C. L. Cocke, J. A. Gary, R. E. Olson, V. Mergel, J. Ullrich, and H. Schmidt-Böcking. Imaging of Saddle Point Electron Emission in Slow p-He Collisions. *Phys. Rev. Lett.*, 77:4520, 1996.

[DKS+01] A. Dorn, A. Kheifets, C. D. Schröter, B. Najjari, C. Höhr, R. Moshammer, and J. Ullrich. Double Ionization of Helium by Electron-Impact: Complete Pictures of the Four-Body Breakup Dynamics. *Phys. Rev. Lett.*, 86:3755–3758, April 2001.

[DKS+03] A. Dorn, A. Kheifets, C. Schröter, C. Höhr, G. Sakhelashvili, R. Moshammer, J. Lower, and J. Ullrich. Appearance and disappearance of the second Born effects in the (e,3e) reaction on He. *Phys. Rev. A*, 68(1):012715, July 2003.

[DLBD+92] C. Dupré, A. Lahmam-Bennani, A. Duguet, F. Mota-Furtado, P. F. O'Mahony, and C. Dal Cappello. (e,2e) triple differential cross sections for the simultaneous ionization and excitation of helium. *J. Phys. B*, 25:259, 1992.

[DLBLM98] A. Duguet, A. Lahmam-Bennani, M. Lecas, and B. El Marji. A multidetection, multicoincidence spectrometer for (e,2e) and (e,3e) electron impact ionization measurements. *Rev. Sci. Instrum.*, 1998.

[DMS+99] A. Dorn, R. Moshammer, C. D. Schröter, T. J. M. Zouros, W. Schmitt, H. Kollmus, R. Mann, and J. Ullrich. Double ionization of helium by fast electron impact. *Phys. Rev. Lett.*, 1999.

[ECLBC05] S. Elazzouzi, C. Dal Cappello, A. Lahmam-Bennani, and F. Catoire. Double ionization of helium by electron impact: angular distributions at low incident energy. *J. Phys. B*, 38:1391, 2005.

[EFJ+82] H. Ehrhardt, M. Fischer, K. Jung, Jr. F. W. Byron, C. J. Joachain, and B. Piraux. Triply Differential Cross Sections for the Ionization of Helium by Fast Electrons. *Phys. Rev. Lett.*, 48, 1982.

[EJKS86] H. Ehrhardt, K. Jung, G. Knoth, and P. Schlemmer. Differential Cross Sections of Direct Single Electron Impact Ionization. *Z. Phys. D*, page 3, 1986.

[ER04] A. Emmanouilidou and J. M. Rost. Triple photoionzation of lithium near threshold. (unpublished), 2004.

[ER06] A. Emmanouilidou and J. M. Rost. Triple photoionization of lithium near threshold. *J. Phys. B*, 39:L99, 2006.

[ESTW69] H. Ehrhardt, M. Schulz, T. Tekaat, and K. Willmann. Ionization of Helium: Angular Correlation of the Scattered and Ejected Electrons. *Phys. Rev. Lett.*, 22:89, 1969.

[FA91] A. Franz and P. L. Altick. Electron impactt ionization of helium: coplanar triply differential cross sections at high and intermediate energies. *J. Phys. B*, 25:1577, 1991.

[FB01] Y. Fang and K. Bartschat. Resonance effects in simultaneous electron-impact ionization-excitation of helium. *Phys. Rev. A*, 64:020701, 2001.

[FC68] U. Fano and J. W. Cooper. Spectral Distribution of Atomic Oscillator Strengths. *Rev. Mod. Phys.*, 40:441, 1968.

[FDMC95] M. J. Ford, J. P. Doering, J. H. Moore, and M. A. Coplan. Multiple detector triple coincidence spectrometer for (e,3e) electron impact double-ionization measurements. *Rev. Sci. Instrum.*, 66(5):3137, 1995.

[FF90] J. M. Feagin and R. D. Filipczyk. Multiple Wannier Power Laws for 3e Escape. *Phys. Rev. Lett.*, 64:384, 1990.

[FKZ+04] M. Fischer, N. Kolachevsky, M. Zimmermann, R. Holzwarth, Th. Udem, T. W. Hansch, M. Abgrall, J. Grunert, I. Maksimovic, S. Bize, H. Marion, F. Pereira Dos Santos, P. Lemonde, G. Santarelli, P. Laurent, A. Clairon, C. Salomon, M. Haas, U. D. Jentschura, and C. H. Keitel. New Limits on the Drift of Fundamental Constants from Laboratory Measurements. *Phys. Rev. Lett.*, 92:230802, 2004.

[FPR91] P. D. Fainstein, V. H. Ponce, and R. D. Rivarola. Two-centre effects in ionization by ion impact. *J. Phys. B*, 24:3091, 1991.

[FPS+05] M. Foster, J. L. Peacher, M. Schulz, A. Hasan, and D. H. Madison. Precollision and postcollision electron-electron correlation effects for intermediate-energy proton-impact ionization of helium. *Phys. Rev. A*, 72:062708, 2005.

[GB] J. R. Götz and J. S. Briggs. Mehrteilchen Effekte im Coulomb-Kontinuum. In *26. Arbeitsbericht Energiereiche Atomare Stöße*.

[Gey04] T. Geyer. Electron impact double ionization of helium from classical trajectory calculations. *J. Phys. B*, 37:1215, 2004.

[Gmb] RoentDek GmbH. Kelkheim, Germany (www.roentdek.com).

[Gru83] P. Grujic. The threshold law for double ionisation in electron-atom collisions. *J. Phys. B*, 16:2567, 1983.

[GWB03] J. R. Götz, M. Walter, and J. S. Briggs. Appearance of non-first-Born effects in (e,3e) on helium. *J. Phys. B*, 36:L77, 2003.

[Haa06] N. Haag. N.n. Master's thesis, University of Heidelberg, 2006.

[HMF+04] A. Hasan, N. V. Maydanyuk, B. Fendler, A. Voitkiv, and B. Najjari. Three-dimensional fully differential single ionization cross sections for 75 keV p+He collisions. *J. Phys. B*, 37:1923, 2004.

[HMR05a] D. A. Horner, C. W. McCurdy, and T. N. Rescigno. Electron-impact excitation autoionization of helium in the s-wave limit. *Phys. Rev. A*, 71(1):010701, 2005.

[HMR05b] D. A. Horner, C. W. McCurdy, and Thomas N. Rescigno. Electron-helium scattering in the s-wave model using exterior complex scaling. *Phys. Rev. A*, 71(1):012701, 2005.

[HSSS05] C. Hugenschmidt, K. Schreckenbach, M. Stadlbauer, and B. Straßer. Low-energy positrons of high intensity at the new positron beam faccility NEPOMUC. *Nucl. Instrum. Meth. A*, 554:384, 2005.

[HSWM91] A. Huetz, P. Selles, D. Waymel, and J. Mazeau. Wannier Theory for Double Photoionization of Noble Gases. *J. Phys. B*, 24:1917, 1991.

[HW96] P. A. Hayes and J. F. Williams. Simultaneous Ionization and Excitation to the He^+ 2^2P State. *Phys. Rev. Lett.*, 77:3098, 1996.

[Ino71] M. Inokuti. Inelastic Collisions of Fast Charged Particles with Atoms and Molecules–The Bethe Theory Revisited. *Rev. Mod. Phys.*, page 297, 1971.

[Jea02] O. Jagutzki and et. al. Multiple Hit Readout of a Microchannel Plate Detector With a Three-Layer Delay-Line Anode. *IEEE Transactions on Nuclear Science*, 49:2477, 2002.

[JM00] S. Jones and D. H. Madison. Ionization of hydrogen atoms by fast electrons. *Phys. Rev. A*, 62:042701, 2000.

[JM03a] S. Jones and D. H. Madison. Role of the Ground State in Electron-Atom Double Ionization. *Phys. Rev. Lett.*, 91:073201, 2003.

[JM03b] S. Jones and D. H. Madison. Scaling behaviour of the fully differential cross section for ionization of hydrogen atoms by the impact of fast elementary charged particles. *Phys. Rev. A*, 65:05272, 2003.

[JMFS$^+$85] K. Jung, R. Müller-Fiedler, P. Schlemmer, H. Ehrhardt, and H. Klar. Absolute triple differential cross sections of electron impact ionisation of helium at 600 eV collision energy. *J. Phys. B*, 18:2955, 1985.

[Joa] Charles J. Joachain. *Quantum Collision Theory.* North-Holland Publishing Company Amsterdam.

[KB98] A. S. Kheifets and I. Bray. Calculation of Circular Dichroism in Helium Double Photoionization. *Phys. Rev. A*, 81:4588, 1998.

[KBB99] A. S. Kheifets, I. Bray, and K. Bartschat. Convergent calculations for simultaneous electron-impact ionization-excitation of helium. *J. Phys. B*, 1999.

[KBLB$^+$99] A. S. Kheifets, I. Bray, A. Lahmam-Bennani, A. Duguet, and I. Taouil. A comparative experimental and theoretical investigation of the electron-impact double ionization of He in the keV regime. *J. Phys. B*, 1999.

[KBNCP90] H. Knudsen, L. Brun-Nielsen, M. Charlton, and M. R. Poulsen. Single ionization of H_2, He, Ne and Ar by positron impact. *J. Phys. B.*, 23:3955, 1990.

[Khe04] A. S. Kheifets. Second-order Born model for two-electron atomic ionization by fast charged particle impact. *Phys. Rev. A*, 69:032712, 2004.

[KMSB03] A. S. Kadyrov, A. M. Mukhamedzhanov, A. T. Stelbovics, and I. Bray. Integral Representation for the Electron-Atom Ioization Amplitude which is Free of Ambiguity and Divergence Problems. *Phys. Rev. Lett.*, 91(25):253202, 2003.

[KMSB04] A. S. Kadyrov, A. M. Mukhamedzhanov, A. T. Stelbovics, and I. Bray. Theory of electron-impact ionization of atoms. *Phys. Rev. A*, 70(6):062703, 2004.

[KO98] M Yu. Kuchiev and V. N. Ostrovsky. Threshold laws for the breakup of atomic particles into several charged fragments. *Phys. Rev. A*, 58:321, 1998.

[KS76] H. Klar and W. Schlecht. Treshold multiple ionization of atoms. Energy dependence for double and triple escape. *J. Phys. B*, 9(10):1699, 1976.

[LB91] A. Lahmam-Bennani. Recent developments and new trends in (e,2e) and (e,3e) studies. *J. Phys. B*, 24:2401, 1991.

[LB02] A. Lahmam-Bennani. Thirty years of experimental electron-electron (e,2e) coincidence studies: achievements and perspectives. *Journ. Electr. Spectr.*, 123:365, 2002.

[LBAFS88] A. Lahmam-Bennani, L. Avaldi, E. Fainelli, and G. Stefani. The asymmetric (e,2e) collisions at intermediate and high impact energy: success and limits of first order models. *J. Phys. B*, 21:2145, 1988.

[LBCD87] A. Lahmam-Bennani, M. Cherid, and A. Duguet. A critical evaluation of various methods for absolute scale determination in (e,2e) experiments. *J. Phys. B*, 20:2531, 1987.

[LBDC$^+$03] A. Lahmam-Bennani, A. Duguet, C. Dal Cappello, H. Nebdi, and B. Piraux. Importance of non-first-order effects in the (e,3e) double ionization of helium. *Phys. Rev. A*, 67:010701, 2003.

[LBDD89] A. Lahmam-Bennani, C. Dupré, and A. Duguet. Electron-Impact Ionization of Argon Studied by Double and Triple Coincidence Techniques: The First (e,3e) Experiment. *Phys. Rev. Lett.*, 63:1582, 1989.

[LBDG$^+$01] A. Lahmam-Bennani, A. Duguet, M. N. Gaboriaud, I. Taouil, M. Lecas, A. Kheifets, J. Berakdar, and C. Dal Cappello. Complete experiments for the double ionization of He: (e,3e) cross sections at 1 keV impact energy and small momentum transfer. *J. Phys. B*, 34:3072, 2001.

[LBTD$^+$99] A. Lahmam-Bennani, I. Taouil, A. Duguet, M. Lecas, L. Avaldi, and J. Berakdar. Origin of dips and peaks in the absolute fully resolved cross sections for the electron-impact double ionization of He. *Phys. Rev. A*, 59:3584, 1999.

[LRW99] S. Lucey, J. Rasch, and Colm T. Whelan. On the use of analytic ansatz three-body wave functions in the study of (e,2e) and related processes. *Proc. R. Lond. A*, 455:349, 1999.

[LTL00] T. G. Lee, H. C. Tseng, and C. D. Lin. Evaluation of antiproton-impact ionization of He atoms below 40 keV. *Phys. Rev. A*, 61:06271, 2000.

[LW90] J. Lower and E. Weigold. Correlations in the autoionising region of He measured by the (e,2e) technique. *J. Phys. B*, 23:2819, 1990.

[MB97] A. W. Malcharek and J. S. Briggs. The n-electron Coulomb continuum. *J. Phys. B*, 30:4419, 1997.

[MBR04] C. W. McCurdy, M. Baertschy, and T. N. Rescigno. Solving the three-body Coulomb breakup problem using exterior complex scaling. *J. Phys. B*, 37:R137, 2004.

[McG82] J. H. McGuire. Double Ionization of Helium by Protons and Electrons at High Velocities. *Phys. Rev. Lett.*, 49:1153, 1982.

[MFF+03] D. H. Madison, D. Fischer, M. Foster, R. Moshammer, S. Jones, and J. Ullrich. Probing Scattering Wave Functions Close to the Nucleus. *Phys. Rev. Lett.*, 91(25):253201, 2003.

[MFK03] R. Moshammer, D. Fischer, and H. Kollmus. *Many-Particle Quantum Dynamics in Atomic and Molecular Fragmentation*, chapter Recoil-Ion Momentum Spectroscopy and "Reaction Microscopes". Springer-Verlag Berlin Heidelberg New York, 2003.

[MFS+99] R. Moshammer, P. D. Fainstein, M. Schulz, W. Schmitt, H. Kollmus, R. Mann, S. Hagmann, and J. Ullrich. Initial State Dependence of Low-Energy Electron Emission in Fast Ion Atom Collisions. *Phys. Rev. Lett.*, 83:4721, 1999.

[Mil88] D. R. Miller. *Atomic and Molecular Beam Methods*, volume 1, chapter Free Jet Sources, pages 14–53. Oxford University Press, 1988.

[MJL+81] C. Martin, P. Jelinski, M. Lampton, R. F. Malina, and H. O. Anger. Wedge-and-strip anodes for centroid-finding position-sensitive photon and particle detectors. *Rev. Sci. Instrum.*, 52:1067, 1981.

[MO04] J. H. Macek and S. Yu Ovchninikov. Energy and angular distributions of electrons ejected from atomic hydrogen by low-energy proton impact. *Phys. Rev. A*, 70:052702, 2004.

[MR92] A. J. Murray and F. H. Read. Novel Exploration of the Helium Ionization Process. *Phys. Rev. Lett.*, 69:2912, 1992.

[MRR+00] P. J. Marchalant, B. Rouvellou, J. Rasch, S. Rioual, Colm T. Whelan, A. Pochat, D. H. Madison, and H. R. J. Walters. Excitation-ionization of helium to He^+(n=2) at 365.8 ev. *J. Phys. B*, 33:L749, 2000.

[MSJ+01] D. Madison, M. Schulz, S. Jones, M. Foster, R. Moshamer, and J. Ullrich. Comparison of theoretical and absolute experimental fully-differential cross sections for ion-atom impact ionization. *J. Phys. B*, 35:3297, 2001.

[MUS+96] R. Moshammer, M. Unverzagt, W. Schmitt, J. Ullrich, and H. Schmidt-Böcking. A 4π recoil-ion electron momentum analyzer: a high resolution 'microscope' for the investigation of the dynamics of atomic, molecular and nuclear reactions. *Nucl. Instrum. Methods B*, 1996.

[MUU+94] R. Moshammer, J. Ullrich, M. Unverzagt, W. Schmidt, P. Jardin, R. E. Olson, R. Mann, R. Dörner, V. Mergel, U. Buck, and H. Schmidt-Böcking. Low-Energy Electrons and Their Dynamical Correlation with Recoil Ions for Single Ionization of Helium by Fast, Heavy-Ion Impact. *Phys. Rev. Lett.*, 73:3371, 1994.

[MWR92] A. J. Murray, M. B. Woolf, and F. H. Read. Results from symmetric and non-symmetric energy sharing (e,2e) experiments in the perpendicular plane. *J. Phys. B*, 25:3021, 1992.

[OF05] R. E. Olson and J. Fiol. Extreme Sensitivity of Differential Momentum Transfer Cross Sections to Target Atom Initial Conditions. *Phys. Rev. Lett.*, 95(26):263203, 2005.

[Pet77] R. K. Peterkop. *Theory of Ionization of Atoms by Electron-Impact*. Colorado Associated University Press, Boulder, 1977.

[PNB+04] C. Plottke, P. Nicol, I. Bray, D. V. Fursa, and A. T. Stelbovics. Electron-impact helium double excitation within the S-wave model. *J. Phys. B*, 37:3711, 2004.

[PS91] C. Pan and A. F. Starace. Target Dependence of Angular Distributions for Near-Threshold (e,2e) Processes. *Phys. Rev. Lett.*, 67:185, 1991.

[Rau71] A. R. P. Rau. Two Electrons in a Coulomb Potential. Double-Continuum Wave Functions and Threshold Law for Electron-Atom Ionization. *Phys. Rev. A*, 4:207, 1971.

[RBFM96] J. Röder, I. Bray, D. V. Fursa, and I. E. McCarthy. Absolute triple differential cross section for electron-impact ionization of helium at 40 ev. *J. Phys. B*, 29:2103, 1996.

[RBIM99] T. N. Rescigno, M. Baertschy, W. A. Isaacs, and C. W. McCurdy. Collisional Breakup in a Quantum System of Three Charged Particles. *Science*, 286:2474, 1999.

[REP+97] J. Röder, H. Ehrhardt, Cheng Pang, A. F. Starace, I. Bray, and D. V. Fursa. Absolute Triply Differential (e,2e) Cross Section Measurements fo H with Comparison to Theory. *Phys. Rev. Lett.*, 79:1666–1669, 1997.

[RPRB06] C. Ruiz, L. Plaja, L. Roso, and A. Becker. Ab initio Calculation of the Double Ionization of Helium in a Few-Cycle Laser Pulse Beyond the One-Dimensional Approximation. *Phys. Rev. Lett.*, 96:053001, 2006.

[RRF+92a] T. Rösel, J. Röder, L. Frost, K. Jung, and H. ehrhardt. Measurement of absolute, near-threshold triple differential cross sections for electron impact ionization. *J. Phys. B*, 25:3859, 1992.

[RRF+92b] T. Rösel, J. Röder, L. Frost, K. Jung, H. Ehrhardt, S. Jones, and D. H. Madison. Absolute triple differential cross section for ionization of helium near threshold. *Phys. Rev. A*, 46(5):2539–2552, 1992.

[RRP+00] B. Rouvellou, S. Rioual, A. Pochat, R. J. Tweed, J. Langlois, G. Nguyen Vien, and O. Robaux. Simultaneous excitation-ionization of helium at five times threshold. *J. Phys. B*, 33:L599, 2000.

[RS65] M. R. H. Rudge and M. J. Seaton. Ionization of Atomic Hydrogen by Electron Impact. *Proc. R. Phys. Soc.*, 283:262, 1965.

[Rud68] M. R. H. Rudge. Theory of the Ionization of Atoms by Electron Impact. *Rev. Mod. Phys.*, 40:564, 1968.

[Rut11] E. Rutherford. The scattering of α and β Particles by Matter and the Structure of the Atom. *Phil. Mag. 21*, page 669, 1911.

[SA88] J. A. R. Samson and G. C. Angel. Test of the Threshold Law for TriplePhotoionization in Atomic Oxygen and Neon. *Phys. Rev. Lett.*, 61:1584, 1988.

[SAC90] G. Stefani, L. Avaldi, and R. Camilloni. On the relevance of the final ionic state to the (e,2e) TDCS. *J. Phys. B*, 23:L227, 1990.

[SBFB05] A. T. Stelbovics, I. Bray, D. V. Fursa, and K. Bartschat. Electron-impact ionization of helium for equal-energy-sharing kinematics. *Phys. Rev. A*, 17(5):1592, 2005.

[SBP02] V. L. Shablov, V. A. Bilyk, and Yu. V. Popov. Status of the convergent close-coupling method within the framework of the rigorous Coulomb scattering theory. *Phys. Rev. A*, 65:042719, 2002.

[SCB+97] O. Samardzic, L. Campbell, M. J. Brunger, A. S. Kheifets, and E. Weigold. Autoionization in electron-helium collisions: an (e,2e) investigation. *J. Phys. B*, 30:4383, 1997.

[SDH+05] G. Sakhelashvili, A. Dorn, C. Höhr, J. Ullrich, A. S. Kheifets, J. Lower, and Bartschat. Triple Coincidence (e,γ2e) Experiment for Simultaneous Electron Impact Ionization Excitation of Helium. *Phys. Rev. Lett.*, 95(3):033201, July 2005.

[SEMG88] M. B. Shah, D. S. Elliot, P. McCallion, and H. B. Gilbody. Single and double ionization of helium by electron impact. *J. Phys. B*, 21:2751, 1988.

[SL64] S. M. Silvermann and E. N. Lassettre. Additional Collision Cross Sections for Helium Especially in the Ionized Continuum. *J. Chem. Phys.*, 40:1265, 1964.

[SMF+03] M. Schulz, R. Moshammer, D. Fischer, H. Kollmus, D. H. Madison, S. Jones, and J. Ullrich. Three-dimensional imaging of atomic four-body processes. *Nature (London)*, 422:48, 2003.

[SMS+00] M. Schulz, R. Moshammer, W. Schmitt, H. Kollmus, R. Mann, S. Hagmann, R. E. Olson, and J. Ullrich. Correlated three-electron continuum states in triple ionization by fast heavy-ion impact. *Phys. Rev. A*, 61:022703, 2000.

[SRD+05] C. D. Schröter, A. Rudenko, A. Dorn, R. Moshammer, and J. Ullrich. Status of the pulsed photoelectron source for atomic and molecular collision experiments. *Nucl. Instrum. Meth. A*, 536:312, January 2005.

[SS02] J. A. R. Samson and W. C. Stolte. Precision measurements of the total photoionization cross-sections of He, Ne, Ar, Kr, and Xe. *Journal of Electron Spectroscopy and Related Phenomena*, 123:265, 2002.

[TLBDA98] I. Taouil, A. Lahmam-Bennani, A. Duguet, and L. Avaldi. Fully Determined (e,3e) Experiments for the Double Ionization of Helium. *Phys. Rev. Lett.*, 81:4600, 1998.

[TRR00] G. Tanner, K. Richter, and J.-M. Rost. The theory of two-electron atoms: between ground state and complete fragmentation. *Rev. Mod. Phys.*, 72:497, 2000.

[uGH14] J. Franck und G. Hertz. Über Zusammenstöße zwischen Elektronen und den Molekülen des Quecksilberdampfes und die Ionisierungsspannung derselben. *Verh. Deutsche Phys. Ges.*, 16:457, 1914.

[UMD+03] J. Ullrich, R. Moshammer, A. Dorn, L. Ph. Schmidt, and H. Schmidt-Böcking. Recoil-ion and electron momentum spectroscopy: reaction-microscopes. *Rep. Prog. Phys.*, 66:1463, 2003.

[US03] J. Ullrich and V. P. Shevelko. *Many-Particle Quantum Dynamics in Atomic and Molecular Fragmentation*. Springer, 2003.

[VB05] O. K. Vorov and K. Bartschat. Model sensitivity of theoretical results for ionization-excitation of helium. *J. Phys. B*, 38:1189, 2005.

[vBWC+06] R. V. van Boyen, N. Watanabe, J. W. Cooper, J. P. Doering, J. H. Moore, and M. A. Coplan. Two-step single-ionization mechanisms. *Phys. Rev. A*, 73:032703, 2006.

[VNU03] A. B. Voitkiv, B. Najjari, and J. Ullrich. On the higher-order effects in target single ionization by bare ions in the pertubative regime. *J. Phys. B*, 36:2591–2609, 2003.

[VU03] A. B. Voitkiv and J. Ullrich. Three-body Coulomb dynamics in hydrogen ionization by protons and antiprotons at intermediate collision velocities. *Phys. Rev. A*, 67:062703, 2003.

[vWKvTdH81] B. van Wingerden, J. T. Kimman, M. van Tilburg, and F. J. de Heer. Triple and double differential cross sections for electron impact ionisation of helium and molecular hydrogen. *J. Phys. B*, 14:2475, 1981.

[Wan53] G. H. Wannier. The Treshold Law for Single Ionization of Atoms or Ions by Electrons. *Phys. Rev.*, 90(5):817, 1953.

[Wan55] G. H. Wannier. Treshold Law for Multiple Ionization. *Phys. Rev.*, 100(4):1180, 1955.

[WBS06] J. F. Williams, P. L. Bartlett, and A. T. Stelbovics. Threshold Electron-Impact Ionization Mechanism for Hydrogen Atoms. *Phys. Rev. Lett.*, 96:123201, 2006.

[WKT$^+$05] N. Watanabe, Y. Khajuria, M. Takahashi, Y. Udagawa, P. S. Vinitsky, Yu. V. Popov, O. Chuluunbaatar, and K. A. Kouzakov. (e,2e) and (e,3e-1) studies on double processes of He at large momentum transfer. *Phys. Rev. A*, 71:032705, 2005.

[WPH$^+$00] R. Wehlitz, T. Pattard, M.-T. Huang, I. A. Sellin, J. Burgdörfer, and Y. Azuma. Near-threshold triple-photoionization cross section of lithium. *Phys. Rev. A*, 61:030704, 2000.

Acknowledgements

I am indebted to several people who have contributed to the present work:

- A. Czasch from the Group of R. Dörner and H. Schmidt-Böcking in Frankfurt am Main for supplying the source code of the resort routine for the reconstruction of the Hexanode delay-line signals.
- Calculations were kindly provided by I. Bray, Zhangjin Chen, D. Madison, A. Kheifets, K. Bartschat, J. R. Götz, J. S. Briggs and A. Voitkiv. I am in particular indebted to Bennaceur Najjari, who provided the code to generate 3C cross sections for single ionization of helium. The calculations were extremely handy and were a cornerstone in the course of the work.
- The 'old guard' of former PhD students, Conny Höhr and Daniel Fischer for providing initial aid.
- Shiping Cao for assisting in the fight with the Hexanode and the signal reconstruction. Christina Dimopoulou for taking part in the measurements.
- The ion collision fraction: Michael Schulz for helpful support on generating sensible 3D-plots and Robert Moshammer for helpful hints on technical issues and data analysis.
- Joachim Ullrich for the promotion of the matter and the very stimulating atmosphere.
- Alexander Dorn for the invaluable support in the lab and profound suggestions and hints. The time during the PhD was a very pleasant experience, so thanks a lot!
- I would like to thank my parents for laying the foundations of this thesis. In the end, of course, I would like to particularly thank Julia Schneider for the large amount of invested time, which allowed me to pursue this work. I am also indebted to my daughter Margarete for cherishing her nightly rest so much, that I could go to work well rested.